Washington University in St. Louis
Washington University Open Scholarship

Engineering and Applied Science Theses & Dissertations | McKelvey School of Engineering

Winter 12-15-2017

The Inter-Laminar Shearing Effect on Wrinkle Development in Composite Forming Processes

David Sundquist
Washington University in St. Louis

Follow this and additional works at: https://openscholarship.wustl.edu/eng_etds

Part of the Materials Science and Engineering Commons, Mechanical Engineering Commons, and the Mechanics of Materials Commons

Recommended Citation
Sundquist, David, "The Inter-Laminar Shearing Effect on Wrinkle Development in Composite Forming Processes" (2017). *Engineering and Applied Science Theses & Dissertations*. 297.
https://openscholarship.wustl.edu/eng_etds/297

This Dissertation is brought to you for free and open access by the McKelvey School of Engineering at Washington University Open Scholarship. It has been accepted for inclusion in Engineering and Applied Science Theses & Dissertations by an authorized administrator of Washington University Open Scholarship. For more information, please contact digital@wumail.wustl.edu.

WASHINGTON UNIVERSITY IN ST. LOUIS

Department of Mechanical Engineering and Materials Science

Dissertation Examination Committee:
Doctor David Peters, Chair
Doctor Richard Axelbaum
Doctor Kathy Flores
Doctor Kenneth Jerina
Doctor Shankar Sastry
Doctor Zeaid Hasan

The Inter-Laminar Shearing Effect on Wrinkle Development in Composite Forming Processes

A Dissertation

by

David John Sundquist

A dissertation presented to
the School of Engineering and Applied Science
of Washington University
in partial fulfillment of the
requirements for the degree
of Doctor of Science

December 2017
St. Louis, Missouri

© 2017, David John Sundquist

TABLE OF CONTENTS

LIST OF FIGURES

LIST OF TABLES

ACKNOWLEDGEMENTS

I would like to thank Boeing and Washington University in St. Louis for their support of this research. I would also like to thank my advisor and friends who were valued resources through this project. Your input and guidance were appreciated.

ABSTRACT OF THE DISSERTATION

The Inter-laminar Shearing Effect on Wrinkle Development in Composite Forming Processes

by

David John Sundquist

Doctor of Science in Mechanical Engineering and Materials Science

Washington University in St. Louis, 2017

Professor David Peters, Chair

Composite materials are becoming prevalent in aerospace industries as the uniqueness of the composite structure allows the composite to be tailored specifically for individual applications. Many fabrication techniques produce defects in composite parts such as wrinkles, fiber waviness, fiber misalignment, and porosity. The driving mechanisms behind these defects occurring during forming processes are not fully understood and, thus, characterization formation of these defects in a uncured state is beneficial to optimize composite processing.

This work primarily investigated the influence of how uncured pre-impregnated carbon ply properties affect the wrinkling behavior of a composite laminates. Several factors affecting composite ply forming were investigated include intra-laminar shearing, material tack, and inter-laminar shearing. A series of hot drape forming trials were conducted with uni-directional tapes (UD), plain weaves (PW), and eight harness satin (8HS) prepregs which showed that intra-laminar shearing was a factor in the wrinkling. The 8HS laminate formed without wrinkles while the PW laminate had smaller wrinkles than the tape laminate which followed the trend of drapability of individual plies.

Focusing only on PW prepregs, variations of Cycom 970's PW prepreg was analyzed for tack and inter-laminar shearing. The tack test showed the transition between inter-facial and a cohesive failure which corresponds to the temperature at which the resin starts to flow. The inter-laminar shearing characterization provided strong correlations between viscosity, strain rate, initial pressure, and fiber twist on the shear modulus and shear stress. The characterization of the prepreg properties was also used to develop an uncured laminate model derived from the first-order shear displacement theory. Verification of this model was conducted via experimental hot drape forming of laminates at various Hersey numbers which accurately predicted the experimental wrinkle formation.

CHAPTER 1 – INTRODUCTION

In recent years, composite materials have been used more prevalently by industries including automotive, aerospace, and sporting goods. Fundamentally, a composite is a combination of a matrix and reinforcement. Fiber-reinforced composites utilize the strength of individual fibers such as glass or carbon which are bonded together commonly by epoxy resins. The uniqueness of the composite structure allows the composite to be tailored specifically for individual applications. These engineered composites have shown superior improvements to metal counterparts. Due to the immaturity of the field, many fabrication techniques produce part defects such as wrinkles, fiber waviness, fiber misalignment, and porosity. The mechanisms behind these defects are not fully understood and, thus, an investigation into the formation of these defects in a green state is beneficial to better understand how to optimize composite processing.

This chapter presents an introduction to composite processing with emphases on hot drape forming (HDF). Then a background of laminated plate theory is presented followed by a summary of fluid dynamics principles applied to inter-laminar shearing.

1.1 Composite Forming

Various forming methods have been developed and used for composite materials. Labor-intensive forming methods include hand layup and resin transfer molding while automated-forming techniques include drape forming, press forming, automated fiber placement, filament winding, and tape laying. Each of these techniques utilizes different material choices such as dry fiber tapes, weaves, or pre-impregnated tapes or weaves.

Drape forming is a semi-automated forming process. Drape formers consist of a vacuum table, a stretchable silicone diaphragm, and an optional heat source. Rudimentary drape formers

are depicted in Figure 1 consisting of a vacuum box. Figure 2 depicts an industrial style drape former with infrared (IR) heaters.

(a) HDF assembly **(b)** HDF

Figure 1: Rudimentary Drape Former [1]

Figure 2: Industrial Drape Former [2]

During the draping process, a flat laminate is fabricated reflecting the final layup orientation. The flat laminate is then aligned to the form tool, as depicted in Figure 1. The silicone diaphragm is supported by standoffs, which prevent the diaphragm from prematurely stressing the composite charge. The composite laminate is heated to the required form temperature and vacuum is applied. The force of the diaphragm elongating induces shear stresses into the ply laminate and, thus, initiates inter-laminar shearing and laminate bending as the diaphragm elongates. The vacuum pressure allows for a uniform force to be applied to the

entire part including recessed areas or flanges. The drape forming process is often applied to form angle brackets and channel geometries such as depicted in Figure 1b.

One of the influential defects that occurs from hot drape forming is out-of-plane wrinkle. Formed wrinkles are classified into three groups — span, off-angle, and chord wrinkles — which are similar to those used in [1,3] represented by locations 1, 2, and 3 respectively. Span wrinkles occur along the length axis of the c-channel whereas chord wrinkles are perpendicular to the length. Off-angle wrinkles are a combination of chord and span wrinkles. These wrinkles are at some angle greater than 0° but less than 90° referenced from the c-channel's long axis. The three wrinkle types can occur on the web or flanges and are further depicted in Figure 3. In the flange, the span and off-angle wrinkles occur due to the (0°) oriented plies possessing global tension and bridging the joggle region. The chord wrinkles are caused by local compressive stresses in the laminates near the onset of the joggle region shown by [1].

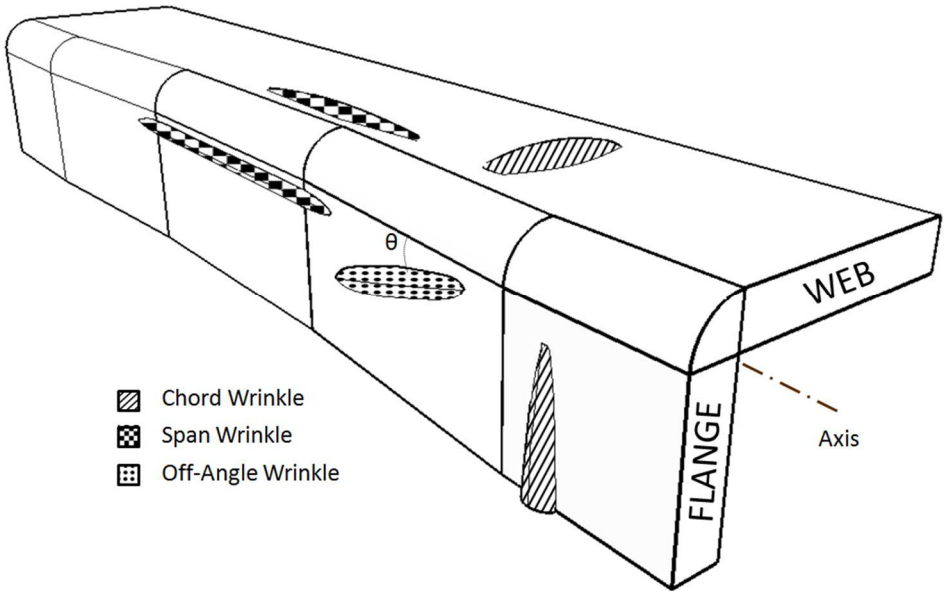

Figure 3: Wrinkle Types Along HDF C-channel Section

1.2 Laminated Plate Theories

Several theories exist for laminated plates. The classical laminated plate theory and the first-order laminated plate theory are presented herein. A laminated plate consists of several different layers of material as depicted in Figure 4. It is customary notation that the midplane of the laminate is the xy plane and the z direction is positive downward. Thus, the k^{th} ply interfaces can be determined to be z_k and z_{k-1} where the difference between the two is the ply thickness.

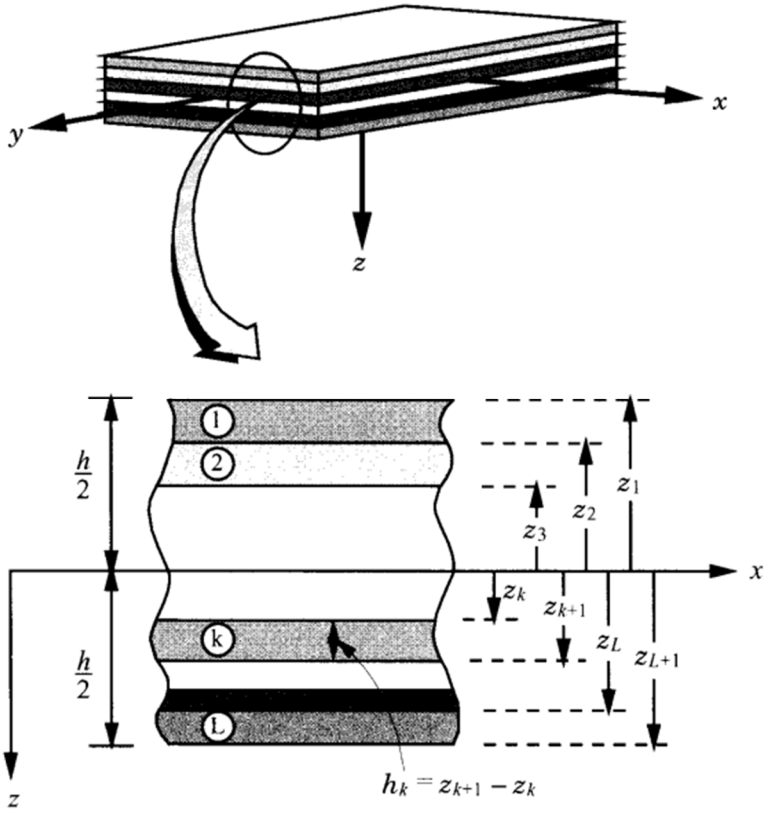

Figure 4: Laminated Plates [4]

From micromechanics, the equations for the engineering constants can be determined. In the following equations, subscripts of *f* designate the fiber while *m* designates the matrix. It will be assumed that the primary direction is along the fiber while secondary direction is aligned to

the matrix for unidirectional materials. Then, the following equations designate the material properties for principle material directions.

$$E_1 = E_f \nu_f + E_m \nu_m \tag{1}$$

$$E_2 = \frac{E_f \nu_f}{E_f \nu_m + E_m \nu_f} \tag{2}$$

$$\nu_{12} = V_f \nu_f + V_m \nu_m \tag{3}$$

$$G_{12} = \frac{G_f G_m}{G_f V_m + G_m V_f} \tag{4}$$

Where V_f and V_m are the volume fractions of the fiber and matrix, respectively. Through a series of transformations and assumptions, Hooke's law, shown in Equation 5, can be determined for a laminate with plies at various orientations measured off the principle direction.

$$\sigma_i = C_{ij} \varepsilon_j \tag{5}$$

While not defined herein, the stiffness matrix $[\bar{Q}]$ is defined in any mechanics of laminated plate text such as [4].

$$\begin{bmatrix} \sigma_x \\ \sigma_y \\ \tau_{xy} \end{bmatrix} = \begin{bmatrix} \bar{Q}_{11} & \bar{Q}_{12} & \bar{Q}_{16} \\ \bar{Q}_{12} & \bar{Q}_{22} & \bar{Q}_{26} \\ \bar{Q}_{16} & \bar{Q}_{26} & \bar{Q}_{66} \end{bmatrix} \begin{bmatrix} \varepsilon_x \\ \varepsilon_y \\ \gamma_{xy} \end{bmatrix} \tag{6}$$

The variation between theories then depends upon the assumptions used to calculate the equations of motion for the system.

1.2.1 Classical Laminated Plate Theory

Classical lamination theory is based on Kirchhoff's hypotheses which are summarized below [4].

1. Straight lines perpendicular to the mid-surface remain straight after deformation.
2. The plate is inextensible, thus, there is no elongation.

3. Straight lines perpendicular to the mid-surface remain perpendicular to the mid-surface after deformation.

The first two assumptions imply there is no transverse normal strain and that the transverse displacement is independent of the z coordinate. The third assumption implies that the transverse shear strains are zero. These assumptions are visually represented in Figure 5.

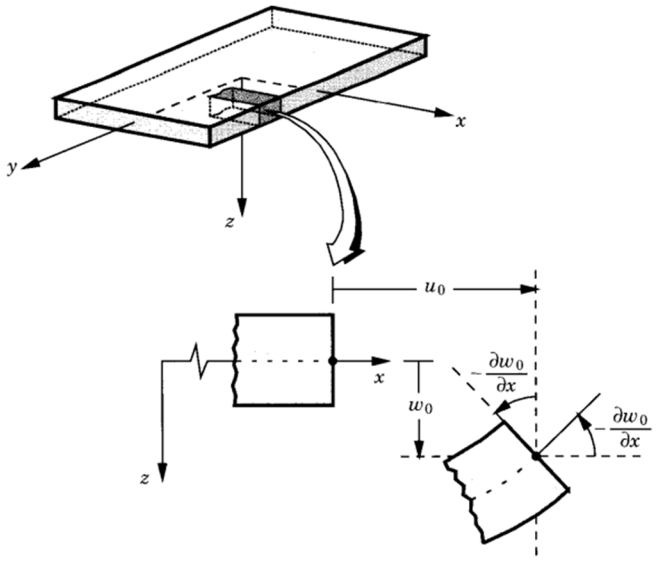

Figure 5: Classical Lamination Theory [4]

By application of these assumptions, the following relation for the force resultant, N, and moment resultant, M, forces can be determined. Through a layer-wise integration, Equation 6 then becomes

$$\begin{bmatrix}\{N\}\\ \{M\}\end{bmatrix} = \begin{bmatrix}[A] & [B]\\ [B] & [D]\end{bmatrix}\begin{bmatrix}\{\varepsilon^0\}\\ \{\varepsilon^1\}\end{bmatrix} \tag{7}$$

where A is the extension stiffness, B is the extension-bend coupling matrix, and D is the bending stiffness defined by Equations 8-10.

$$A_{ij} = \sum_{i=k}^{N} \bar{Q}_{ij}^{k}(z_k - z_{k-1}) \tag{8}$$

$$B_{ij} = \frac{1}{2}\sum_{i=k}^{N} \bar{Q}_{ij}^{k}(z_k^2 - z_{k-1}^2) \tag{9}$$

$$D_{ij} = \frac{1}{3}\sum_{i=k}^{N} \bar{Q}_{ij}^{k}(z_k^3 - z_{k-1}^3) \tag{10}$$

Hence, the strains can be expressed by displacements

$$\{\varepsilon^o\} = \begin{Bmatrix} \frac{\partial u_o}{\partial x} + \frac{1}{2}\frac{\partial \omega_o}{\partial x}^2 \\ \frac{\partial v_o}{\partial y} + \frac{1}{2}\frac{\partial \omega_o}{\partial y}^2 \\ \frac{\partial u_o}{\partial y} + \frac{\partial v_o}{\partial x} + \frac{\partial \omega_o}{\partial x}\frac{\partial \omega_o}{\partial y} \end{Bmatrix} \tag{11}$$

$$\{\varepsilon^1\} = \begin{Bmatrix} \frac{\partial^2 \omega_0}{\partial x^2} \\ \frac{\partial^2 \omega_0}{\partial y^2} \\ 2\frac{\partial^2 \omega_0}{\partial x \partial y} \end{Bmatrix} \tag{12}$$

1.2.2 First Order Laminated Plate Theory

First order laminated plate theory makes the same assumptions as the classical lamination theory except for the third hypothesis. In the first order theory, it does not require the lines to remain perpendicular to the mid-surface after deformation as shown in Figure 6.

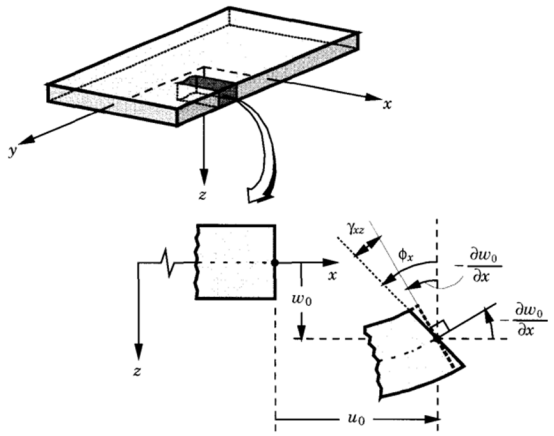

Figure 6: First Order Laminated Plate Theory Deformation [4]

This reduction of assumptions then causes Equation 7 to be statically indeterminate; thus, an additional term is introduced to mitigate this and is called the transverse force resultants {Q}.

$$\begin{Bmatrix} Q_y \\ Q_x \end{Bmatrix} = K \begin{bmatrix} A_{44} & A_{45} \\ A_{45} & A_{55} \end{bmatrix} \begin{Bmatrix} \frac{\partial \omega_o}{\partial y} + \phi_y \\ \frac{\partial \omega_o}{\partial x} + \phi_x \end{Bmatrix} \tag{13}$$

A shear correction factor, K which has been shown to be 6/5 [4], is utilized to accurately represent the transverse shear strains. Similarly to the classical lamination theory, the components of A are defined by Equation 8.

1.2.3 Bending and Buckling Equations

Bending and buckling are two common features of laminated plates. The actual equations for bending and buckling are derived from the equations of motion. For the classical lamination theory, these equations often reduce to a one-dimensional problem such as the Euler-Bernoulli beam theory whereas the first order laminated plate theory reduces to Timoshenko beam theory. Here are presented solutions for the classical lamination theory; the first order theory can be found in [4]. For a laminated plate, the equation of motion, derived from Equation 6, is defined by Equation 14.

$$\begin{bmatrix} 0 \\ 0 \\ q \end{bmatrix} = \begin{bmatrix} c_{11} & c_{12} & c_{13} \\ c_{12} & c_{22} & c_{23} \\ c_{13} & c_{23} & c_{33} \end{bmatrix} \begin{Bmatrix} u_o \\ v_o \\ \omega_o \end{Bmatrix} + \begin{bmatrix} m_{11} & 0 & m_{13} \\ 0 & m_{22} & m_{23} \\ m_{13} & m_{23} & m_{33} \end{bmatrix} \begin{Bmatrix} \ddot{u}_o \\ \ddot{v}_o \\ \ddot{\omega}_o \end{Bmatrix} \tag{14}$$

By expanding Equation 14, the out-of-plane displacement ω can be defined by Equation 15.

$$B_{11}\frac{\partial^3 u_o}{\partial x^3} + 3B_{16}\frac{\partial^3 u_o}{\partial x^2 \partial y} + (B_{12} + 2B_{66})\frac{\partial^3 u_o}{\partial y^2 \partial x} + B_{26}\frac{\partial^3 u_o}{\partial y^3} + B_{16}\frac{\partial^3 v_o}{\partial x^3} + 3B_{26}\frac{\partial^3 v_o}{\partial y^2 \partial x} + (B_{12} +$$

$$2B_{66})\frac{\partial^3 v_o}{\partial x^2 \partial y} + B_{22}\frac{\partial^3 v_o}{\partial y^3} - \left(D_{11}\frac{\partial^4 \omega_o}{\partial x^4} + 4D_{16}\frac{\partial^4 \omega_o}{\partial x^3 \partial y} + 2(D_{12} + 2D_{66})\frac{\partial^4 \omega_o}{\partial x^2 \partial y^2} + 4D_{26}\frac{\partial^4 \omega_o}{\partial x \partial y^3} + D_{22}\frac{\partial^4 \omega_o}{\partial y^4}\right) +$$

$$\widehat{N}_{xx}\frac{\partial^2 \omega_o}{\partial x^2} + \widehat{N}_{xy}\frac{\partial^2 \omega_o}{\partial x \partial y} + \widehat{N}_{yy}\frac{\partial^2 \omega_o}{\partial y^2} + q = I_1\left(\frac{\partial \ddot{u}_o}{\partial x} + \frac{\partial \ddot{v}_o}{\partial y}\right) + I_o\ddot{\omega}_o - I_1\left(\frac{\partial^2 \ddot{\omega}_o}{\partial x^2} + \frac{\partial^2 \ddot{\omega}_o}{\partial y^2}\right) \tag{15}$$

For symmetric laminates, the B matrix is zero thus reducing Equation 15 to a function of the D matrix, laminate moment of inertia (I), and the edge loads ($\widehat{N}$). By solving this differential

equation, the solution for bending and buckling can be determined by applying the appropriate boundary conditions.

For a one-degree-of-freedom problem, the bending solution for a laminated cantilevered beam under a distributed load is defined by:

$$\omega_o = \frac{q_o b a^4}{24 E_{xx} I_{yy}} \left(6 \left(\frac{x}{a}\right)^2 - 4 \left(\frac{x}{a}\right)^3 + \left(\frac{x}{a}\right)^4 \right) \tag{16}$$

The buckling problem reduces to an eigenvalue problem, and the general solution is shown in Equation 17. For a clamped-clamped plate buckling problem, the buckling stress is then defined by Equation 18.

$$W(x) = c_1 \sin \lambda_b x + c_2 \cos \lambda_b x + c_3 x + c_4 \tag{17}$$

$$N_{cr} = \left(\frac{\pi^2}{3}\right) \frac{E_{xx} h^3}{a^2} = \left(\frac{2\pi}{a}\right)^2 \frac{1}{D'_{11}} \tag{18}$$

1.3 Fluid Dynamics of Sliding Plates

In the hot drape forming process, uncured plies undergo inter-laminar shear enabling conformation of a flat charge to tool geometry. This process closely resembles two sliding plates with a fluid boundary between them. This section aims to introduce fluid dynamic principles pertaining to resin flow between plates.

1.3.1 Types of Fluids

Several different types of fluids exist which are classified by their shearing response. A linear shear rate vs. stress is known as a Newtonian fluid and takes the following relation:

$$\tau = \mu \frac{dv_x}{dy} \tag{19}$$

Where τ is the shear stress, μ is the fluid viscosity, and $\frac{du}{dy}$ is the shear strain. If a fluid does not have a linear response, it is known as a non-Newtonian fluid. Non-Newtonian fluids include

responses such as shear thinning, shear thickening, and Bingham plastic. These shear responses are summarized in Figure 7. Under an increasing shear strain, the viscosity of a shear thinning fluid will decrease whereas for a shear thickening fluid the viscosity will increase. These fluids will follow the following relationship.

$$\tau = \eta \frac{dv_x}{dy} \tag{20}$$

Where η is the apparent viscosity and is not necessarily linear. Bingham plastics have a unique response. At low strains, the Bingham plastic behaves as a solid with no flow until the yield shear stress is exceeded. Then the flow response is linear and classified as:

$$\tau = \begin{cases} 0 & | \ \tau < \tau_y \\ \mu \frac{dv_x}{dy} + \tau_y & | \ \tau \geq \tau_y \end{cases} \tag{21}$$

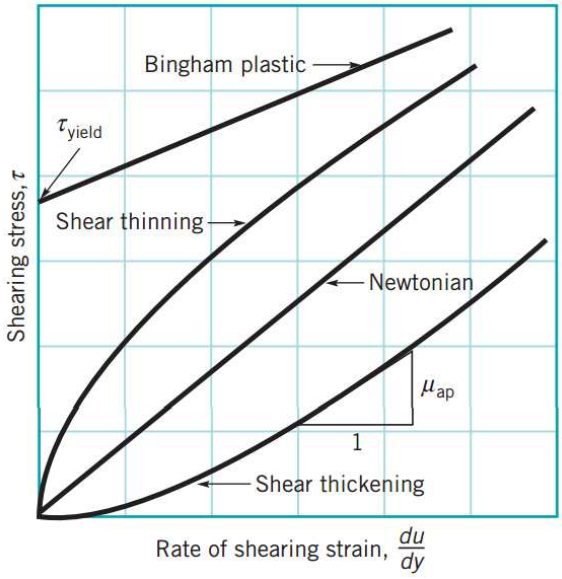

Figure 7: Newtonian and Non-Newtonian Shear Response Curves [5]

1.3.2 Couette Flow

As previously mentioned, during the hot drape forming process, a flat laminate of plies undergoes inter-laminar shear while conforming to a specific geometry. The resin acts as a

viscous layer between the plies while they slip. A simple diagram is shown in Figure 8 where H is the separation between plates. As the top plate moves relative to the lower plate, the fluid at the top plate moves with velocity υ_o while the lower plate fluid remains stationary inducing steady state motion along the x axis.

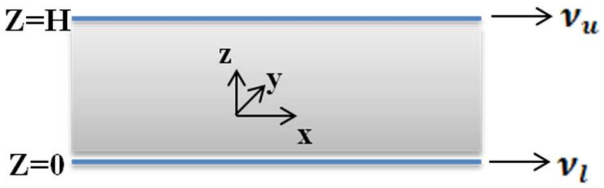

Figure 8: Couette Flow

This situation closely resembles a special case of laminar flow between plates called Couette flow where flow is induced by movement of the plates. In this flow, it is assumed that the pressure gradient between plates is a constant. In the case of drape forming, the resin does not flow independently; rather, flow is induced by inter-laminar shearing thus the pressure gradient is zero. Starting from the Navier-Stokes equation, the fluid velocity profile between plates can be developed.

$$\rho\left[\frac{\partial\vec{V}}{\partial t}+\left(\vec{V}\cdot\nabla\right)\vec{V}\right]=-\nabla P+\mu\nabla^2\vec{V}+\rho\vec{g} \tag{22}$$

Summarizing the above assumptions:

Steady State Flow: $$\frac{\partial\vec{V}}{\partial t}=0 \tag{23}$$

No Pressure Gradient: $$\nabla P=0 \tag{24}$$

Laminar Flow only in x: $$\left(\vec{V}\cdot\nabla\right)\vec{V}=0 \tag{25}$$

Relative Motion: $$v_o=v_u-v_l \tag{26}$$

Thus Navier-Stokes reduces to:

$$0=\mu\nabla^2\vec{V} \tag{27}$$

Since $\vec{V} = v_x\hat{\imath}$, the above equation simplifies to 1D as

$$0 = \mu\frac{\partial^2 v_x}{\partial z^2} \tag{28}$$

Integration yields:

$$v_x = c_1 z + c_2 \tag{29}$$

Using boundary conditions specified in Figure 8,

$$v_x = \frac{v_u - v_l}{H} z + v_l \tag{30}$$

Differentiating with respect to z gives

$$\frac{\partial v_x}{\partial z} = \frac{v_u - v_l}{H} \tag{31}$$

Which then yields

$$\frac{\partial v_x}{\partial z} = \frac{v_o}{H} \tag{32}$$

This shows that the strain rate $\frac{\partial v_x}{\partial z}$ is directly dependent upon the relative velocity of the plates along the x–direction and inversely proportional to the thickness between the plates.

1.3.3 Stribeck Curve

While Couette flow describes the shear response of sliding plates, it assumes that the plates are frictionless. The study of tribology looks at the interactions of surfaces in motion considering friction, lubrication, and wear. One of the fundamental topics in tribology is the Stribeck curve which relates the friction coefficient to the viscosity, sliding speed, and pressure defined by the dimensionless Hersey number (H).

$$H = \frac{\mu v}{p_l} = \frac{\mu\dot{\gamma}}{p} \tag{33}$$

Where η is resin viscosity, v is the velocity at the contact surface, p_l is the linear pressure, $\dot{\gamma}$ is the strain rate, and p is the normal pressure.

The Stribeck curve is divided into three regions: boundary friction, mixed friction, or hydrodynamic friction as shown in Figure 9. The boundary friction regions characteristic low speeds and high pressures cause high friction due to the solid body interaction. On the opposite extreme, the hydrodynamic regime is governed largely by the resin viscosity. As the Hersey number increases with increasing viscosity, the resin layer increases with increasing hydrodynamic pressure which then drives an increase of friction from the local minimum. The final region of the Stribeck curve is the mixed region where a mixture of solid body interaction and hydrodynamic pressure dominate in different positions. With increasing speed, more of the lubrication fluid will dominate lowering the friction coefficient to its minimum at the transition to the hydrodynamic friction zone.

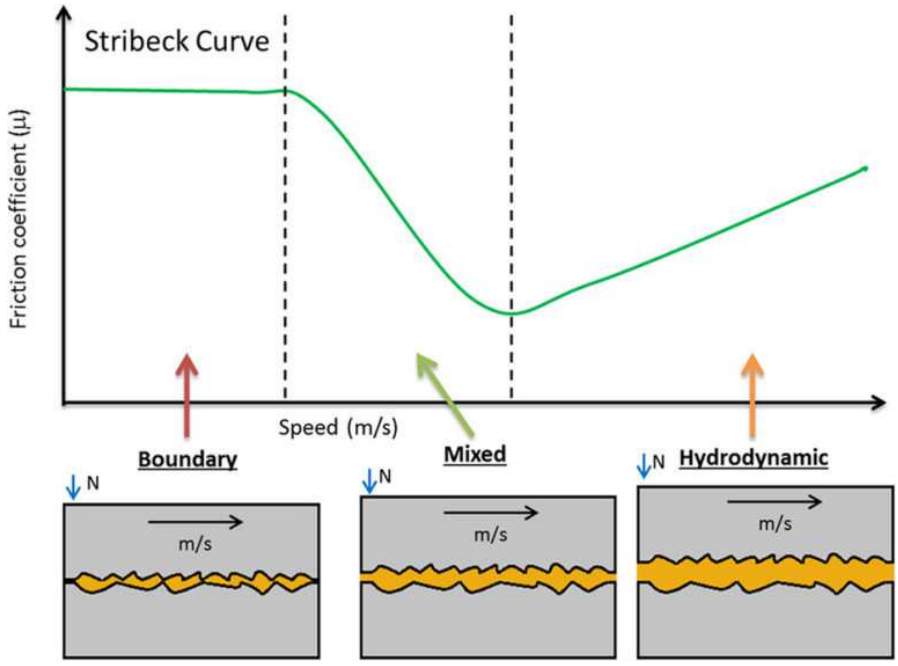

Figure 9: Example of a Stribeck Curve [6]

Chapter 2 – Literature Review

This chapter contains a summary of research into the various components of composite formability. These include composite processing, ply bending, intra-laminar and inter-laminar shearing, drapability, tack, and work focused on drape forming.

2.1 Composite Processing

The use of composite materials has many benefits over metals but also many challenges in processing. Inherent variability of prepreg during manufacturing such as prepreg thickness, resin distributions, and fiber orientations can lead to final part variations [7–10]. Buckling of the fibers is common in both manual hand layup processes and automated processes such as hot drape forming. During curing, the coefficient of thermal expansion within the composite laminate and tool have been shown to cause fiber waviness and residual stresses leading to cured part distortions [11–15].

The effect of wrinkles in composite laminates is well understood to decrease mechanical properties [16,17] including in tension [18–20] and compression [11,21–23]. Further, the effect of wrinkles has been effectively modeled [24–26], yet the driving mechanism behind how these wrinkles form is not well understood. Many mechanisms have been proposed for wrinkle development in single composite layers that consider the interlocking of weave patterns [27,28] and frictional shear stress [29]. Other research evaluating single plies of woven fabric have been evaluated for their ductility, drapability, and intra-laminar shearing [30,31].

Other researchers have looked at the effect of the coefficient of thermal expansion [32–36]. The expansion differential of the tool and composite creates localized tension in the ply adjacent to the tool surface. The friction between the tool and plies has been reported as the influencing property of the force transferred from the tool to part. The decrease of ply tool to ply

friction has been shown to induce wrinkling in female tools where the plies are able to slip and buckle due to excess material.

2.2 Bending

For many automated processes, ply and laminate bending is critical for forming defect-free parts. This is often characterized through cantilever bend tests [37–39] and the Kawabata bending test [40,41]. Others have used a DMA (dynamic mechanical analysis) to characterize the bending of single plies both simply supported and cantilever beam [42,43]. A British standard [44] also further outlines proper procedures to test bending using the cantilever beam test.

Many authors have worked to identify a mathematical model describing the cantilever bend test through many different finite element approaches [37,45–47]. Through a series of iterations, Harrison [47] shows that the results of a bias extension test and cantilever beam test can be closely modeled using modified truss and beam elements. Harrison also reports that the deformation of a ply in a cantilever beam test matches the equation of composite bending presented in the British standard [44] given by:

$$\delta = \frac{f(\theta)}{\frac{\tan(\theta)}{\cos(0.5\theta)}} \frac{\rho g L^3}{8} \tag{34}$$

Where ρ is the ply density, g is the acceleration due to gravity, L is the length of the strip, and θ is the angle of deformation measured from the initial horizontal plane. $f(\theta)$ is described by second order function

$$f(\theta) = (-3.24e-5)\,\theta^2 + (3.87e-6)\theta + 0.99 \tag{35}$$

One limitation to this equation is that it only takes into account the density of a laminate and neglects the inter-laminar shear experienced as individual plies slip over each other.

2.3 Intra-laminar Shear

The most common model of intra-laminar shear is the pin-joint model (PJN) [27]. This model considers intra-laminar shearing and part geometry to determine if wrinkles will initiate. The model considers a woven fabric with a unit cell as shown in Figure 10.

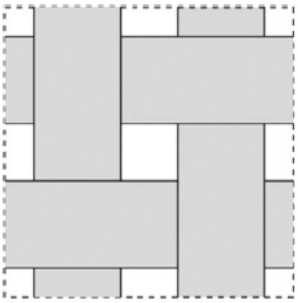

Figure 10: PJN Woven Fabric Unit Cell [30]

The theory states that fibers will not slip at warp and weft intersections. The fibers are also considered inextensible. Thus, the unit cell length cannot change; only the internal angles of the cell can change. The plies are allowed to deform until the critical locking angle, determined by the bias extension test or picture frame test [30,48–51], is reached. At which point, wrinkling will initiate. This flow is depicted in Figure 11.

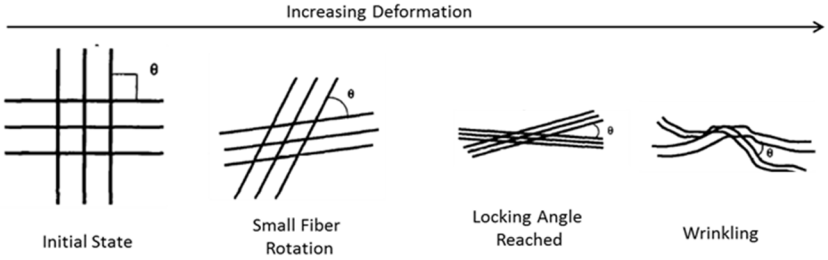

Figure 11: PJN Deformation Schematic (adapted) [27]

Testing for the critical locking angle with the picture frame and bias extension tests has shown that a slight discrepancy exists between testing methods [50]. It was shown that the picture frame approach over-estimates the critical angle due to internal tension developed during the test. By modifying the picture frame test fixture to reduce developed tensions, the results

from the picture frame test more closely align to the bias extension test [50]. A benchmarking of materials and test methods shows variability in the results from different universities [51] due to the test fixtures and methods. Other factors that could influence the tests are variability within the fabric batches. Modeling approaches have been successfully used to simulate the results achieved in picture frame and bias extension tests [48,49,52,53].

Research has also been conducted into the locking angle of different weave types [54–56]. These results have shown that deformation is lowest with plain weaves and increases with twills and is largest with harnesses. This indicates that forming will be better using a harness than a plain weave. During these tests, Sharma, et al. report that the PJN theory underestimates the experimental results [54]. Mohammed, et al. also show that as shear rate increases, the deformability of fabrics lowers [55]. Shear stress in plain weaves was further described by (36), twills (37), and 8HS (38), based upon the shear angle.

$$\tau_{pw} = 2.8e - 3\gamma^5 - 2.77\gamma^3 + 2588.1\gamma \tag{36}$$

$$\tau_{twill} = 0.59\gamma^3 + 569.23\gamma \tag{37}$$

$$\tau_{8HS} = 0.47\gamma^3 + 115.43\gamma \tag{38}$$

Larberg et al. examined the bias extension test on unidirectional fabric laminates and applied the PNJ theory to the results [57]. Two types of defects were observed in this experiment. The thinner materials, reported as 977-2 and 8552, showed visible out-of-plane wrinkles while the thicker M21 material developed voids due to fiber splitting. Each sample set tested exhibited small fiber deformation which was observed as bands. It was shown that lower strain rates resulted in less wrinkling which corresponds to other published research [48,58,59].

The effect of temperature on the load carrying capacity of laminates is as expected. As the viscosity of a resin drops, a lower load will induce inter-laminar shearing. This was

showcased by using M21 fibers. The comparison between the resin systems shows that more than viscosity affects the load to induce intra-laminar shearing. Only considering viscosity, the M21 prepreg would be expected to require the most load to deform, but it requires roughly half that of 8552 and twice that of 977-2. The percent thickness change (debulk factor) can also influence the inter-laminar shearing [59]. In addition to the debulk factor, the resin additives such as thermoplastic particles and level of tack of the systems could have influenced these results.

Larberg, et al. also applied the PJN theory to the data [57]. As previously discussed, the PJN theory is typically applied only to fabric weaves. By applying the PJN theories to unidirectional laminates, the authors are investigating at how well debulking can induce pivot positions at fiber crossovers. Interestingly, the M21 fabric correlated closely with the PJN theory until 40 mm of deformation while the other materials did not correlate. This seems to suggest that the various resin systems, fiber types and sizes, and inter-laminar slipping play a role in intra-laminar slipping.

2.4 Drapability

Drapability is often defined by the ability of a material to conform to a specific geometry. Many different methods have been used to characterize prepreg drapability using several different tools such as tetrahedral [60] and hemispheres [61–64]. General drapability tests are performed on dry fibers without impregnated resin. This type of study greatly affects many different processes such as stamp forming, liquid compression molding, and drape forming. Often the PJN theory is used as the base model to characterize the deformation of laminates [65,66] with good adherence. Other authors have looked at more advanced finite element models that show improved accuracy to experimental results [67–70].

Through a series of experiments and modeling, Allaoui, et al. identify several factors that affect ply drapability and conclude that the thickness of the laminate or ply and speed of testing play vital roles in testing [60]. Boisse, et al. also show that the bending stiffness of the fibers influence the drapability [71]. Wang, et al. looked at the drapability of impregnated fibers and found that the initial point of contact of fibers is a large influencing parameter for drapability of a rudder tip, D-rib, nose rib, sine wave rib, and flap panel [67].

Several authors have considered the dry weave architecture's effect on forming [72–75] . Mohammed, et al. compared the effect of plain weave, twill, and five harness satin architectures [72]. In this experiment, Mohammed, et al. report that the fiber-locking angle is smaller in drape tests than picture frame tests. Experimental results also show that the harness has the most drapability, followed by the twill, plain weave. As expected, a comparison between plain weaves shows that a looser weave will deform more easily than a tight weave [72] corresponding well to the effect of the locking angle in different weaves [54–56].

2.5 Tack

Prepreg tack describes the adhesive force of a resin to a substrate. Typical prepregs are available in a variety of tack levels ranging from high to low. Challenges arise when quantifying the tack level of a prepreg. Prepreg manufacturers quantify the tack through a touch test. In which a technician qualitatively assigns a tack level to the prepreg based upon how well the material sticks to the testing instrument. Manufacturers have fine tuned the resin chemistry blend to produce the desired tack level consistently.

Problems arise with the user of the prepreg as humidity and out-time can change the tack level of the prepreg from the manufacturers' produced level. Recent work by RJ Crossley of the University of Nottingham has developed a test fixture to quantitatively determine a prepreg's

tack level [76] applied for automated tape laying. In their test, a prepreg strip was adhered to a plate and the force required to remove the prepreg was recorded resulting in a fiber stiffness and tack portion. Many factors were found to influence the reliability of the test. The cleanliness of the test plate during the test was the largest influencing factor. The temperature and humidity also played a lesser affect on the tests.

Besides the influencing factors, the test was successfully able to identify the tack levels of commercial prepregs. The article did report tack variability based upon sample testing position. Samples removed from the center of a prepreg roll possessed higher tack than the samples removed from the edge. The authors attribute this variation to the prepreg production method. During the production of prepregs, often liquid resin is deposited across the width of a prepreg roll, and rollers are used to equally distribute the resin.

One interesting result reported was that the tack is influenced differently by varying temperatures across prepreg systems tested [76]. Of the two components the test measured, the fiber stiffness universally decreased based upon temperature. The tack tended to increase among low tack and automated tape laying (ATL) prepreg samples but was shown to decrease on the high-tack sample. Between the two increasing samples, the tack for the ATL peaked then decreased while the low-tack sample converged at a maximum tack level. The variation of tack corresponded with the failure mode of the prepregs. The high-tack sample failed cohesively while the low-tack prepregs failed interfacially. The ATL exhibited interfacial failure below its tack peak while after the peak, cohesive failures occurred.

2.6 Inter-laminar Shear

Inter-laminar shearing is a vital factor inducing forming as it defines how easily plies are capable of slipping past one another. Successfully forming complex parts require the material to

conform to features such as joggles and curvature. Insufficient shearing will induce: in-plane and out-of-plane wrinkles [1,32,77] and poor consolidation [78]. Insufficient shearing will cause plies to undergo axial compression. Because the width to thickness ratio of the plies is large, the out-of-plane buckling predominates over in-plane buckling [77]. Thus characterizing the intra-laminar slippage influences process modeling [71,77] which then can be applied to improve manufacturing processes.

Several authors have worked to characterize the inter-laminar shear or friction of prepregs [36,51,79–81]. All authors used a derivation of the test rig presented in Figure 12 and reported shear variations between prepreg types and batches. All papers reported that the inter-laminar shear reaches a local maximum in a temperature sweep tested following a convex trend and is due to a combination of the resin lubricating the interface and the fiber to fiber friction. Besides the resin lubrication, factors such as the thermoplastic toughening method of prepregs, rate, and temperature can greatly influence the inter-laminar slip [80,82–84].

The fixture presented in Figure 12, is designed to fit into a standard Instron and tested in an environmental chamber. Prepreg is applied to the clamps (iii) and the base plate (iv) and a consolidation pressure applied by an actuator (ii). The limitation of this fixture is the constant pressure applied to both clamps and uniformly controlling the displacement of the clamps. Test results show that there are two regimes: pre-slip and post-slip. The pre-slip, static friction, and the post slip, dynamic friction, are a function of both rate and pressure. The inflection point between the two regimes is dependent upon temperature and the consolidation pressure [81,85].

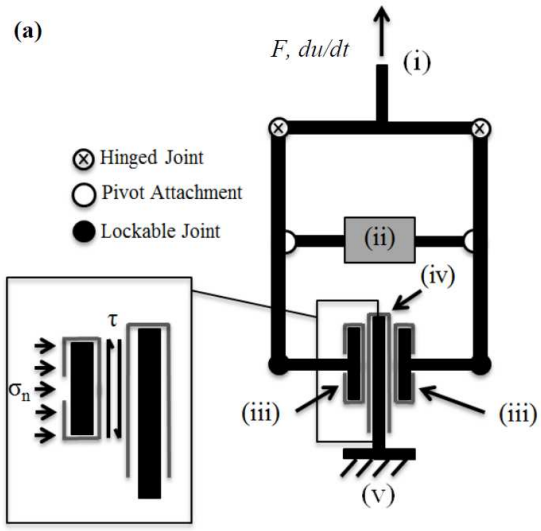

Figure 12: Inter-laminar Shear Test Fixture [81]

2.7 Models

Martin and Seferis first calculated a single coefficient of static friction [79]. Current modeling approaches have generally considered flow compaction models derived from a Darcy flow approach [86,87] or a kinetic approach such as the PJN theory [27,88–90]. Short comings of these models are that they cannot fully capture the influence of layering due to inter-laminar shear. Several different results have been reported from the inter-laminar slip. Larberg, et al. [80] derives a single coefficient of friction using a tribology model. Erland, et al. [81] consider a viscoelastic-plastic model while other authors consider the slip elastic [91].

Dodwell, et al. have proposed two different approaches for modeling consolidation. A first order-energy method [77] and a Cosserat continuum model based from geological models [42,92].

2.7.1 Kinetic Model

Laminate forming can be modeled kinematically by strain mapping and identification of material properties [29,88,90]. In essence, it assumes that a flat laminate can conform to any

shape through bending and in-plane shear [90]. It is assumed that out-of-plane wrinkles are induced through fiber buckling. Pandey, et al. [58] suggest two models that describe laminate wrinkling. One is based on an energy method and the other as an eigenvalue problem. While the models lack a correlation to experimental results, the models do suggest that a thicker laminate will have a higher tendency to wrinkle.

Researchers investigating the c-channel shape using a Gauss – Bonnet theory show that a c-channel can fit the theory indicating that the fibers follow a Gaussian curve [29]. It does show, however, that the joggle is a heavily sheared area. The width of the joggle shear band is defined by

$$\gamma = L_j|\sin(\theta - \alpha)| \tag{39}$$

Where L_j is the length of the joggle, θ is the ply orientation, and α is the joggle angle. This helps understand the full effect of the joggles. Increasing the shear band will increase the likelihood of wrinkles occurring.

Gutowski, et al. present an energy approach [88] in which the total strain energy is defined as a function of the composite and diaphragm.

$$\Delta U = \Delta U_{diaphram} + \Delta U_{composite} \tag{40}$$

The strain energy of the composite is

$$\Delta U_{composite} = \int_0^L \frac{M^2}{2EI} dx \tag{41}$$

The critical load for wrinkle initiation for a double diaphragm forming model is defined by

$$P_{critical} = 2F_{diaphram} + \frac{KE(t)I}{L^2} \tag{42}$$

In which the $F_{diaphram}$ is the force at which the diaphragm is pulled, L is the fiber length, K is a fitted constant, and E(t) is the time dependent modulus. The in plane shear is defined through a geodesic curve.

$$\int_c \ k_g \, ds + \iint_R \ K \, dA = 2\pi - \sum_{i=1}^{M} \theta_i \tag{43}$$

Where K is a function of part shape, and θ_i is the initial fiber orientation. Gutowski further determines the shear along a curved c-channel's inner and outer flange. Based upon the fiber length (l)

$$l_{inner} = \ 2R_1 \sin(\Gamma_{12}) + (S_n - R_1)\Gamma_{12} \tag{44}$$

$$l_{outer} = \ 2R_2 \sin(\Gamma_{12}) + (S_n - R_2)\Gamma_{12} \tag{45}$$

in which R_i is the inner and outer radius, and S_n is the distance down the flange. While these are intra-laminar slippage, the inter-laminar shear (Γ_{13}) can be inferred. While this is a double diaphragm forming model, the influencing parameters for the material can be observed for a normal drape forming situation. Gutowski, et al. calculate that the inter-laminar shear(Γ_{13}) is 10^3 to 10^4 times larger than the intra-laminar shear (Γ_{12}). In the case of double diaphragm forming, the diaphragm elongation is the main support preventing out-of-plane wrinkling. Whereas the hot drape forming process has only one diaphragm allowing for out-of-plane wrinkling to more easily occur. While these models are somewhat limited, they provide the foundation for advanced modeling techniques using FEA based approaches which include using different beam models [37] and also a combination kinetic/Tribology approach [93,94].

2.7.2 Tribology Model

Composite laminate sheets are separated by layers of resin. This closely resembles a state of tribology of hydrodynamic friction. Thermoplastic composites are well understood [93,94]. The friction of the prepreg is influenced both by the tool-to-ply friction and the inter-

laminar shearing. The tool-to-ply friction has been modeled using a thin film lubrication derivation from Reynolds equation. The inter-laminar friction is determined by fitting the following shear and viscosity equations to experimental data [93].

$$\tau = \tau_o + a(p + p_o)^b \frac{\vec{\gamma}}{h} \mu \tag{46}$$

Where p is the normal pressure, h is film thickness, μ is the viscosity determined by the cross viscosity model, and $\vec{\gamma}$ is the shear vector. The remaining parameters are fitted to experimental data. The cross viscosity model defines viscosity as

$$\mu = \frac{\mu_o}{1+(C\gamma_{eq})^n} \tag{47}$$

Where γ_{eq} is the shear rate and the remaining parameters are fitted to experimental data. While this approach works well for thermoplastic materials, Larberg, et al. [83] has shown that thermosets do not behave purely hydrodynamically. Several authors have verified that the friction of thermoset prepregs follow the mixed region of the Stribeck curve [36,79,95,96].

Larberg tested several unidirectional prepreg systems and found that several factors influence the friction coefficient. Among the material systems, a minimized friction was observed at a slight normal pressure indicating the transition from hydrodynamic to mixed regions of the Stribeck curve. The rate of testing also influenced test results for three of the four material systems further indicating that each resin matrix will behave differently. The toughening method, surface roughness, and viscous resin layer thickness are also major influences on the measured friction. Larberg showed that as temperature increases, the friction increases while the viscosity decreases. This may be due to the consolidation of plies causing fiber – fiber interactions to become more dominate.

2.7.3 Viscoelastic Model

A one-dimensional viscoelastic model [81] was developed from the inter-laminar shear tests, and several key parameters were developed from the tests. The static friction zone is defined as

$$\tau = K\gamma \tag{48}$$

where τ is the shear stress and γ is the shear strain. K is the rate dependence shear stiffness as defined in

$$K = (K_t + \eta \frac{d\gamma}{dt}) \tag{49}$$

$$\frac{d\gamma}{dt} = \frac{R}{Rt+h} \tag{50}$$

where R is the displacement rate, h is the ply thickness, and t is time. Post slip, the dynamic friction zone is defined as

$$\tau = K_t\gamma + \tau_c(1 - \frac{K_t}{K}) \tag{51}$$

where K_t is the constant shear stiffness and τ_c is the critical shear stress at which slip occurs. τ_c can be calculated using the Mohr-Coulomb friction model in which μ is the coefficient of friction, σ_n is the normal force, and j is the joint strength.

$$\tau_c = \mu\sigma_n + j \tag{52}$$

Experimental results show how the shear modulus varies during testing [85]. The rate dependent shear stiffness, K, increases as ply angle is varied from 0° to 45°. On the other hand, the constant shear stiffness, K_t, decreases to a local minimum at 45°. One explanation is that the K is influenced largely by the resin while K_t is fiber dominated. As the test angle varies, the resin is able to pool at the fiber junctions effectively increasing K. At the same time, the contact area of the fibers or packing density is decreasing which then decreases K_t.

The effect of temperature on the modulus is also different. The rate-dependent modulus decreases with increasing temperature whereas the constant modulus reaches a local maximum then decreases as temperature increases. The increase in K_t confirms data reported in [81] but no explanation is provided as to how this phenomenon might occur.

Considering the critical shear stress, τ_c, it was shown that the joint strength, j, dominates at low temperatures whereas μ dominates at higher temperatures [81]. These results were shown using AS4/8552 which has only surface impregnation and, thus, resin rich areas. The lower temperature forces shearing in the resin rich areas; thus, the joint strength is the influencing factor. As temperature increases, the resin viscosity drops which begins to act as a lubricant. The normal pressure then consolidates the fibers causing the fiber-to-fiber friction to dominate as the resin flows from the joint.

Larberg, et al. [80] and Erland, et al. [81] both show that post yield hardening occurs during shearing. Erland suggests that this is due to the resin viscosity and rate dependence. At low rates and high resin viscosities, the joint can reform after the initial slip has occurred thus allowing a combination of j and μ to influence the transition zone. Follow up tests performed by Dodwell, et al. [77] show that a faster deformation rate eliminates the post yield hardening. It is important to note that this phenomenon is observed in a material with engineered vacuum channels. It is currently unknown if this post-yield hardening will affect fully impregnated materials or other generations of prepregs as their shear characteristics vary among generations [80].

2.7.3.1 Application to Composite Laminates

The viscoelastic model presented in [42,85] has been applied to the consolidation of a prepreg stack over a radius. In this model, the shear and slip were calculated based upon the

thickness of the fiber thus designing the model around the laminate rather than a variable interface. The interaction of the fiber and shear thickness is defined as the laminate shear stiffness, S.

$$S = \frac{S_{int.}h}{h_{int.}} \tag{53}$$

Where S_{int} is the shear modulus of the interface, h_{int} is the height of the interface. And h is the total thickness of one fiber and interface.

$$h = h_{int} + h_{fib} \tag{54}$$

The applied study looked at compaction over tool radius and drape forming a composite charge onto the same radius. It was found that the shear strain for the consolidation scenario is a function of the flange angle, θ, and debulk state, α.

$$\gamma_{con} = \ln((1 - \alpha)\theta) \tag{55}$$

But in the consolidation scenario, only the flange angle is an influencing factor.

$$\gamma_{form} = \ln(1 + \theta) \tag{56}$$

Based upon the applied models, the required shear strain can be determined for each scenario. The simple consolidation required minimal deformation is largely influenced by the static friction region of the inter-laminar shear test and thus the rate dependent stiffness parameter. By application of the presented results in [85], minimization of the cross ply angles and increased consolidation temperature produce the best results.

The required shear strain to drape form the radius is much larger than consolidation, therefore, the dynamic friction region of the inter-laminar shear tests dominates. To minimize K_t and τ_c, thus, improving inter-laminar slip, it would be important to maximize the fiber angles such as an isotropic layup of 0/45 fibers and increased temperature. Interestingly, these results

seem to contradict the work published by Hallander, et al. [1] stating that minimizing the 0° and 45° ply interactions improves the drapability of a laminate.

2.7.4 Energy Model

Dodwell used an energy approach to determine influential process parameters on ply consolidation over an external radius. He showed that a critical pressure is required to induce shearing. If the consolidation pressure is not sufficient the laminate buckles. The work further derives a critical flange length. In which any flanges larger than the critical length will produce wrinkles

$$L_c = \frac{P_c}{\tau} \tag{57}$$

In which L_c is the critical length, P_c is the total critical load for each ply, and τ is the shear stress. Dodwell uses two approaches to determine the shear: coulomb friction and elastic model.

Based upon the modeling parameters, several influencing parameters on wrinkle development have been determined. An increase of the bending stiffness will reduce the wrinkle wavelength and thus overall wrinkling in a radius. The critical flange length is largely influenced upon the thickness of the material. Thicker portions of the laminate require a longer critical length due to larger required book ends causing a higher tendency to wrinkle. Dodwell experimentally confirmed that a thicker laminate will have a higher tendency to wrinkle in the radius than a thinner laminate.

2.7.5 Cosserat Continuum Model

Dodwell, et al. also applied a cosserat continuum model to composite forming [42,92]. Cosserat models are typically utilized in geological modeling for granular, masonry, or

sedimentary features [97–107]. Thus, the model may describe a layered composite laminate closely. Based upon Dodwell's derivations, the governing stress tensors are below.

$$\begin{matrix}\sigma_{11}\\ [\sigma_{33}\\ \sigma_{13}]\\ \sigma_{31}\end{matrix} = \begin{bmatrix} C_{1111} & C_{1133} & & 0 & \\ C_{3311} & C_{3333} & & & \\ & 0 & & C_{1313} & C_{1331} \\ & & & C_{3113} & C_{3131} \end{bmatrix} \begin{matrix}\gamma_{11}\\ [\gamma_{33}\\ \gamma_{13}]\\ \gamma_{31}\end{matrix} \tag{58}$$

$$\begin{bmatrix} M_{21} \\ M_{23} \end{bmatrix} = \begin{bmatrix} D_{2121} & 0 \\ 0 & 0 \end{bmatrix} \begin{bmatrix} k_{21} \\ k_{23} \end{bmatrix} \tag{59}$$

In which the material constants C and D are functions of ply bending and shear and further defined in [42]. These properties are determined through a series of inter-laminar shearing tests using the fixture presented by Erland [85]. Ply bending tests were performed using a DMTA in 3 point bending and cantilever. Dodwell further fits a Timoshenko beam theory to the generated material data using a shear correction factor

$$u = f_{max}[\frac{l^3}{3B} + \frac{6l}{5bhQ_p}] \tag{60}$$

In which both B and Q are temperature dependent functions such that

$$B = B_0 \exp(\frac{E_b}{RT}) \tag{61}$$

$$Q_p = Q_0 \exp(\frac{E_p}{RT}) \tag{62}$$

Where R is the universal gas constant and T is temperature in Kelvin. Experimental testing showed a close correlation to predicted results in the case of a DMA laminate test [42], small scale demonstration article [42], a multilayered beam (cantilever deformation and buckling) [92], and consolidation over a corner radius [92].

2.8 Experimental Drape Forming

Hallander, et al. further explored the effect of layup orientation on c-channel's joggle geometries and showed that the plies in the joggle region were locally under compression [1].

The objective of this research was to investigate two hypotheses. The first hypothesis is that local compression exists in the joggle region of a spar. The second hypothesis is that the [0/45] ply interactions reducing inter-laminar shearing increasing defect initiation. The joggle region, depicted red in Figure 13, is a challenging region of the spar during hot drape forming. After the laminate is heated, the flat laminate is sheared to form the web and flanges. The individual plies must be capable of inter-laminar shearing and intra-laminar shearing to conform to the flange and joggle recess. The longitudinal (0) oriented plies tend to create the largest issue by bridging across the joggle recess. If the inter-laminar shearing is not sufficient, off-angle wrinkles will occur as the 0 ply is forced into the recessed area, as outlined in Figure 13.

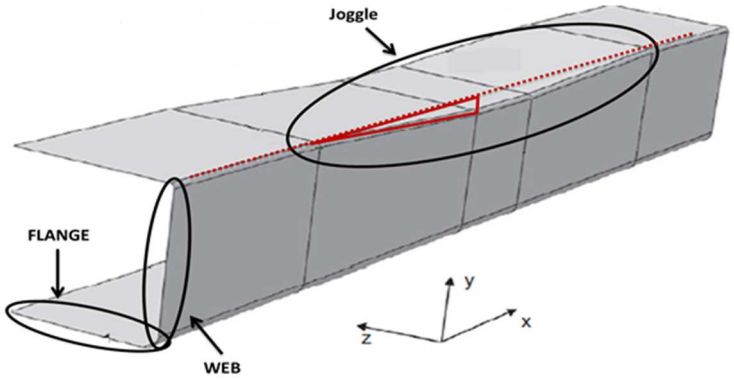

Figure 13: Joggled C-Channel (adapted) [1]

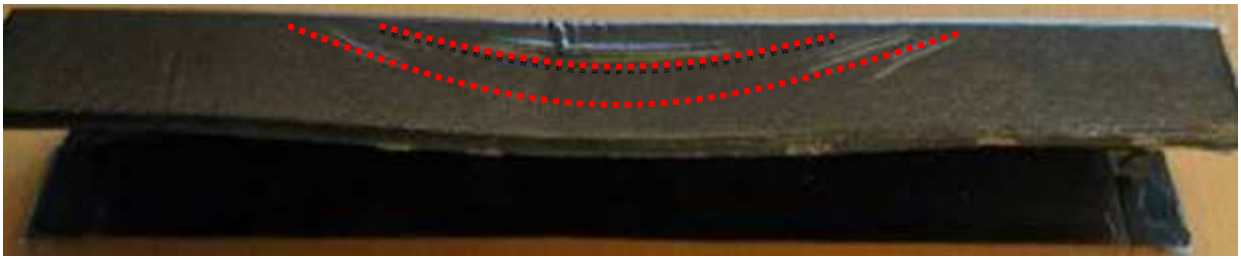

Figure 14: Common Off-Angle Wrinkles of Joggled C-Channel (adapted) [1]

Unidirectional carbon-epoxy laminates were drape formed with multiple replicates on a joggled tool with 20:1 joggle (length: instep). All tests were performed at 65°C. Investigated parameters included ply thickness, layup configuration, material impregnation, and fiber

modulus. The three different layups were designed to promote different amounts of shearing with a baseline quasi-isotropic layup. Different ply counts were also tested with the total laminate thickness a constant variable. These tested parameters are outlined in Table 1.

Table 1: Hot Drape Forming Experimental Design (adapted) [1]

Material	Thickness (mm)	Layup Configuration	Impregnation	Replicate
977-2	0.262	$[(45/0/-45/0)\cdot 2]_s$	Full	3
977-2	0.131	$[(45/0/-45/0)\cdot 4]_s$	Full	3
977-2	0.262	$[(45/0/-45/0)\cdot 2]_s$	Surface	3
977-2	0.131	$[(45/0/-45/0)\cdot 4]_s$	Surface	3
977-2	0.262	$[(90/45/45/-45/-45/90/0/0)]_s$	Full	3
977-2	0.131	$[(90/45/45/-45/-45/90/0/0)\cdot 2]_s$	Full	3
977-2	0.262	$[(90/45/45/-45/-45/90/0/0)]_s$	Surface	3
977-2	0.131	$[(90/45/45/-45/-45/90/0/0)\cdot 2]_s$	Surface	3
977-2/HF	0.131	$[(45/0/-45/90)\cdot 4]_s$	Surface	1
977-2	0.131	$[(45/0/-45/90)\cdot 4]_s$	Surface	1

This experimental design is a 2^3 full factorial design with the added quasi-isotropic layups for a baseline. This design is functional to compare the interaction of all the parameters but is labor intensive. The location of defects, height of defects, and deformation of outermost ply were measured.

To investigate his first hypothesis, Hallander et. al [1], investigated the use of micro computed tomography (CT) analysis to determine if a ply was locally under compression. The micro CT was able to detect density changes in the cured plies of the composite which correspond to localized fiber density increases or decreases caused by localized stresses. The authors found that the local compression stresses existed in the joggle regions of all layup types. More intra-laminar fiber distortions were observed in the layups with [0/45] interactions. These results support the assumption that localized compressive stress exists in the joggle region. The use of micro CT as a nondestructive test can be utilized to understand fiber distortions in parts and also identify areas that recesses or slits could relieve the compressive stresses.

Several correlations were observed between the parameters and wrinkle development. A larger outer ply deformation decreases the severity of defect development. This correlates well to the impregnation level of the fabric showing that full impregnated fabrics have higher friction than fabrics with surface impregnation and result in larger wrinkles. The layup also impacts wrinkle development: layups possessing more +45,-45 pairs shear more when compared to 45,0 pairs. Larberg [57] investigates the intra-laminar shear between +45,-45 pairs via a bias extension test. At low strains, the UD laminate follows the predicted distortion of the pin joint network (PJN) theory but deviates at higher strains. Increasing the inter-laminar friction between pairs of plies will cause the ply set to deform via intra-laminar shear instead of inter-laminar shear improving the formability of some geometries [108]. Additional work to vary the local forces of the laminate successfully considered relieving the local stresses by darting specific plies resulting in minimized wrinkles [3]. Using Aniform modeling software, a numerical model was developed using experimentally determined material properties. Modeling the experimental hot drape forming trials shows good correlation to the numerical model [109].

CHAPTER 3 – OBJECTIVES AND HYPOTHESES

The purpose of this research is to characterize the effect of inter-laminar shearing on out-of-plane wrinkle development on c-channel geometry with double joggles. By fully understanding the influence of ply shearing, a better understanding of the influence of processing and material parameters upon the out-of-plane wrinkle development. Further this knowledge can be applied to screen new materials to identify process parameters using small samples of a material reducing expensive experimental process optimization.

This research investigated material based parameters including fabric architectures and fiber twist and process parameters including processing temperature and forming rate.

Several hypotheses were investigated to support this research. The null hypotheses are outlined below.

H_1: Material tack grade does not affect the inter-laminar friction at temperatures above room temperature. Thus lowering the tack level will not influence out-of-plane wrinkling at elevated temperatures.

H_2: Fiber twist plays a major factor on inter-laminar shearing. By eliminating fiber twist, the inter-laminar shear will decrease effectively reducing out-of-plane wrinkling compared to similar c-channels formed with twisted fabrics.

H_3: The drapability of a ply in a laminate is not affected by inter-laminar effects. Thus 8HS laminates, which show improved ply drapability over PW plies and tapes plies, will produce fewer wrinkles than similar tape or PW laminates.

H_4: Lowering the resin viscosity by forming at higher temperatures, without initiating resin cure, will reduce out-of-plane wrinkle development and show that an optimum resin viscosity will exist for drape forming.

H_5: A direct correlation exists between inter-laminar shearing and out-of-plane wrinkle development. Decreasing the inter-laminar shearing will reduce out-of-plane wrinkling. This correlation can be modeled using laminated plate theories.

CHAPTER 4 – MATERIALS AND METHODOLOGY

In order to achieve the objective and test the hypotheses of this experiment, several experiments were conducted. The materials, methods, and the design of experiments are outlined in this chapter.

4.1 Materials

Two resin systems were utilized in this experiment: Cycom 970 and Cycom 5320-1. Both resin systems were acquired from Solvay and all fibers utilized a T650 fiber. Three product forms of Cycom 5320-1 system were used unidirectional tape (UD), plain weave (PW), and an eight harness (8H). Only PW was investigated using the Cycom 970 but various fiber architectures were investigated. These materials included a standard twisted fiber with 8 twists per meter using a high tack formulation of Cycom 970 (970 HTST), and a fiber with no twists with a low-tack (970 LTNT) variation of Cycom 970. The manufacturers recommended working life of Cycom 970 is 10 days and Cycom 5320-1 is 20 days. All tests were conducted within the recommended out-time of material.

4.2 Experimental Design

The experimental designs for the inter-laminar shear tests and experimental hot drape forming are outlined in the preceding sections.

4.2.1 Inter-laminar Shear and Tack Testing

The inter-laminar shear tests, which partially addressed Hypotheses 2 and 4, focused on screening 5 influencing variables: fiber twist, temperature, pressure, displacement rate, and ply orientation using Cycom 970 PW LTNT and HTST. A Taguchi method was applied to the experiment to reduce the number of testes to 44 tests per fiber twist. One replicate

was performed for each combination and replicates were performed at key design points as listed in Table 2. Variable ranges were chosen to correspond to the experimental process variables in Table 6 and laminate layup in Table 8. Pressure ranged from 0 to 48 kPa which was lower than reported in [81,85]. This was chosen due to the difference in processing pressures seen in hot drape forming compared to autoclave debulking.

Previous work studied the effect of ply consolidation in cure thus higher pressures were necessary to test to mimic the autoclave processing. During drape forming processes, the bulk of forming occurs at low pressures with the part completely formed at 48 kPa. Each 970 material was tested according the experimental plan detailed in Table 2.

Table 2: Inter-Laminar Shear Tests

Temperature (°C)	**Displacement Rate (mm/s)**	**Pressure (kPa)**	**Base plate Orientation (°)**
22	0.85	0	0
22	0.21	0	0
22	0.42	0	0
22	0.21	0	0
22	0.85	0	0
22	0.04	0	0
49	0.04	48	0
49	0.21	48	0
49	0.85	0	0
49	0.21	0	0
49	0.42	24	0
49	0.42	24	0
49	0.85	48	0
49	0.42	24	0
60	0.85	24	0
71	0.04	0	0
71	0.42	48	0
71	0.85	0	0
71	0.42	24	0
71	0.21	0	0
71	0.85	48	0
71	0.04	48	0
71	0.85	48	0

71	0.21	0	0
22	0.85	0	45
22	0.85	0	45
22	0.42	0	45
22	0.21	0	45
22	0.04	0	45
22	0.04	0	45
49	0.04	0	45
49	0.85	0	45
49	0.21	0	45
49	0.42	24	45
49	0.42	24	45
49	0.21	48	45
71	0.04	24	45
71	0.04	0	45
71	0.85	0	45
71	0.42	24	45
71	0.85	48	45
71	0.21	48	45
71	0.85	48	45
71	0.21	24	45

Tack tests, which addressed Hypothesis 1, were performed using 970 LTNT and HTST focusing on two variables: temperature and displacement rate. A Taguchi method was applied to reduce the total number of tests to 21 per tack level. One replicate was performed at each design point and three replicates were tested at specific design points. The experimental design is presented in Table 3.

Table 3: Tack Tests

Temperature (°C)	Rate (mm/s)
22	0.21
22	0.42
22	0.42
22	0.85
22	0.85
22	0.85
38	0.42
38	0.85
38	0.85
49	0.21
49	0.42
49	0.42
49	0.42
49	0.85
60	0.21
60	0.85
71	0.21
71	0.42
71	0.85
71	0.85
71	0.85

4.2.2 Bias Extension Testing

Bias extension tests were performed to determine the locking angle between ST and NT fibers. Both room temperature 970 HTST and LTNT samples were tested.

Table 4: Bias Extension Test Matrix

Fabric Weave	Replicates
970 LTNT	3
970 HTST	3

4.2.3 Hot Drape Forming

The first test conducted addressed Hypothesis 3. In order to perform this analysis, Cycom 5320-1 UD, PW, and 8HS prepregs were be evaluated. Tests were formed at 52 °C chosen as 50% of the T_g from the manufacturer's data sheet. Of the three tests, two replicates were formed for the UD and 8H. While the PW spar did not have a replicate, multiple PW spars tested in further experiments with Cycom 970 confirmed the results observed.

Table 5: Evaluation of Weave Architecture

Resin System	Fabric Weave	Ply Count	Temperature (°C)	Replicates
5320-1	UD	18	52	2
5320-1	PW	18	52	1
5320-1	8H	18	52	2

A reduced factorial design was developed to test wrinkle development helping to support Hypotheses 2 and 4. Using a Cycom 970 PW LTNT and HTST variation, several factors affecting out-of-plane wrinkle development were evaluated including: the fiber twist, tack level, ply count, and test temperature. The effect of ply count on out-of-plane wrinkle development was also investigated. Each observed wrinkle was measured as outlined in Figure 26.

Table 6: Evaluation of Fiber Twist, Tack Level, and Temperature

Resin System	Fabric Weave	Ply Count	Temperature (°C)	Replicates
970	PW-ST	10	60	1
970	PW-ST	18	60	1
970	PW-ST	30	22	1
970	PW-ST	30	38	1
970	PW-ST	30	49	1
970	PW-ST	30	60	2
970	PW-ST	30	71	1
970	PW-ST	30	82	1
970	PW-NT	30	22	1
970	PW-NT	30	38	2
970	PW-NT	30	49	2
970	PW-NT	30	60	1
970	PW-NT	30	71	1

4.3 Methodology

The experimental methods for the bias extension testing, inter-laminar shear testing, and experimental hot drape forming analysis are outlined herein.

4.3.1 Bias Extension Testing

Bias extension test samples were cut from broad goods to a ±45 orientation. Samples were cut to have a gauge length of 152 mm and width of 76 mm. Grip plates were placed at either end of the specimen, Figure 15A. The specimens were transferred to the Instron with the backing film in place to minimize any distortion due to handling, Figure 15B. The samples were aligned into the pneumatic grips and the backing film was removed when correctly placed, Figure 15C.

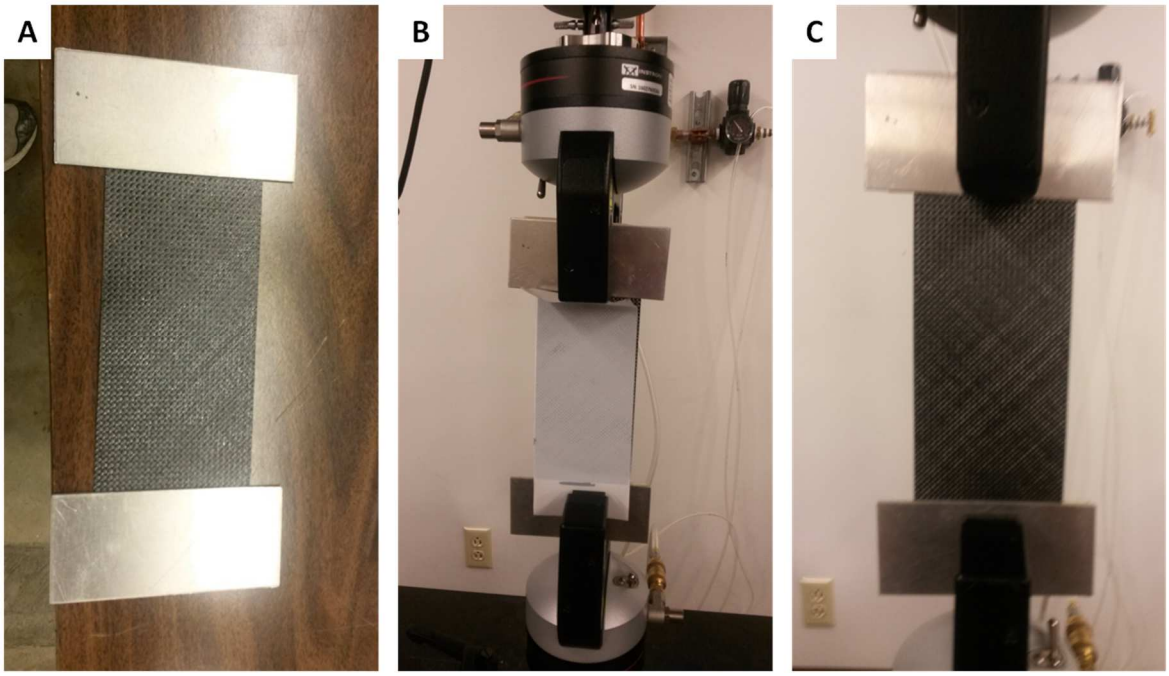

Figure 15: Bias Extension Sample Preparation and Installation

Tests were conducted at Washington University in St. Louis using an Instron Model 5583 with a load cell of 500 N. All tests were performed at room temperature and with a displacement rate of 0.21 mm/s.

4.3.2 Inter-laminar Shear and Tack Testing

4.3.2.1 Test Fixture

A bespoke fixture was developed to test inter-laminar shear and tack which was derived from the fixtures referenced in [76,81]. This fixture, Figure 16 and Figure 17, was designed to fit onto a standard Instron tensile tester and operate outside a climate chamber. Heat was applied through a heating blanket residing under the test platform. External pressure is applied through a spring with a fixed spring constant of 1.5 kg/mm. Standoff blocks were also produced to regulate the pressure to 0, 24, and 48 kPa for inter-laminar shear tests. The slide can be locked in place for the inter-laminar shear tests and translate easily for the tack tests.

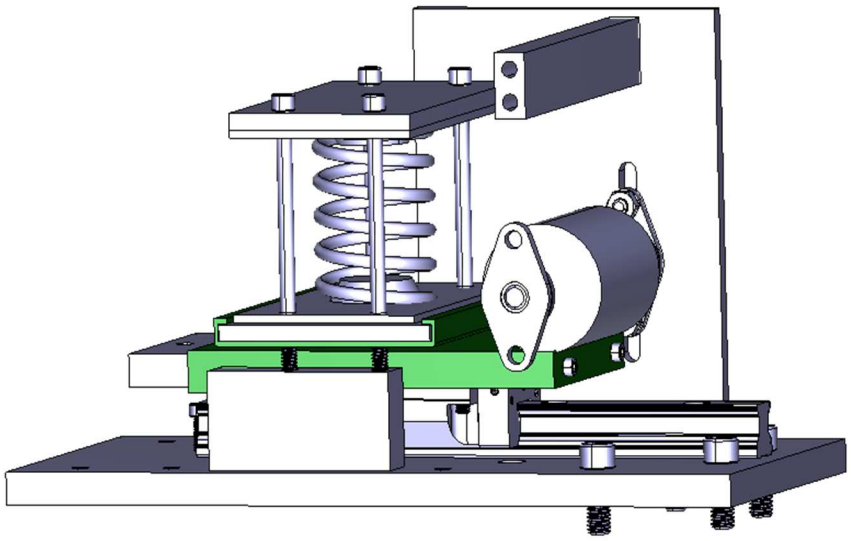

Figure 16: Inter-laminar Shear and Tack Testing Fixture

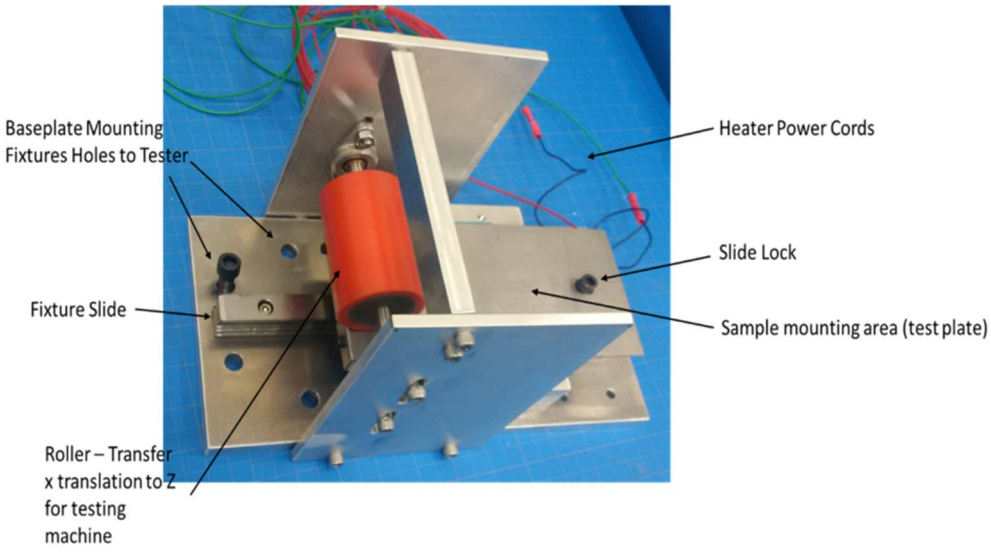

Figure 17: Inter-laminar Shear and Tack Testing Fixture Features

4.3.2.2 Tack Testing

Material specimens were cut from 0/90 oriented broad goods. The base plate material was cut to 150 mm x 127 mm and the test specimens were cut to 63.5 mm x 450 mm. The base plate material was centered on the base plate surface and edges folded onto the back, Figure 18A. The backing was then removed from the prepreg, and the sides were taped to the bottom of the base plate, Figure 18B. Additionally, the remaining edges were taped to the fixture when the backing was removed, as shown in Figure 18C. Taping the base plate material to the fixture enabled good contact of the specimen to the base plate and minimized potential debond during testing. The base was then placed on the slide over the heating pad and insulator, Figure 19A&B. The base was then attached with three screws indicated by red circles in Figure 19C. The screw length determined how the base plate will slide during tests, and, for the tack test, a shorter screw was used that would not prevent the base plate from translating on the slide.

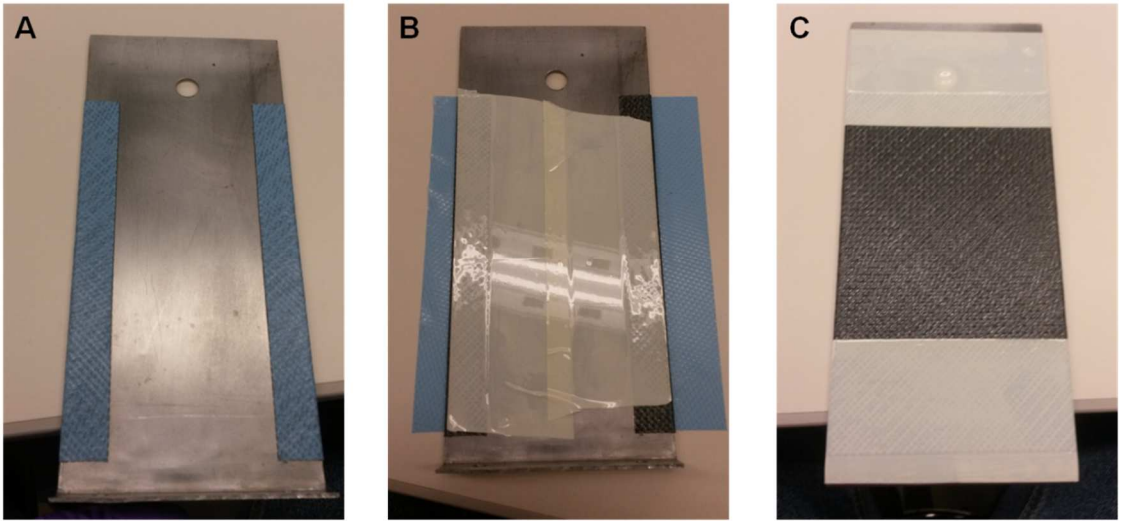

Figure 18: Base Plate Material Application

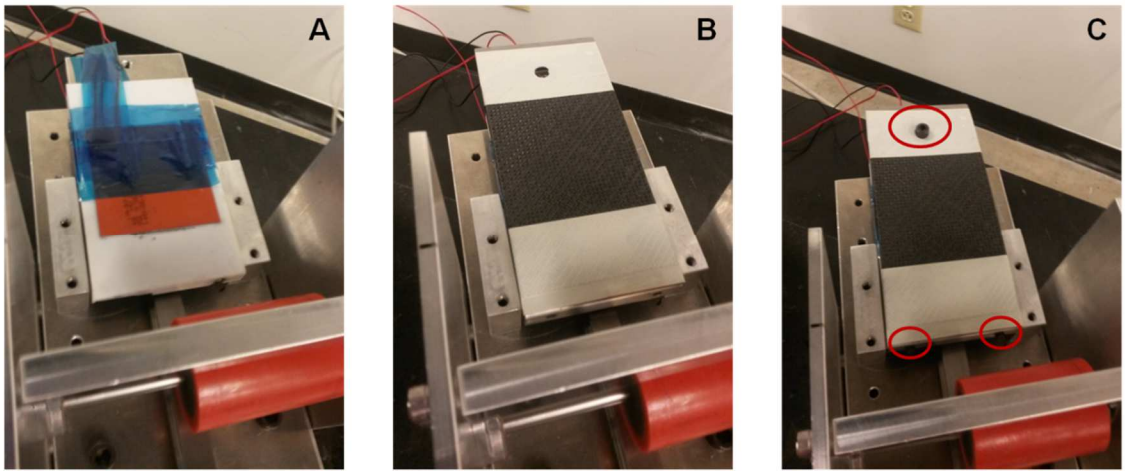

Figure 19: Base Plate Installation to Test Fixture

Then, 64 mm of backing material was removed from the test specimen which was placed centered on the base plate with the edge of sample backing aligned with the first tape edge, Figure 20. The samples were then heated to the desired test temperature and soaked at the test temperature for 15 minutes prior to testing. Room temperature tests were allowed to sit for a minimum of 3 minutes before testing. Samples were run under the roller, Figure 21A, and clamped in a pneumatic grip between two plates, Figure 21B, before testing was initiated.

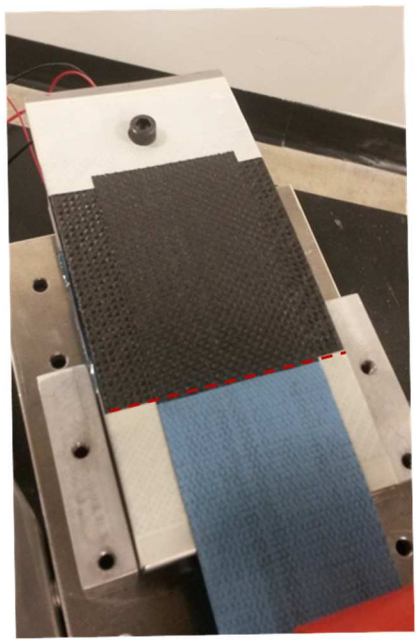

Figure 20: Sample Alignment on Base Plate

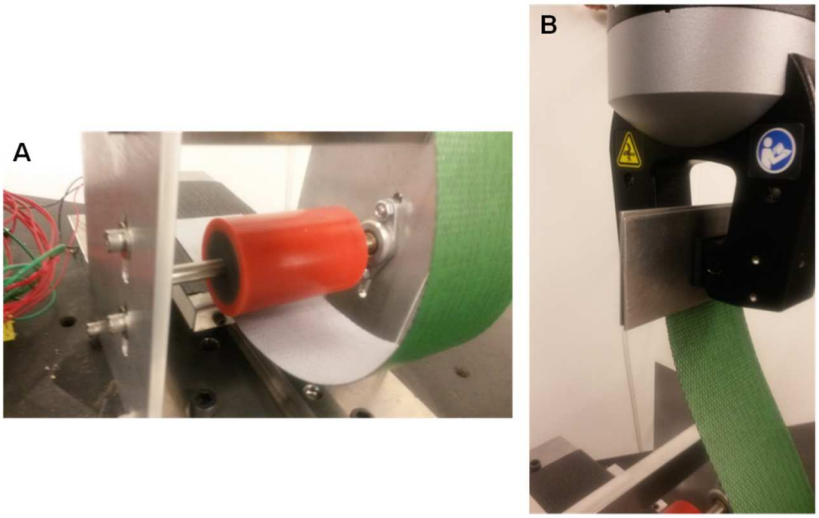

Figure 21: Sample Attachment

Tests were conducted at Washington University in St. Louis using an Instron Model 5583 with a load cell of 500 N. Tests were conducted by controlling the extension and set based upon the indicated displacement rate.

4.3.2.3 Inter-laminar Shear Testing

Test samples were cut from 0/90 broad goods to the desired fiber orientation. The test sample for all tests was cut to 63.5 mm x 450 mm oriented in the 0° direction. Base plate material was cut 150 mm x 127 mm while the pressure plate material was cut to 127 mm x 100 mm. The orientation of the base plate and pressure plate material varied based upon the test requirements. The orientation of each sample was cut such that the warp of the fiber weave was 0° for the 0/90 or +45 for the ±45 tests.

The application of the material to the base plate and attachment of the base plate to the fixture was the same as the tack tests presented in Figure 18 and Figure 19. A longer screw was used to lock the base plate to the slide to prevent slip during the inter-laminar shear tests. The pressure plate material was wrapped around the plate and secured in the same manner as the base plate material, as shown in Figure 22.

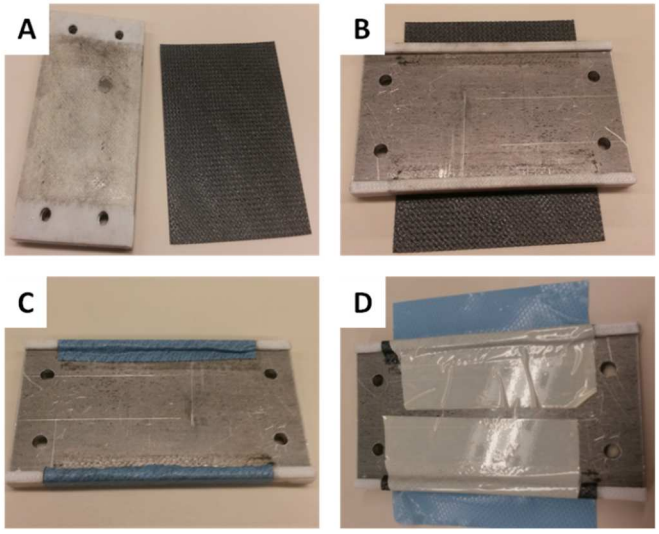

Figure 22: Pressure Plate Material Application

Then, 100 mm of the test sample's backing film was removed and attached to the base plate as shown in Figure 20. Once the test specimen was installed on the base plate, the pressure plate was placed on the base plate through alignment screws, Figure 23A&B. Then, the spring

and supporting structure were applied, Figure 23C&D. Pressure was set by compressing the spring to the height of the standoffs, Figure 23E&F.

Test samples were heated to the desired test temperature and allowed to soak for a minimum of 15 minutes before starting the test. To attach the sample to the pneumatic grip, the sample was wrapped around the grip plates, Figure 24A-C, to prevent the sample from pulling out of the grips.

Tests were conducted at Washington University in St. Louis using an Instron Model 5583 with a load cell of 500 N for testing temperature greater than 50 °C and an 5 KN load cell for testing temperatures less than or equal to 50 °C. Tests were conducted by controlling the extension and set based upon the indicated displacement rate.

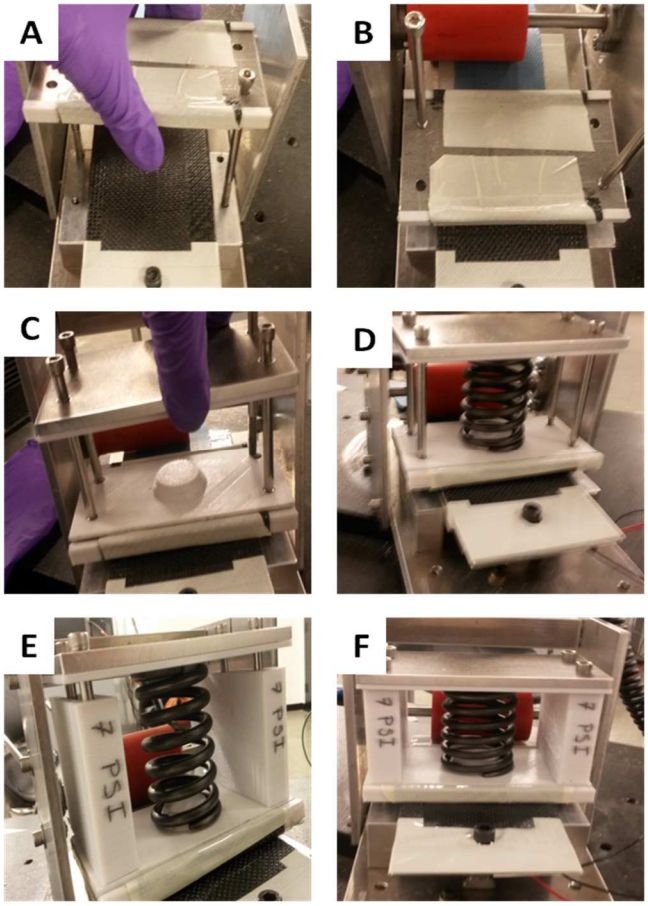

Figure 23: Pressure Assembly Attachment

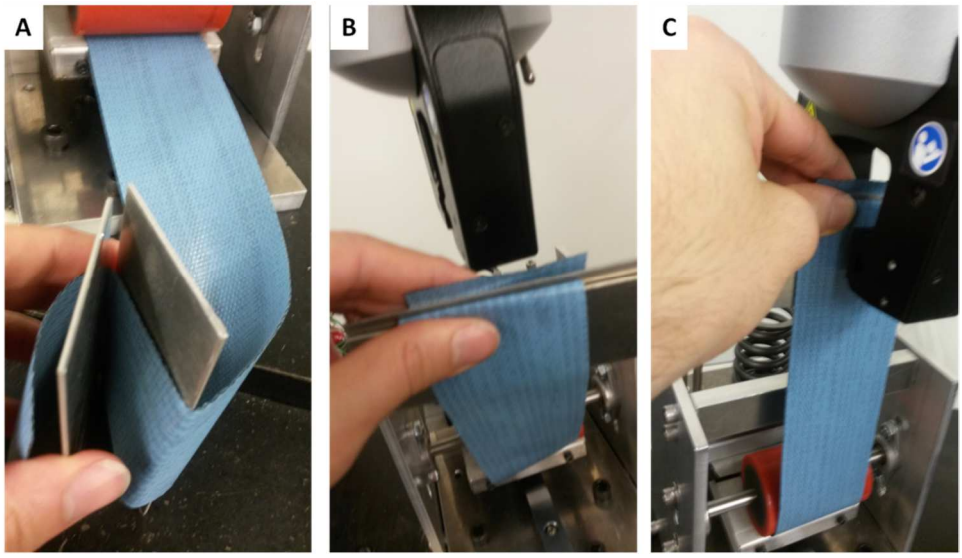

Figure 24: Inter-laminar Shear Grip Attachment

4.3.3 Hot Drape Forming

Hot drape forming tests were conducted on the tool outlined in Figure 25. This tool was chosen as it closely resembles the tool used by Hallander, et al. [1] incorporating a challenging joggle ratio. This specific tool increases the influence of the tool joggle by mirroring the joggle across the tool axis. This allows a comparison to the type of wrinkles observed by Hallander, et al. while further investigating the effect of a compound joggle and material weaves.

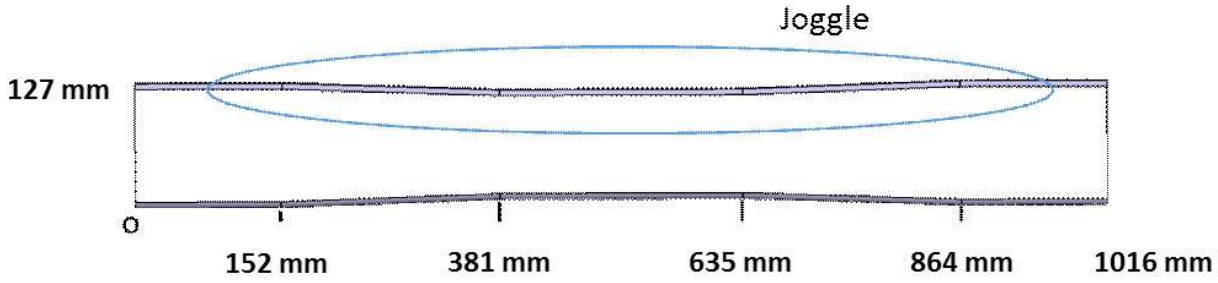

Figure 25: Hot Drape Forming C-Channel Tool (top view)

Further information regarding the tool joggles is presented in Table 7.

Table 7: Joggle Geometry

Flange Length	76.2 mm
Joggle Run	228.6 mm
Joggle Instep	7.62 mm

Flat laminates were hand laid up following the symmetric layups presented

Table 8, in which the plain weave layup 'n' designates the number of (45/0) sequences needed to meet the required ply count and k represents the total number prepreg layers.

$$n = \frac{k-2}{4} \tag{63}$$

Table 8: Composite Layups

Weave Type	**Composite Layup**
Unidirectional Tape	$[+45,0,-45,90,+45,0,-45,90,+45]_s$
Plain Weave	$[(\pm 45,0/90)_n,\pm 45]_s$
8 Harness	$[(\pm 45,0/90)_4,\pm 45]_s$

The individual plies were cut to 965 mm in length by 279 mm width. The plies were hand laid up using the layups presented in Table 8 with no external compaction. The flat laminate was transferred to the hot drape former on a tray to reduce sagging and was centered on the test tool. Three thermocouples were imbedded into the laminate 25 mm from the edge of the flange and located at 100 mm, 500 mm, and 915 mm along the tool. Of the three thermocouples placed, one was placed under the top ply, in the center of the laminate, and on the bottom ply.

The laminate was heated at a rate of 10 °C/min until reaching the set point temperature. The laminate was held at the set point temperature for 15 minutes or until the average thermocouple temperature reached the forming temperature, whichever was longer. Upon completion of the soak, the heating source was disconnected and vacuum was pulled a rate of 6.87 kPa/min to initiate forming. Formed spars were allowed to debulk under full vacuum for 5 minutes to return to room temperature before releasing vacuum and measuring green state wrinkles.

To quantitatively determine the effect of forming parameters on out-of-plane wrinkle development, post-formed out-of-plane green state wrinkles were characterized based upon: type (Figure 3), tool location, and size (Figure 26). The maximum height, wrinkle wavelength, and out-of-plane wrinkle depth were measured at the wrinkle root using a handheld digital micrometer with tolerance of ±0.05 mm. The wrinkle magnitude was represented as a ratio of wrinkle wavelength to wrinkle depth (L/D). A low L/D (i.e., L/D < 10) represents a large green state wrinkle, which when cured, will heavily influence mechanical properties. A large L/D (i.e., L/D > 100) was a minimal green state wrinkle which will be mitigated during cure. A sample with no wrinkle was considered to have an L/D of 150 accounting for the tolerance of the micrometer.

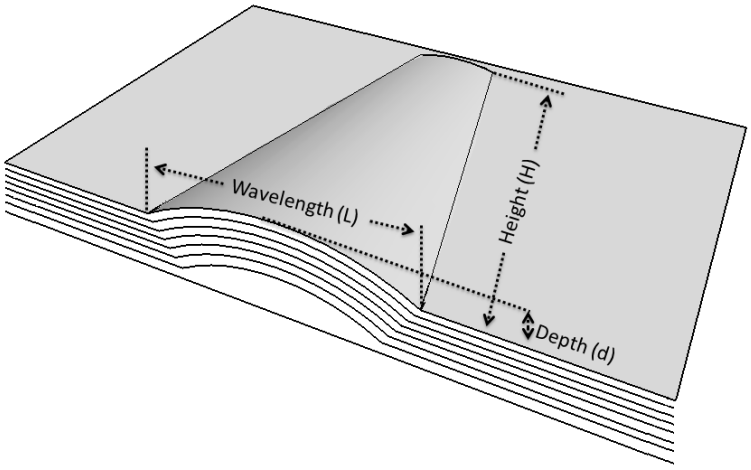

Figure 26: Wrinkle size measurements

CHAPTER 5 – RESULTS AND DISCUSSION

Chapter 5 discusses the results from the experiments outlined in Chapter 4. All sections address prepregs made with Cycom 970 except section 5.6.1 which considers Cycom 5320-1. Tests conducted with the Cycom 970 resin include intra-laminar shearing, inter-laminar shearing, and bias extension tests and address Hypotheses 1, 2, and 4 while the Cycom 5320-1 prepregs were utilized to address Hypothesis 3.

5.1 Resin Viscosity

The manufacturer's data sheet for Cycom 970 resin [110] only reports the resin viscosity from 50 °C to 175 °C. Thus the convergent viscosity modeling software was used to generate the full viscosity profile, shown in Figure 27. Between 22 °C and the local minimum of 130 °C, this data was best fit to a power equation shown in (64) which was used as the governing viscosity equation in later calculations.

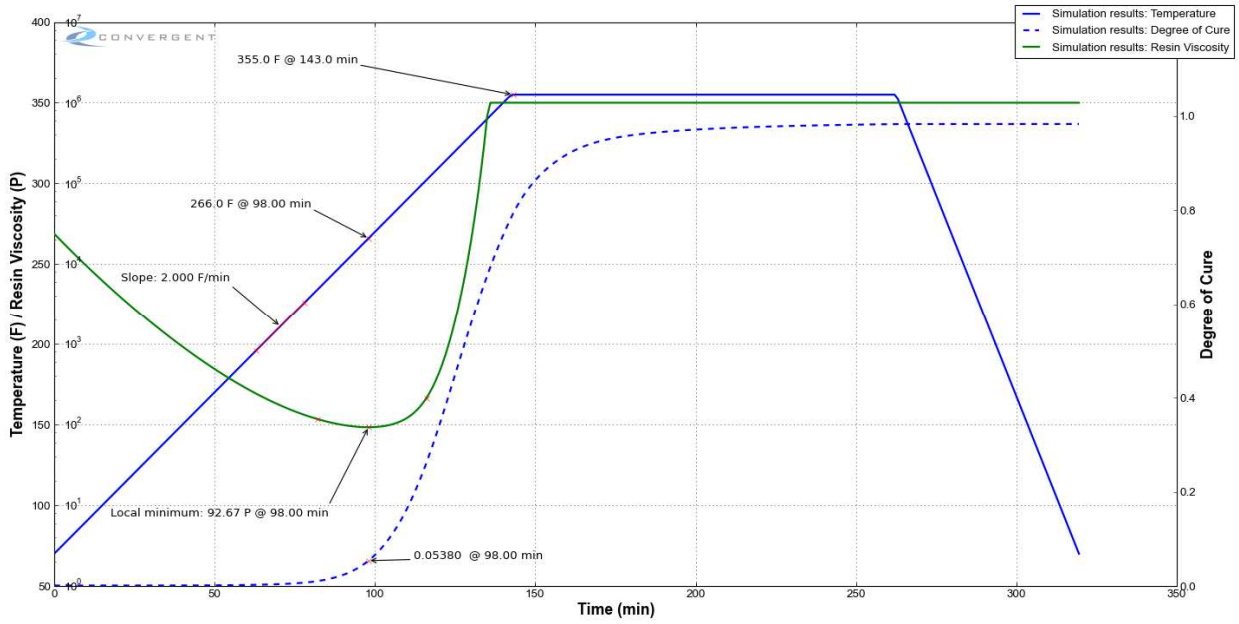

Figure 27: Convergent Cycom 970 Viscosity Profile

$$\eta = 5E8 * T^{-3.21},\ 22℃ < T < 130℃ \quad (64)$$

5.2 Resin Film Thickness

The resin layer thickness on a prepreg ply was measured for an individual ply and also a set of three plies compressed at 2, 24, and 48 kPa. It is assumed that the resin layer is the difference of the ply stack less the design thickness of the carbon prepreg. It is assumed that the resin interface layer accounts for the bulk factor of the prepreg and the natural variation of prepreg thickness.

Since the nominal thickness of the carbon fiber is known to be 0.0216 mm for Cycom 970 standard-twist and never-twist materials, the resin layer is assumed to be the same for both materials. Table 9 provides the results of the various resin layers that were during the inter-laminar shearing calculations.

Table 9: Resin Layers of Compressed Prepreg Stacks

Pressure (kPa)	Resin Layer (mm)
2.00	0.044
24.13	0.036
48.26	0.024

5.3 Bias Extension Tests

The unit cell for the bias extension tests was determined by measuring the tows in the warp and weft directions over a two-inch span and back calculating the unit cell. Five replicates were taken for tows per inch as outlined in Table 10.

Table 10: Tows per 25.4 mm in Warp and Weft directions

Warp	**Weft**
12.5	12.5
12.5	12.5
13	12.5
12.5	12.5
12.5	12.5

Assuming that the tow width is minimal, the unit cell dimensions are outlined in Figure 28. In the unit cell, the length and width are kept constant during the bias extension test while the internal angles distort leading to an extension of the diagonal measurement.

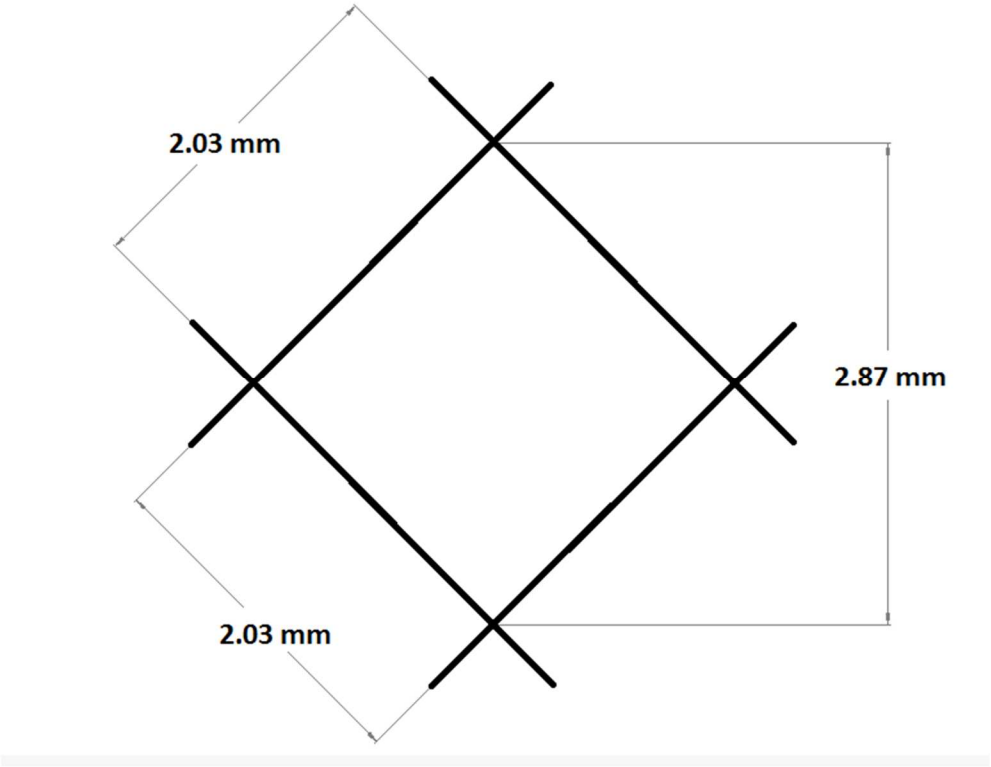

Figure 28: Unit Cell of 970 PW Materials

The bias extension tests are shown in Figure 29. The load versus extension follows the typical two stages of the bias extension test. The first stage is in-plane fiber rotation due to the extension of the fiber unit cell (Figure 28). The second stage is out-of-plane fiber rotation. This occurs after the fibers have rotated and reached the locking angle causing further distortion to go out-of-plane. Thus the intersection of the two regions is the transition from the in-plane rotation to out-of-plane rotation.

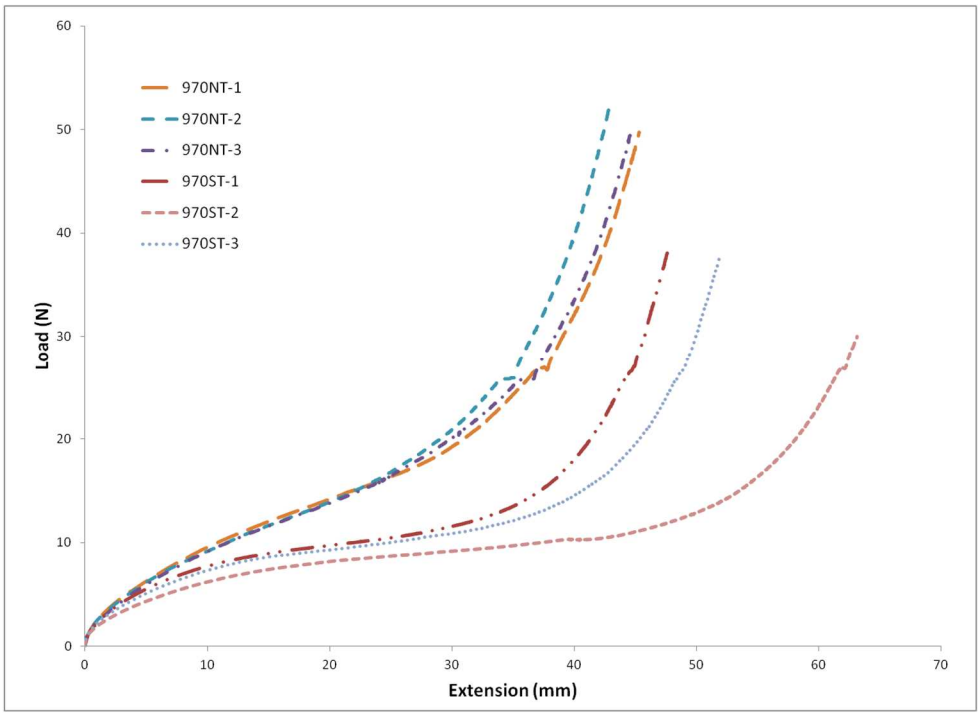

Figure 29 – Bias Extension Tests

* The 970ST-2 sample had a grip length of 7.5 inches instead of the typical 6 in grip increasing the extension of the test.

The extension at which this occurs is used to calculate the locking angle by adding the extension/unit cell to the hypotenuse of the unit cell. Assuming then that the edges of the unit cell do not distort and only the angles move, the locking angle of the fabric can be calculated. Table 11 summarizes the locking angles from the test specimens.

Table 11: Calculated Locking Angles

Sample	Locking Angle (degree)
970ST_1	27.56
970ST_2	26.49
970ST_3	24.82
970NT_1	28.96
970NT_2	29.16
970NT_3	28.10

In order to determine if the two material twists are equivalent, a paired student-t test was conducted. The test showed that the standard-twist and never-twisted samples have equivalent

locking angles at a 95% confidence. Thus the effect of intra-laminar shearing was assumed to be negligible during the forming of the standard-twisted and never-twisted material forms.

5.4 Tack Tests

Section 5.4 and its subsections pertain to Hypothesis 1. It states that the material tack grade does not affect the inter-laminar friction at temperatures above room temperature and that out-of-plane wrinkling is not affected by the tack level.

5.4.1 Tack Test Results

Tack tests were conducted as outlined in section 4.3.2.2. The maximum tack values from the tests are reported in Table 12. Several additional test points were added to better observe the trends that were observed in the high tack testing.

The averaged tack data is summarized in Table 13 and Figure 30. It is observed that the high tack and low tack samples possess very similar adhesive force. In several instances, the low tack sample has a higher adhesive force than the high tack sample tested under the same conditions. The different grades of tack are shown to be statistically equivalent though an ANOVA regression discussed in section 5.4.2. Additionally, the averaged data clearly shows that the tack increases until a local maximum at 38 °C and then decreases as temperature increases. The local maximum of tack has been observed in tack tests of automated tape laying prepregs [76].

Table 12: Tack Test Data

	Low Tack (N)			High Tack (N)		
Temperature (°C)	**0.84 mm/s**	**0.42 mm/s**	**0.21 mm/s**	**0.84 mm/s**	**0.42 mm/s**	**0.21 mm/s**
22.2	43.3	43.1	49.7	52.62	40.4	45.4
22.2	41.1	40.6	34.9	44.5	-	-
22.2	47.3	42.1	-	-	-	-
37.8	54.4	46.2	48.3	66.6	44.9	-
37.8	53.4	49	46.7	43.3	-	-
48.9	46.1	33.4	31.6	38	35.4	24
48.9	32.7	30.6	-	-	31	-
48.9	-	40.3	-	-	27.7	-
60	35.1	26	24	27.2	-	19.4
60	24.5	28.2	-	-	-	-
71.1	24.7	20.7	19.2	17.6	16.2	17.5
71.1	23.2	18.9	13.9	18.1	-	-
71.1	29.1	-	-	19.3	-	-

Table 13: Averaged Tack Data

	Low Tack (N)			High Tack (N)		
Temperature (°C)	**0.84 mm/s**	**0.42 mm/s**	**0.21 mm/s**	**0.84 mm/s**	**0.42 mm/s**	**0.21 mm/s**
22.2	43.9±3.1	41.9±1.2	42.3±10.5	48.6±5.7	40.4	45.4
37.8	53.9±0.7	47.6±2.0	47.5±1.1	55.0±16.5	44.9	-
48.9	39.4±9.5	34.8±5.0	31.6	38.0	31.4±3.9	24.0
60	29.8±7.5	27.1±1.6	24.0	27.2	-	19.4
71.1	25.7±3.1	19.8±1.3	16.6±3.7	18.3±0.9	16.2	17.5

Tack between plies acts similarly to a pressure-sensitive adhesive. Pressure-sensitive adhesives have two typical failure modes defined by the Dahlquist criteria [111–113]: interfacial and cohesive failure modes. The Dahlquist criteria states that there exists a value of the elastic modulus under which the adhesive starts to flow and above it the adhesive is too stiff to fully wet the substrate, which causes interfacial failure between the resin and substrate. Below the critical modulus, the adhesive is able to fully wet the substrate causing cohesive failures.

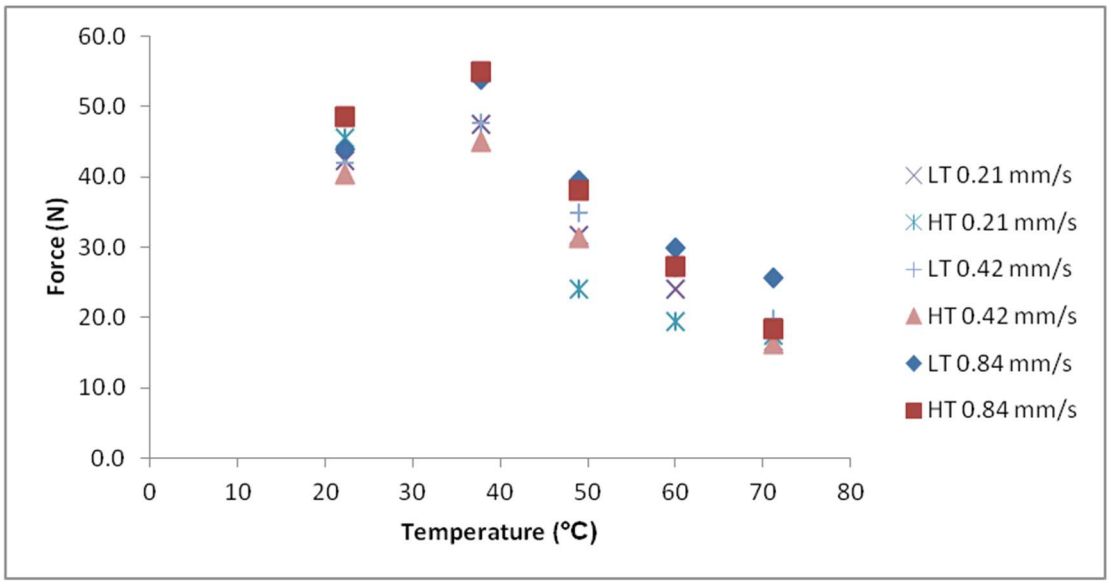

Figure 30: Averaged Tack Tests

Different prepreg tack levels can exhibit both inter-facial and cohesive failure modes [76]. Interfacial failures occur on typical automated prepregs (lower tack specimens) where the tack increases with increasing temperature as it is able to wet the surface better. Higher tack specimens show a cohesive failure in which the tack force decreases with increasing temperature as the adhesive bonds weaken with increased heat. Prepregs that exhibit a peak tack value exhibit both types of falures due to meeting the Dahlquist criteria within the screened temperature range. Lower temperatures will have a stiffer modulus and exhibit interfacial failures while at higher temperatures will show cohesive failures as the modulus is less than the critiera. The 970 tack tests for both the high-tack and low-tack varients show both failure modes which is clearly seen by the local maximum in Figure 30. Additionally, in Figure 31 and Figure 32, the amount of wetting of the high-tack samples is observed to correspond to inter-facial failures and cohesive failures. For inter-facial failures, most of the tack failure occurs at the surface causing small adhesive strings to form between plies. During cohesive failures, the resin flows and more adhesive strings form between plies.

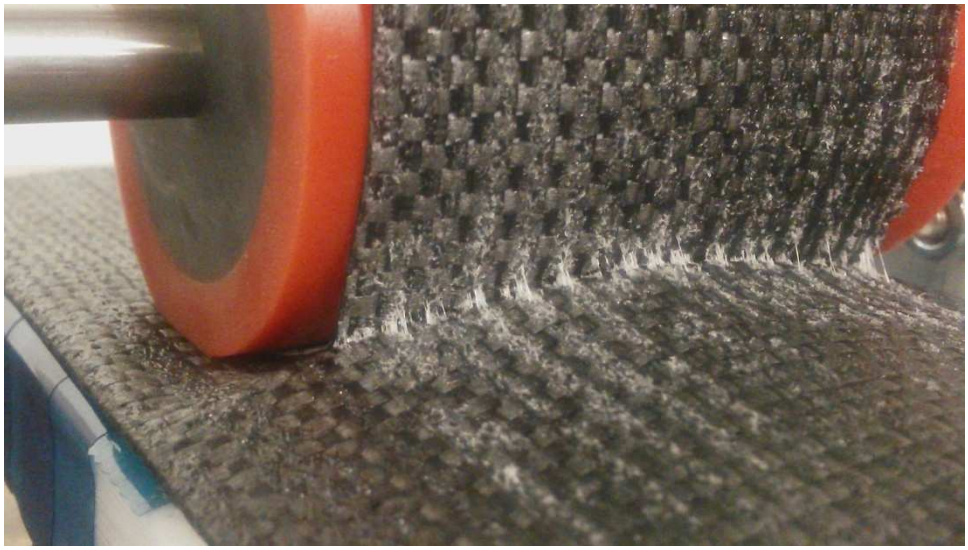

Figure 31: HTST Tack Test 22 °C – Inter-facial Failure

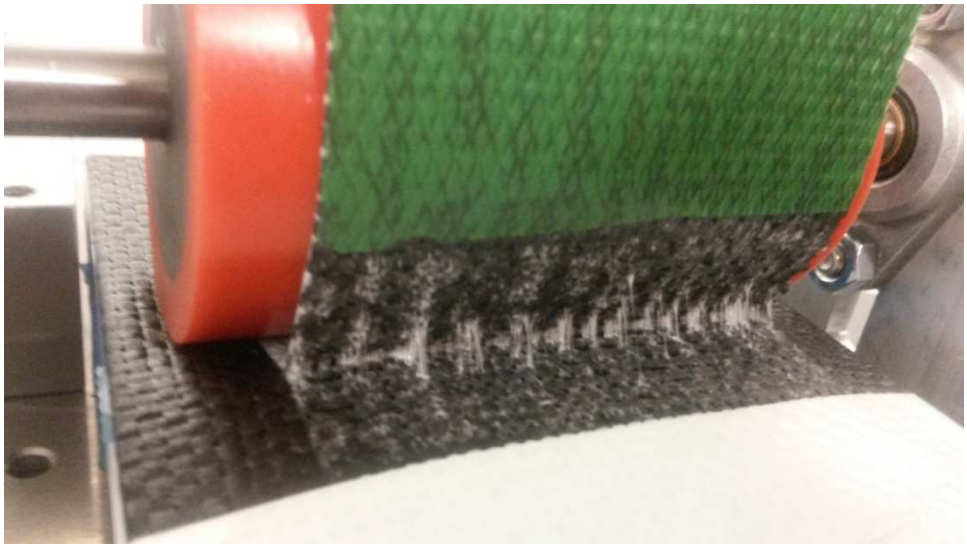

Figure 32: HTST Tack Test 49 °C – Cohesive Failure

5.4.2 Tack Models

An ANOVA regression was performed on the tack data in Table 12 looking at the temperature, extension rate, and tack level as variables. With a 5% significance interval, the significant variables are identified as the temperature and extension rate as shown in Table 14.

The material tack levels were found to be statistically equivalent at each test temperature. While all tests were performed within the manufacturer's working life of 10 days, the out time was not recorded for the samples. It is possible that the high tack samples possessed more out time than the low tack samples which may have affected the tack test results.

Table 14: Significant Tack Variables

Variable	P-value
Temperature (°C)	0
Rate (mm/s)	0.003
Material	0.202

A second order model is able to accurately capture the cohesive failures (>40 °C) but does not accurately predict the peak tack force centered around 38 °C as observed in Figure 30. In order to fully capture the transition from interfacial to cohesive failure transition, a cubic model was fitted to the data. This model is provided by Equation 65 with an R-squared of 0.926, it shows no statistically significant differences between tack levels. In Equation 65, T is the test temperature in Celsius and $\dot{x}$ is the extension rate in mm/s.

$$T(N) = -30.790 + 6.923\mathrm{T} - 83.470\dot{x} - 0.175T^2 + 2.439T\dot{x} + 61.1\dot{x}^2 + 0.001\mathrm{T}^3 - 0.013\mathrm{T}^2\dot{x} - 1.047T\dot{x}^2 \quad (65)$$

In Figure 33 through Figure 35, the tack model (65) is plotted at each extension rate with the averaged experimental high tack and low tack results overlaid. The maximum tack values are at 30 °C for 0.21 mm/s extension rate, 31 °C for the 0.42 mm/s rate, and 32 °C for the 0.84 mm/s rates. The subtle difference in the transition temperature from interfacial to cohesive failure modes indicates that the viscoelastic nature of the resin also influences the tack response.

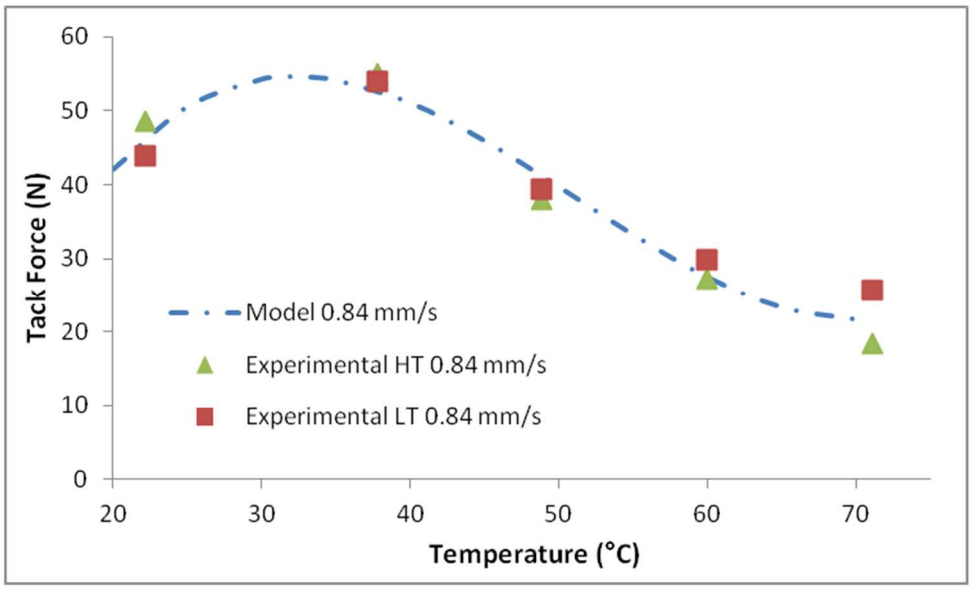

Figure 33: 0.84 mm/s Tack Model

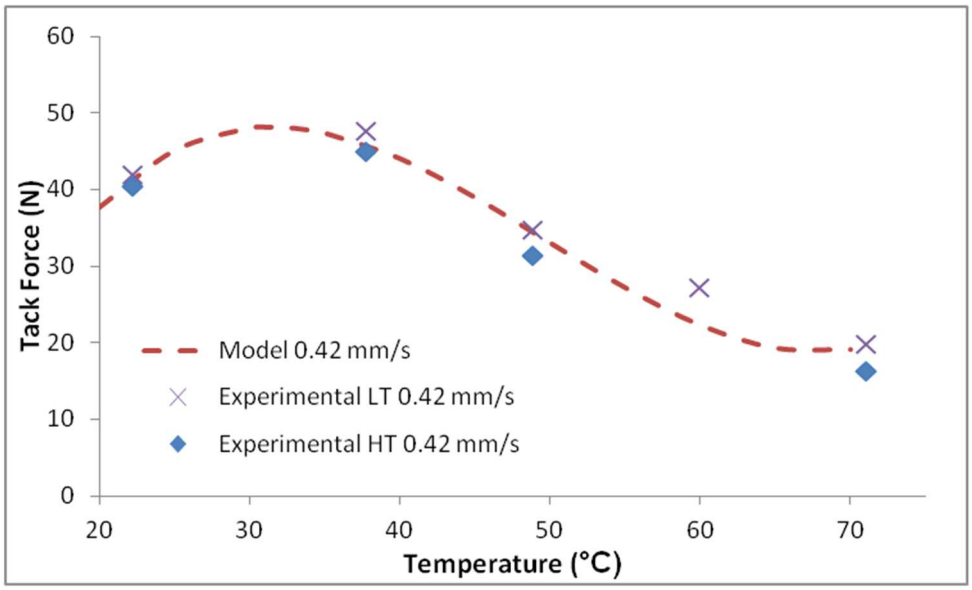

Figure 34: 0.42 mm/s Tack Model

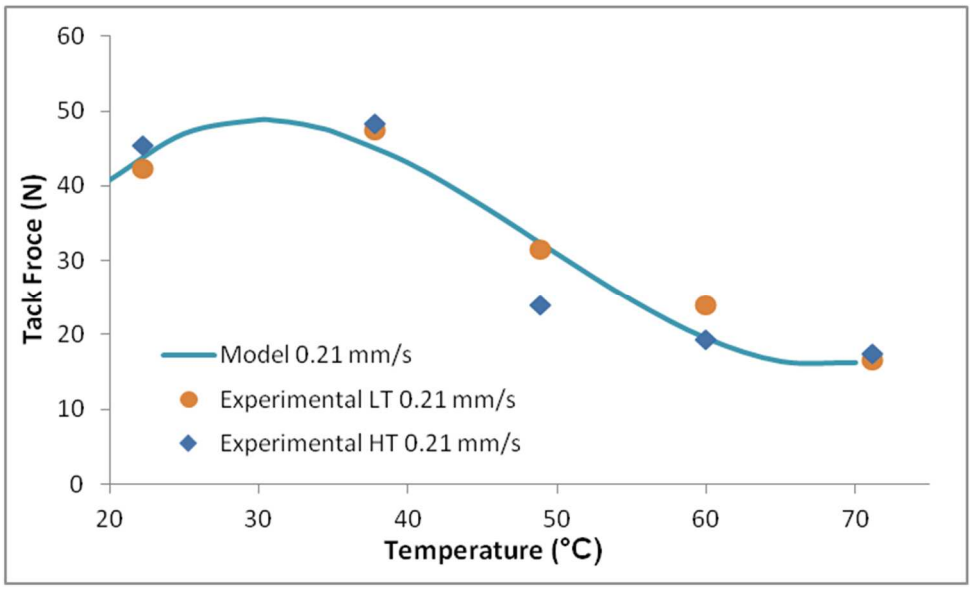

Figure 35: 0.21 mm/s Tack Model

5.4.3 Discussion of the Influence of Tack on Drape Forming and Automated Processes

The tack test data shows that there is not a significant difference between the two tack types at elevated temperatures. What the tack test can clearly show however is the failure mode of the resin. Positive slopes to a tack curve indicate that the failure mode is interfacial while negative slopes indicate cohesive failures.

For multiple composite plies forming in one operation, the plies are required to slip past each other. The failure mode of tack failure would affect how the plies slip. For instance, meeting the Dahlquist criteria would enable the resin to begin to flow and lubricate the interface between plies acting more similarly to Couette flow. Thus, a negative slope of the tack versus temperature curve would indicate that the Dahlquist criteria had been met for the resin system and that the resin lubricates the inter-laminar slip. A positive slope for the tack versus temperature curve would indicate the resin does not lubricate the ply interface.

The tack test can be used to identify the maximum tack value which is a useful process parameter for automated composite processes. For hot drape forming, the temperature corresponding to the maximum tack value represents the minimum forming temperature allowing the resin to flow. For Cycom 970 systems, the minimum temperature is between 30 °C and 32 °C. However, tape laying and automated fiber placement processes should process at the maximum tack value as these processes require the tack to adhere the new ply to the previous and to the tool.

Hypothesis 1 can be accepted since the two different tack grades of low tack and high tack were statistically equivalent above room temperature. The tack test itself however can show how the resin behaves at various temperatures and can show the minimum forming temperatures necessary to achieve a hydrodynamic slip state.

5.5 Inter-laminar Shear Tests

Section 5.5 and its subsections report the results of testing the first part of Hypothesis 2 which states that fiber twist plays a major factor on inter-laminar shearing. The second part of Hypothesis 2 is addressed in section 5.6.2.1 which pertains to the formation of wrinkles in c-channel parts produced with different fiber twist types.

Inter-laminar shear tests were conducted as outlined in section 4.3.2.3. The typical responses of the shear stress versus shear strain of the various extension rates tested are shown in Figure 36. In the initial phase of the test no permanent deformation occurs, the response is linear leading to the maximum stress defined as the static shear stress. As the static stress is overcome, the stress drops and equilibrates at the dynamic shear stress. Interestingly, this response is not quite as similar to those reported by Erland [81] but follow well with those reported by Haanappel [52]. Erland reported an increase in shear stress as the static load transitions to

dynamic. These tests were performed with much higher pressures than those tested herein due to the desire to better understand the compaction process which is more closely mimicked by the high rate/ high pressure test experiments conducted. The higher testing pressure can lead to the static stress and dynamic stress being equivalent which was confirmed at the upper bound of this test matrix.

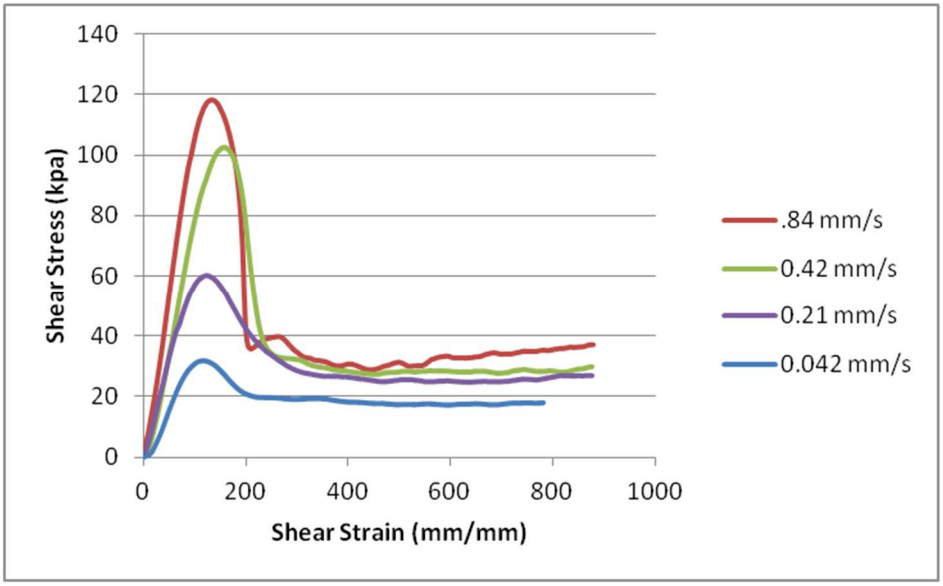

Figure 36: Typical Shear Response for Inter-Laminar Shear Tests (P=0 kPa)

From the experimental tests, the static and dynamic coefficient of frictions can further be determined through (66), where τ is the dynamic or static shear, μ_f is the coefficient of friction, and p is the normal pressure.

$$\tau = \mu_f p \tag{66}$$

5.5.1 Inter-Laminar Shear Experimental Results

The shear modulus, dynamic shear stress, static shear stress, static friction, and dynamic friction were calculated from the experimental tests and provided in Table 15 and Table 16.

Table 15: Never-Twisted Inter-Laminar Shear Stress Results

Temperature (°C)	Viscosity (Pa-s)	Extension Rate (mm/s)	Pressure (kPa)	Static Shear Stress (kPa)	Dynamic Shear Stress (kPa)	Shear Modulus (kPa)	Static Friction (μ_s)	Dynamic Friction (μ_k)
22.2	2514.97	0.04	2.00	47.14	33.66	0.32	23.57	16.83
71.1	59.05	0.04	2.00	5.12	2.45	0.09	2.56	1.23
22.2	2514.97	0.21	2.00	84.35	45.87	0.58	42.17	22.93
22.2	2514.97	0.21	2.00	101.15	39.03	0.71	50.57	19.51
48.9	370.83	0.21	2.00	31.91	15.07	0.30	15.95	7.53
71.1	59.05	0.21	2.00	14.13	6.15	0.20	7.07	3.08
71.1	59.05	0.21	2.00	16.35	7.00	0.23	8.17	3.50
22.2	2514.97	0.42	2.00	119.02	63.97	0.76	59.51	31.98
22.2	2514.97	0.85	2.00	103.96	28.42	0.84	51.98	14.21
22.2	2514.97	0.85	2.00	137.25	72.92	0.95	68.62	36.46
48.9	370.83	0.85	2.00	81.14	27.71	0.65	40.57	13.86
71.1	59.05	0.85	2.00	41.90	14.77	0.45	20.95	7.38
48.9	370.83	0.42	24.13	74.68	54.48	0.44	3.09	2.26
48.9	370.83	0.42	24.13	90.68	81.33	0.56	3.76	3.37
48.9	370.83	0.42	24.13	79.18	69.27	0.50	3.28	2.87
71.1	59.05	0.42	24.13	44.12	29.43	0.41	1.83	1.22
71.1	59.05	0.85	24.13	62.76	40.58	0.50	2.60	1.68
48.9	370.83	0.04	48.26	30.04	17.90	0.14	0.62	0.37
71.1	59.05	0.04	48.26	12.00	8.38	0.12	0.25	0.17
48.9	370.83	0.21	48.26	51.41	42.58	0.24	1.07	0.88
71.1	59.05	0.42	48.26	36.31	22.20	0.20	0.75	0.46
48.9	370.83	0.85	48.26	141.94	120.81	0.52	2.94	2.50
71.1	59.05	0.85	48.26	56.36	30.76	0.27	1.17	0.64
71.1	59.05	0.85	48.26	58.12	40.24	0.33	1.20	0.83
22.2	2514.97	0.04	2.00	48.82	25.61	0.35	24.41	12.80
22.2	2514.97	0.04	2.00	54.40	23.16	0.43	27.20	11.58
22.2	2514.97	0.04	2.00	41.85	28.67	0.37	20.93	14.33
48.9	370.83	0.04	2.00	8.94	5.71	0.11	4.47	2.85
71.1	59.05	0.04	2.00	4.98	2.42	0.07	2.49	1.21
22.2	2514.97	0.21	2.00	90.13	42.67	0.65	45.07	21.33
22.2	2514.97	0.42	2.00	133.15	28.44	0.92	66.57	14.22
48.9	370.83	0.21	2.00	31.89	12.16	0.30	15.94	6.08
22.2	2514.97	0.85	2.00	143.98	63.71	0.96	71.99	31.85
22.2	2514.97	0.85	2.00	138.84	40.39	1.00	69.42	20.19
22.2	2514.97	0.42	2.00	102.73	47.85	0.84	51.36	23.93
48.9	370.83	0.85	2.00	83.43	24.66	0.62	41.72	12.33
71.1	59.05	0.85	2.00	39.44	12.69	0.42	19.72	6.34

71.1	59.05	0.85	2.00	36.41	12.95	0.38	18.20	6.48
71.1	59.05	0.04	24.13	12.39	8.16	0.23	0.51	0.34
71.1	59.05	0.21	24.13	40.71	22.12	0.39	1.69	0.92
48.9	370.83	0.42	24.13	86.75	60.78	0.53	3.59	2.52
48.9	370.83	0.42	24.13	77.27	59.49	0.47	3.20	2.47
71.1	59.05	0.42	24.13	39.69	22.75	0.43	1.64	0.94
48.9	370.83	0.21	48.26	58.08	32.70	0.27	1.20	0.68
71.1	59.05	0.21	48.26	23.61	13.39	0.19	0.49	0.28
71.1	59.05	0.85	48.26	61.20	33.56	0.30	1.27	0.70
71.1	59.05	0.85	48.26	56.63	36.30	0.37	1.17	0.75

Table 16: Standard-Twist Inter-Laminar Shear Stress Results

Temperature (°C)	**Viscosity (Pa-s)**	**Extension Rate (mm/s)**	**Pressure (kPa)**	**Static Shear Stress (kPa)**	**Dynamic Shear Stress (kPa)**	**Shear Modulus (kPa)**	**Static Friction (μ_s)**	**Dynamic Friction (μ_k)**
22.2	2514.97	0.21	2.00	67.47	23.41	0.49	33.74	11.70
22.2	2514.97	0.21	2.00	56.23	21.51	0.50	28.11	10.75
22.2	2514.97	0.42	2.00	75.72	29.93	0.45	37.86	14.96
22.2	2514.97	0.85	2.00	113.62	45.44	0.92	56.81	22.72
22.2	2514.97	0.85	2.00	98.81	43.88	0.86	49.41	21.94
37.8	931.60	0.42	2.00	46.80	18.52	0.44	23.40	9.26
37.8	931.60	0.85	24.13	149.32	140.91	0.87	6.19	5.84
37.8	931.60	0.42	48.26	105.05	97.30	0.50	2.18	2.02
48.9	370.83	0.21	2.00	27.97	8.03	0.33	13.99	4.02
48.9	370.83	0.85	2.00	54.05	19.09	0.66	27.02	9.55
48.9	370.83	0.42	24.13	74.60	49.65	0.66	3.09	2.06
48.9	370.83	0.42	24.13	83.63	60.44	0.65	3.47	2.50
48.9	370.83	0.42	24.13	66.15	53.26	0.52	2.74	2.21
48.9	370.83	0.85	48.26	121.02	94.88	0.43	2.51	1.97
60	101.23	0.42	2.00	25.74	12.01	0.36	12.87	6.00
60	101.23	0.85	24.13	83.90	60.29	0.67	3.48	2.50
60	101.23	0.42	48.26	51.57	33.53	0.30	1.07	0.69
71.1	59.05	0.21	2.00	8.40	3.04	0.24	4.20	1.52
71.1	59.05	0.21	2.00	10.24	3.20	0.22	5.12	1.60
71.1	59.05	0.85	2.00	16.75	4.76	0.28	8.37	2.38
71.1	59.05	0.42	24.13	34.44	26.79	0.42	1.43	1.11
71.1	59.05	0.85	48.26	51.11	28.08	0.37	1.06	0.58
71.1	59.05	0.85	48.26	51.88	33.06	0.40	1.07	0.68
71.1	59.05	0.85	48.26	51.08	35.01	0.32	1.06	0.73
22.2	2514.97	0.85	2.00	118.33	33.60	1.10	59.16	16.80
22.2	2514.97	0.04	2.00	31.64	19.16	0.32	15.82	9.58

22.2	2514.97	0.21	2.00	60.07	25.43	0.61	30.03	12.72
22.2	2514.97	0.42	2.00	102.66	28.25	1.31	51.33	14.13
22.2	2514.97	0.04	2.00	31.05	12.25	0.45	15.53	6.13
22.2	2514.97	0.85	2.00	88.22	20.70	0.85	44.11	10.35
22.2	2514.97	0.42	2.00	95.64	19.86	0.92	47.82	9.93
48.9	931.60	0.21	48.26	63.72	43.03	0.36	1.32	0.89
48.9	931.60	0.42	24.13	92.86	61.81	0.63	3.85	2.56
48.9	931.60	0.42	24.13	61.14	54.03	0.54	2.53	2.24
48.9	931.60	0.85	2.00	46.05	10.79	0.56	23.03	5.40
48.9	931.60	0.21	2.00	14.34	4.89	0.28	7.17	2.44
48.9	931.60	0.04	2.00	2.75	1.79	0.07	1.38	0.89
71.1	59.05	0.04	2.00	3.51	0.67	0.16	1.76	0.34
71.1	59.05	0.04	24.13	17.07	11.09	0.31	0.71	0.46
71.1	59.05	0.85	2.00	13.04	4.30	0.32	6.52	2.15
71.1	59.05	0.42	24.13	36.34	20.16	0.51	1.51	0.84
71.1	59.05	0.85	48.26	51.63	30.66	0.38	1.07	0.64
71.1	59.05	0.21	48.26	33.77	21.18	0.25	0.70	0.44
71.1	59.05	0.85	48.26	53.01	31.55	0.38	1.10	0.65

The stress versus strain response of the 22.2 °C tests for both fiber twist types gives an indication of the type of response sliding materials exhibit. The shear rate was calculated from the Couette flow equation (32). As indicated in Figure 37 and Figure 38, the behavior of the inter-laminar shear stress approximates that of a Bingham plastic where the response is linear after an initial shear stress is reached as indicated by Equation 21.

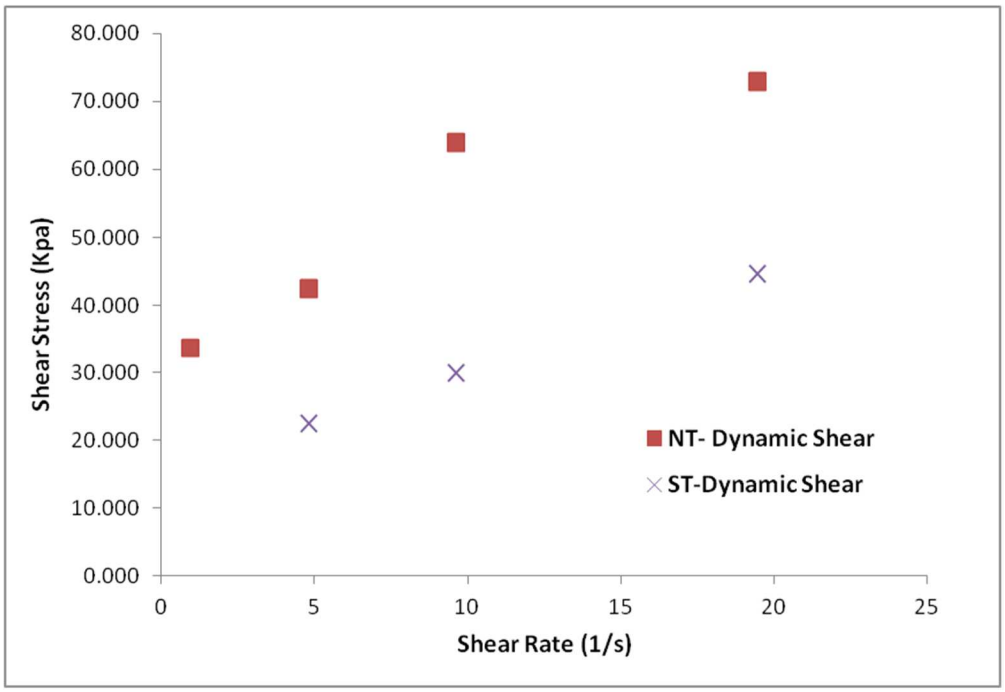

Figure 37: Bingham Plastic Response of Dynamic Shear Stress at 22.2 °C

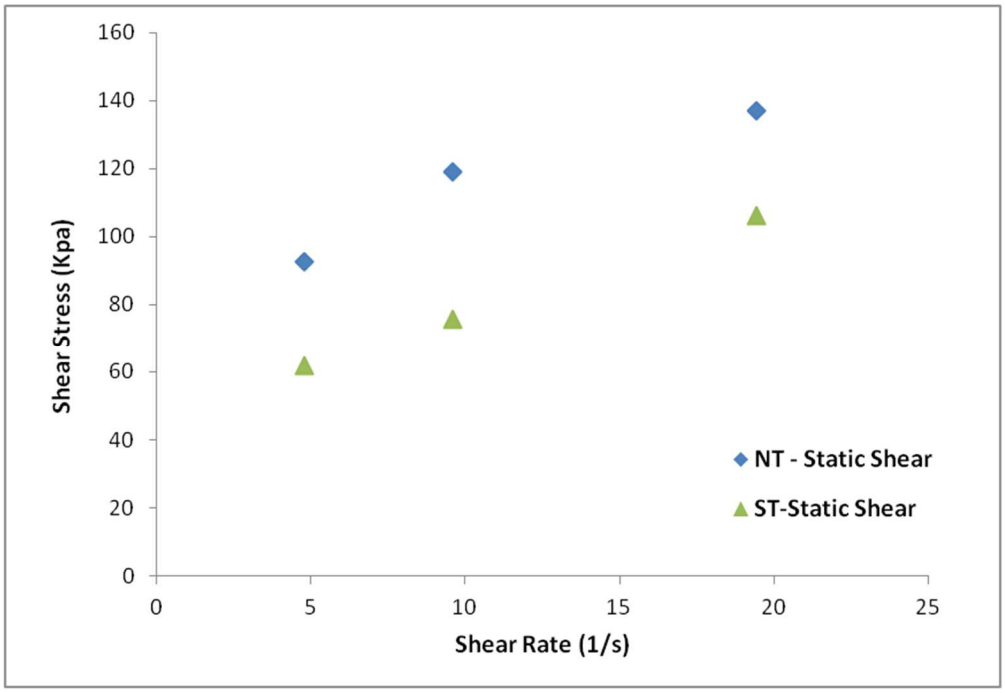

Figure 38: Bingham Plastic Response of Static Shear Stress at 22.2 °C

5.5.1.1 Inter-Laminar Shear Regression Model

Additional temperature responses were not plotted due to an insufficient variation of tests at different shear rates. The data was fit using a surface regression model in Minitab statistical software, and this model was used as the basis for interpolation. The full quadratic model considered variables of pressure, viscosity, and shear rate. In Table 17, X denotes a significant variable at significance levels of 5% and provides the R^2 values of the model.

Table 17: Significant Variables for Inter-Laminar Shear Tests

Variable	Static Shear	Dynamic Shear	Shear Modulus
Viscosity	X	X	X
Rate	X	X	X
Pressure	X	X	-
Fiber Twist	X	X	-
Orientation	-	X	X
R-sq	87.5	81.0	85.7

For the static shear case, all variables except the orientation were significant. As indicated in the fundamental shear equations (19-21), the shear rate and viscosity were expected to play a fundamental role. Pressure also affects how the material will begin to shear. It is interesting that the standard twist and never twisted fibers affect the static shearing while the ply orientation does not. In the dynamic shear model, the ply orientation is significant which indicates that there is a difference of friction between the two orientations but that in the static region there are more dominating variables. The shear modulus only had three significant variables: viscosity, shear rate, and ply angle. The viscosity and shear rate are as expected, but the pressure is not significant in the quadratic surface regression model. Additionally, the ply orientation does show significance which would indicate a difference of friction between similar and off-angle slips. The fit equations for the static shear, dynamic shear, and shear modulus take

the general form of Equation 67 where the constants are provided in Table 18. Where p is the applied pressure (kPa), $\dot{\gamma}$ is the shear rate (1/s), and μ is the resin viscosity (kPa·s).

$$\tau, G = C_0 + C_1\mu + C_2\dot{\gamma} + C_3p + C_4\mu^2 + C_5\dot{\gamma}^2 + C_6p^2 + C_7\mu\dot{\gamma} + C_8\mu p + C_9\dot{\gamma}p \quad (67)$$

Table 18: Inter-laminar Shear Model Constants

	Material	C0	C1	C2	C3	C4	C5	C6	C7	C8	C9
Static Shear	ST_0	-1.900	28.670	1.194	0.990	-6.000	-0.045	-0.005	1.516	-0.110	0.017
	ST_45	9.100	5.200	-0.660	0.740	-5.020	-0.043	-0.024	3.778	0.024	0.108
	NT_0	1.570	24.490	2.173	0.590	-3.350	-0.030	-0.014	1.484	-0.026	0.018
	NT-45	-9.500	29.370	2.921	0.568	-4.790	-0.056	-0.015	2.082	0.040	0.041
Dynamic Shear	ST_0	-3.390	14.880	0.454	0.896	-5.200	-0.040	-0.009	1.049	0.305	0.028
	ST-45	-16.990	10.170	1.307	1.053	-4.640	-0.058	-0.020	1.770	0.380	0.071
	NT_0	5.390	9.200	0.389	0.593	-2.550	-0.048	-0.021	1.434	0.233	0.064
	NT-45	-8.500	13.850	1.301	0.596	-4.640	-0.058	-0.020	1.770	0.380	0.071
Shear Modulus	ST_0	0.078	0.156	0.020	0.007	-0.026	0.000	0.000	0.004	-0.002	0.000
	ST-45	-0.055	0.163	0.031	0.008	-0.011	0.000	0.000	0.008	-0.002	0.000
	NT_0	0.077	0.143	0.023	0.002	-0.009	0.000	0.000	0.003	-0.002	0.000
	NT-45	-0.001	0.151	0.027	0.005	-0.011	0.000	0.000	0.008	-0.002	0.000

Table 19: Model Data for Never Twist Material and Ply Angle 0°

Temperature (°C)	Extension Rate (mm/s)	Pressure (kPa)	Viscosity (kPa-s)	Shear Rate (1/s)	Twist-Ply Angle	Static Shear (kPa)	Dynamic Shear (kPa)	Shear Modulus (kPa)
22.2	0.042	2	2.515	0.960	NT-0	***47.138***	***33.664***	***0.321***
22.2	0.042	24.132	2.515	1.149	NT-0	53.757	35.116	0.328
22.2	0.042	48.263	2.515	1.725	NT-0	46.412	33.241	0.186
22.2	0.21	2	2.515	4.801	NT-0	***92.750***	***42.450***	***0.643***
22.2	0.21	24.132	2.515	5.744	NT-0	81.947	59.051	0.448
22.2	0.21	48.263	2.515	8.627	NT-0	91.059	78.710	0.331
22.2	0.42	2	2.515	9.601	NT-0	***119.016***	***63.970***	***0.757***
22.2	0.42	24.132	2.515	11.488	NT-0	115.380	86.095	0.587
22.2	0.42	48.263	2.515	17.254	NT-0	142.794	129.062	0.487
22.2	0.84	2	2.515	19.431	NT-0	***120.600***	***50.670***	***0.896***
22.2	0.84	24.132	2.515	23.249	NT-0	177.579	131.506	0.833
22.2	0.84	48.263	2.515	34.920	NT-0	234.609	209.685	0.721
48.9	0.042	2	0.932	0.960	NT-0	25.974	15.020	0.228
48.9	0.042	24.132	0.932	1.149	NT-0	31.556	22.953	0.213
48.9	0.042	48.263	0.932	1.725	NT-0	***30.037***	***17.895***	***0.143***
48.9	0.21	2	0.932	4.801	NT-0	***31.910***	***15.068***	***0.295***
48.9	0.21	24.132	0.932	5.744	NT-0	48.949	36.455	0.308
48.9	0.21	48.263	0.932	8.627	NT-0	***51.411***	***42.580***	***0.245***
48.9	0.42	2	0.932	9.601	NT-0	54.237	26.615	0.437
48.9	0.42	24.132	0.932	11.488	NT-0	***81.510***	***68.360***	***0.500***
48.9	0.42	48.263	0.932	17.254	NT-0	83.743	71.429	0.352
48.9	0.84	2	0.932	19.431	NT-0	***81.137***	***27.712***	***0.654***
48.9	0.84	24.132	0.932	23.249	NT-0	103.448	69.163	0.599
48.9	0.84	48.263	0.932	34.920	NT-0	***141.945***	***120.814***	***0.520***
71.1	0.042	2	0.059	0.960	NT-0	***5.124***	***2.455***	***0.087***
71.1	0.042	24.132	0.059	1.149	NT-0	12.143	10.787	0.129
71.1	0.042	48.263	0.059	1.725	NT-0	***12.000***	***8.379***	***0.116***
71.1	0.21	2	0.059	4.801	NT-0	***15.240***	***6.580***	***0.213***
71.1	0.21	24.132	0.059	5.744	NT-0	23.586	18.538	0.211
71.1	0.21	48.263	0.059	8.627	NT-0	23.730	14.235	0.174
71.1	0.42	2	0.059	9.601	NT-0	23.378	8.372	0.295
71.1	0.42	24.132	0.059	11.488	NT-0	***44.116***	***29.427***	***0.409***
71.1	0.42	48.263	0.059	17.254	NT-0	***36.311***	***22.203***	***0.200***
71.1	0.84	2	0.059	19.431	NT-0	***41.904***	***14.768***	***0.450***
71.1	0.84	24.132	0.059	23.249	NT-0	***62.759***	***40.582***	***0.504***
71.1	0.84	48.263	0.059	34.920	NT-0	***57.230***	***35.500***	***0.300***

Table 20: Model Data for Never Twist Material and Ply Angle 45°

Temperature (°C)	Extension Rate (mm/s)	Pressure (kPa)	Viscosity (kPa-s)	Shear Rate (1/s)	Twist-Ply Angle	Static Shear (kPa)	Dynamic Shear (kPa)	Shear Modulus (kPa)
22.2	0.042	2	2.515	0.960	NT-45	***48.360***	***25.812***	***0.381***
22.2	0.042	24.132	2.515	1.149	NT-45	52.145	31.003	0.328
22.2	0.042	48.263	2.515	1.725	NT-45	49.692	39.840	0.241
22.2	0.21	2	2.515	4.801	NT-45	***90.131***	***42.666***	***0.645***
22.2	0.21	24.132	2.515	5.744	NT-45	92.439	63.444	0.527
22.2	0.21	48.263	2.515	8.627	NT-45	115.749	98.967	0.513
22.2	0.42	2	2.515	9.601	NT-45	***117.940***	***38.150***	***0.879***
22.2	0.42	24.132	2.515	11.488	NT-45	139.511	100.539	0.757
22.2	0.42	48.263	2.515	17.254	NT-45	190.884	165.079	0.812
22.2	0.84	2	2.515	19.431	NT-45	***141.410***	***52.050***	***0.982***
22.2	0.84	24.132	2.515	23.249	NT-45	224.468	164.513	1.165
22.2	0.84	48.263	2.515	34.920	NT-45	318.956	273.420	1.283
48.9	0.042	2	0.932	0.960	NT-45	19.551	5.108	0.169
48.9	0.042	24.132	0.932	1.149	NT-45	26.466	16.655	0.211
48.9	0.042	48.263	0.932	1.725	NT-45	20.583	9.357	0.189
48.9	0.21	2	0.932	4.801	NT-45	***31.890***	***12.160***	***0.300***
48.9	0.21	24.132	0.932	5.744	NT-45	51.612	36.218	0.348
48.9	0.21	48.263	0.932	8.627	NT-45	***58.077***	***32.695***	***0.268***
48.9	0.42	2	0.932	9.601	NT-45	57.199	26.511	0.440
48.9	0.42	24.132	0.932	11.488	NT-45	***82.010***	***60.130***	***0.504***
48.9	0.42	48.263	0.932	17.254	NT-45	110.583	91.075	0.554
48.9	0.84	2	0.932	19.431	NT-45	***83.430***	***24.658***	***0.623***
48.9	0.84	24.132	0.932	23.249	NT-45	125.934	88.227	0.754
48.9	0.84	48.263	0.932	34.920	NT-45	180.420	149.908	0.791
71.1	0.042	2	0.059	0.960	NT-45	***4.977***	***2.422***	***0.075***
71.1	0.042	24.132	0.059	1.149	NT-45	***12.390***	***8.159***	***0.226***
71.1	0.042	48.263	0.059	1.725	NT-45	19.804	13.895	0.136
71.1	0.21	2	0.059	4.801	NT-45	7.029	4.610	0.142
71.1	0.21	24.132	0.059	5.744	NT-45	***40.711***	***22.115***	***0.395***
71.1	0.21	48.263	0.059	8.627	NT-45	***23.610***	***13.388***	***0.188***
71.1	0.42	2	0.059	9.601	NT-45	18.201	2.946	0.252
71.1	0.42	24.132	0.059	11.488	NT-45	***39.691***	***22.752***	***0.426***
71.1	0.42	48.263	0.059	17.254	NT-45	56.068	40.351	0.388
71.1	0.84	2	0.059	19.431	NT-45	***37.920***	***12.820***	***0.401***
71.1	0.84	24.132	0.059	23.249	NT-45	61.370	36.246	0.503
71.1	0.84	48.263	0.059	34.920	NT-45	*58.920*	*34.930*	*0.334*

Table 21: Model Data for Standard Twist Material and Ply Angle 0°

Temperature (°C)	Extension Rate (mm/s)	Pressure (kPa)	Viscosity (kPa-s)	Shear Rate (1/s)	Twist-Ply Angle	Static Shear (kPa)	Dynamic Shear (kPa)	Shear Modulus (kPa)
22.2	0.042	2	2.515	0.960	ST-0	29.178	1.762	0.329
22.2	0.042	24.132	2.515	1.149	ST-0	48.734	34.490	0.337
22.2	0.042	48.263	2.515	1.725	ST-0	56.801	50.389	0.278
22.2	0.21	2	2.515	4.801	ST-0	***61.850***	***22.460***	***0.498***
22.2	0.21	24.132	2.515	5.744	ST-0	75.946	55.324	0.461
22.2	0.21	48.263	2.515	8.627	ST-0	103.208	92.082	0.438
22.2	0.42	2	2.515	9.601	ST-0	***75.719***	***29.929***	***0.448***
22.2	0.42	24.132	2.515	11.488	ST-0	106.664	77.910	0.599
22.2	0.42	48.263	2.515	17.254	ST-0	153.782	136.402	0.598
22.2	0.84	2	2.515	19.431	ST-0	***106.220***	***44.660***	***0.890***
22.2	0.84	24.132	2.515	23.249	ST-0	158.138	112.174	0.817
22.2	0.84	48.263	2.515	34.920	ST-0	231.561	200.120	0.783
48.9	0.042	2	0.932	0.960	ST-0	28.069	18.138	0.272
48.9	0.042	24.132	0.932	1.149	ST-0	45.602	37.021	0.344
48.9	0.042	48.263	0.932	1.725	ST-0	50.240	36.785	0.351
48.9	0.21	2	0.932	4.801	ST-0	***27.971***	***8.032***	***0.329***
48.9	0.21	24.132	0.932	5.744	ST-0	57.666	44.977	0.408
48.9	0.21	48.263	0.932	8.627	ST-0	73.895	59.136	0.420
48.9	0.42	2	0.932	9.601	ST-0	41.116	17.714	0.403
48.9	0.42	24.132	0.932	11.488	ST-0	***74.790***	***54.450***	***0.609***
48.9	0.42	48.263	0.932	17.254	ST-0	96.029	79.277	0.465
48.9	0.84	2	0.932	19.431	ST-0	***54.046***	***19.093***	***0.658***
48.9	0.84	24.132	0.932	23.249	ST-0	82.150	52.768	0.531
48.9	0.84	48.263	0.932	34.920	ST-0	***121.016***	***94.880***	***0.429***
71.1	0.042	2	0.059	0.960	ST-0	6.845	2.579	0.216
71.1	0.042	24.132	0.059	1.149	ST-0	33.612	28.473	0.324
71.1	0.042	48.263	0.059	1.725	ST-0	36.359	19.345	0.367
71.1	0.21	2	0.059	4.801	ST-0	***9.320***	***3.123***	***0.231***
71.1	0.21	24.132	0.059	5.744	ST-0	37.328	29.332	0.354
71.1	0.21	48.263	0.059	8.627	ST-0	47.477	31.037	0.385
71.1	0.42	2	0.059	9.601	ST-0	14.543	3.450	0.284
71.1	0.42	24.132	0.059	11.488	ST-0	***34.435***	***26.792***	***0.423***
71.1	0.42	48.263	0.059	17.254	ST-0	53.938	37.854	0.368
71.1	0.84	2	0.059	19.431	ST-0	***16.746***	***4.756***	***0.278***
71.1	0.84	24.132	0.059	23.249	ST-0	30.012	10.088	0.349
71.1	0.84	48.263	0.059	34.920	ST-0	***51.360***	***32.050***	***0.361***

Table 22: Model Data for Standard Twist Material and Ply Angle 45°

Temperature (°C)	Extension Rate (mm/s)	Pressure (kPa)	Viscosity (kPa-s)	Shear Rate (1/s)	Twist-Ply Angle	Static Shear (kPa)	Dynamic Shear (kPa)	Shear Modulus (kPa)
22.2	0.042	2	2.515	0.960	ST-45	***31.300***	***15.700***	***0.388***
22.2	0.042	24.132	2.515	1.149	ST-45	41.401	24.293	0.381
22.2	0.042	48.263	2.515	1.725	ST-45	55.807	44.162	0.368
22.2	0.21	2	2.515	4.801	ST-45	***60.069***	***25.431***	***0.606***
22.2	0.21	24.132	2.515	5.744	ST-45	60.415	56.761	0.598
22.2	0.21	48.263	2.515	8.627	ST-45	122.354	103.330	0.667
22.2	0.42	2	2.515	9.601	ST-45	***99.100***	***24.100***	***1.100***
22.2	0.42	24.132	2.515	11.488	ST-45	121.930	93.891	0.851
22.2	0.42	48.263	2.515	17.254	ST-45	204.183	169.494	1.001
22.2	0.84	2	2.515	19.431	ST-45	***103.300***	***27.200***	***0.980***
22.2	0.84	24.132	2.515	23.249	ST-45	238.953	157.935	1.306
22.2	0.84	48.263	2.515	34.920	ST-45	412.789	277.940	1.542
48.9	0.042	2	0.932	0.960	ST-45	***2.751***	***1.790***	***0.074***
48.9	0.042	24.132	0.932	1.149	ST-45	20.526	15.772	0.244
48.9	0.042	48.263	0.932	1.725	ST-45	5.461	3.100	0.296
48.9	0.21	2	0.932	4.801	ST-45	***14.340***	***4.885***	***0.276***
48.9	0.21	24.132	0.932	5.744	ST-45	44.311	35.363	0.400
48.9	0.21	48.263	0.932	8.627	ST-45	***63.724***	***43.028***	***0.363***
48.9	0.42	2	0.932	9.601	ST-45	36.554	15.564	0.442
48.9	0.42	24.132	0.932	11.488	ST-45	***77.000***	***57.900***	***0.586***
48.9	0.42	48.263	0.932	17.254	ST-45	118.318	101.317	0.723
48.9	0.84	2	0.932	19.431	ST-45	***46.051***	***10.793***	***0.560***
48.9	0.84	24.132	0.932	23.249	ST-45	118.134	87.477	0.876
48.9	0.84	48.263	0.932	34.920	ST-45	221.252	160.255	1.030
71.1	0.042	2	0.059	0.960	ST-45	***3.511***	***0.671***	***0.158***
71.1	0.042	24.132	0.059	1.149	ST-45	***17.065***	***11.088***	***0.314***
71.1	0.042	48.263	0.059	1.725	ST-45	30.620	21.510	0.232
71.1	0.21	2	0.059	4.801	ST-45	8.722	1.430	0.114
71.1	0.21	24.132	0.059	5.744	ST-45	24.680	13.627	0.266
71.1	0.21	48.263	0.059	8.627	ST-45	***33.771***	***21.183***	***0.252***
71.1	0.42	2	0.059	9.601	ST-45	4.664	2.380	0.243
71.1	0.42	24.132	0.059	11.488	ST-45	***36.335***	***20.156***	***0.510***
71.1	0.42	48.263	0.059	17.254	ST-45	60.243	53.804	0.546
71.1	0.84	2	0.059	19.431	ST-45	***13.042***	***4.303***	***0.324***
71.1	0.84	24.132	0.059	23.249	ST-45	40.797	38.707	0.614
71.1	0.84	48.263	0.059	34.920	ST-45	***52.300***	***31.100***	***0.385***

5.5.1.2 Correlations of Inter-Laminar Shearing to Experimental Variables

For each fiber twist and fiber orientation, the shear stress and shear modulus were plotted versus the static shear strain and viscosity for each normal pressure. These plots are provided in Appendix A. A subset of the graphs is provided in Figure 39 and Figure 40. From Equation 21, it is expected that the response would be linear when either the viscosity or the shear rate is held constant. The results show a generally linear response for both situations. It is of note that the slopes of both the viscosity and strain rate trends are not equivalent to the constant strain rate or viscosity, respectively. This indicates that the friction of the material also plays a contributing role in the inter-laminar shearing response.

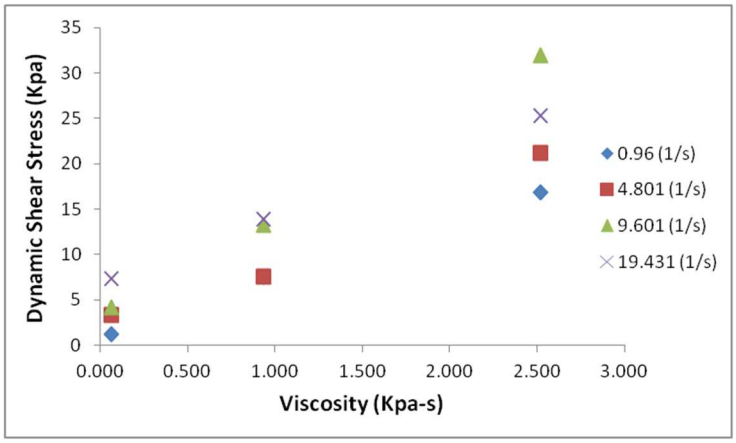

Figure 39: Effect of Viscosity with Never Twist 0° Oriented Shear

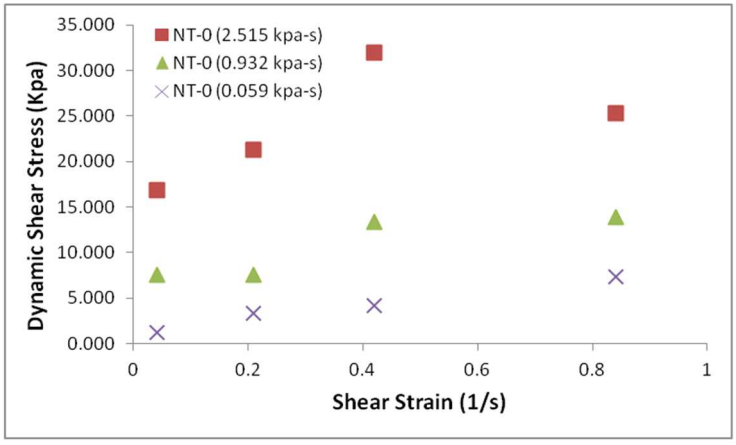

Figure 40: Effect of Strain with Never Twist 0° Oriented Shear

The linear response to the data shows that the models follow the trends of a Bingham Plastic (21). However, as mentioned, the slope of the trends is not equivalent to the variable held constant. For instance in Figure 40 the slopes of the data corresponding to the fluid viscosity yield 10.74, 8.9, and 7.36 kPa-s which do not correspond to the resin viscosities of 2.515, 0.932, and 0.059 kPa-s, respectively. This indicates that the Bingham plastic model is not sufficient to capture the full interaction of resin viscosity and frictional responses of the material.

5.5.1.3 Tribological Modeling of Inter-Laminar Shearing

Several authors have shown that a tribological approach can model thermoplastic prepreg slip [36,52,96]. The Stribeck curve can also be used to analyze thermoset prepregs although they do not follow the curve perfectly [83]. The Hersey number (33) relates the shear rate, viscosity and normal pressure to the coefficient of friction. The coefficient of friction (66) was calculated for both the static and dynamic shear stresses. Figure 41 shows the correlation between coefficient of dynamic friction and Hersey number.

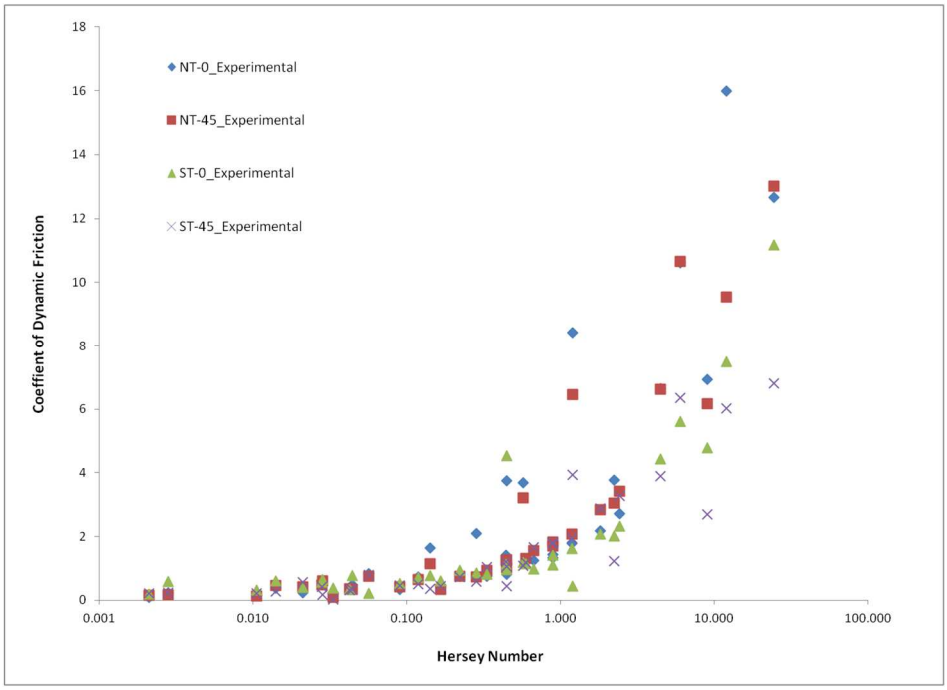

Figure 41: Coefficient of Dynamic Friction versus Hersey Number

A comparison of the differences between Figure 9 and Figure 41 shows that the prepreg does not follow the typical Stribeck curve. The prepreg does not exhibit a boundary friction region, nor does it show a large mixed friction region. The boundary friction region is dominated by solid body interactions such as non-lubricated friction and can be significantly reduced or eliminated by utilizing a lubricant. Larberg [80], has shown that the hydrodynamic region is largely dependent upon the material. For instance, 977-2 prepregs show an increase in friction at higher Hersey numbers while M21 prepregs exhibit a convergence to a minimum. Their results are consistent with ours in two ways. First, their reported tests also did not exhibit a boundary region of friction. Furthermore, only the transition from the mixed region to hydrodynamic was captured for several prepregs. In order to further characterize the lack of a boundary region, several inter-laminar shear tests were performed on dry standard twist fibers for ply angles of both 0/90 and ±45 degrees. These dry friction tests are provided in Table 23.

Table 23: Dry Friction Tests

	Coefficient of Static Friction	**Coefficient of Dynamic Friction**
ST-0	10.7	9.5
ST-45	3.1	3.0

The results show a large increase of friction for dry friction which would correspond to Hersey numbers of zero (no viscosity). These tests show that the boundary friction region does exist for very low Hersey numbers which for lubricated shearing could be achieved with large process pressures. Increasing normal pressures such as those during debulking processes or cures could cause boundary friction or mixed friction regions. However, the boundary region and mixed friction region would rarely be observed during normal forming process parameters.

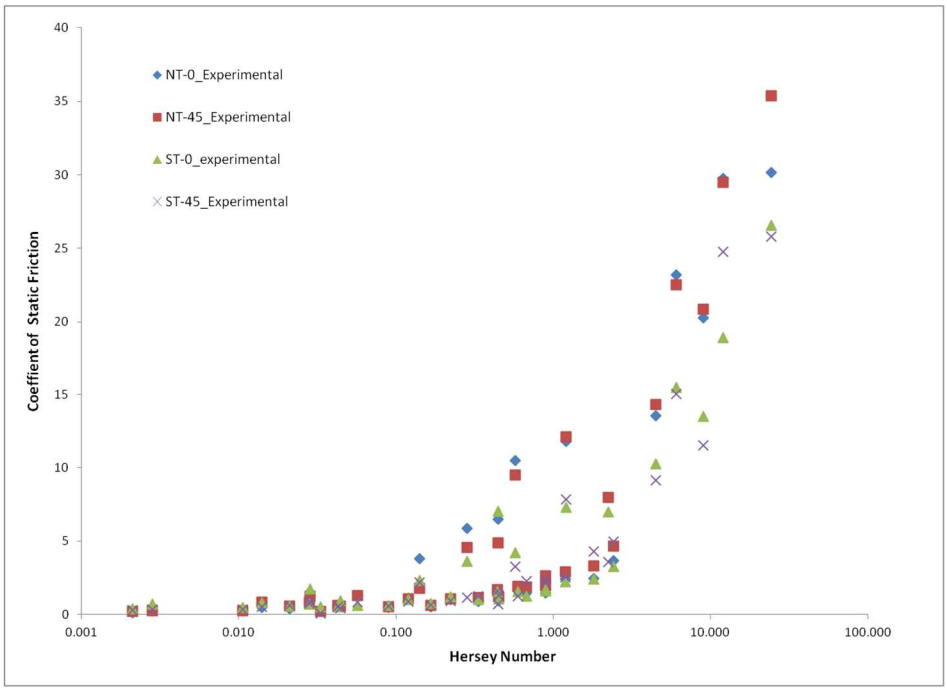

Figure 42: Coefficient of Static Friction versus Hersey Number

Both the coefficient of dynamic friction, Figure 41, and the coefficient of static friction, Figure 42, show the same type of response: the transition of the mixed friction region to the increasing friction of the hydrodynamic regime. The data follows Equation 68.

$$\mu_f = b\left(\frac{\mu\dot{\gamma}}{p}\right)^m \tag{68}$$

The values of b and m are provided in Table 24 for each fiber twist. A comparison of the material coefficients shows that the power coefficient m is a function of the material twist. The never-twisted sample has a tighter deviation than the standard-twisted sample. To verify that the exponents are significantly different, a two-way t-test was performed at a significance level of 5% or less. Considering all never-twisted and standard-twist coefficients from the static and dynamic friction fits exhibits a p-value of 0.020 confirming that the exponents are significantly different. The mean for the exponents are 0.54 and 0.44 for the never-twisted and standard-twist materials, respectively.

The t- test was also performed on the exponent m considering the ply orientation, and the p value was not significant, thus indicating that there was no significant difference between ply orientation for the exponent m. T-tests were also performed on the coefficient b considering both ply angle and fiber twist. Fiber twist was only significant for dynamic friction, and if all coefficients were considered for each classification, no variable was statistically significant.

Table 24: Trends for Coefficient of Frictions

	Material	b	m	R^2
CoSF	NT-0	3.987	0.564	0.779
	NT-45	4.198	0.563	0.820
	ST-0	3.370	0.438	0.741
	ST-45	3.040	0.514	0.783
CoDF	NT-0	2.392	0.527	0.842
	NT-45	2.201	0.518	0.868
	ST-0	1.689	0.368	0.733
	ST-45	1.549	0.449	0.757

T-tests were performed comparing the b coefficient for standard-twist and never-twist materials. No combination was statistically significant. Only when comparing the fiber twist for dynamic and static friction separately did the result approach significance. This indicates that ply orientation is not as impactful as fiber twist on the inter-laminar shear stress. Trends, shown in Figure 43 and Figure 44, were refit to the data based upon a consistent exponent m for the fiber twists which is provided in Table 25. Considering only the ply orientation of each material twist, the fit shows that the influence of ply angle changes for both the static and dynamic friction cases. For the both the static and dynamic friction response, the ply angle of 0° exhibits higher friction than 45° oriented plies.

Table 25: Friction Coefficients for Cycom 970 Prepregs

	Material	b	m	R2
CoSF	NT-0	5.604	0.54	0.842
	NT-45	5.927	0.54	0.891
	ST-0	5.249	0.44	0.851
	ST-45	5.330	0.44	0.831
CoDF	NT-0	2.720	0.54	0.793
	NT-45	2.632	0.54	0.872
	ST-0	2.255	0.44	0.853
	ST-45	1.796	0.44	0.833

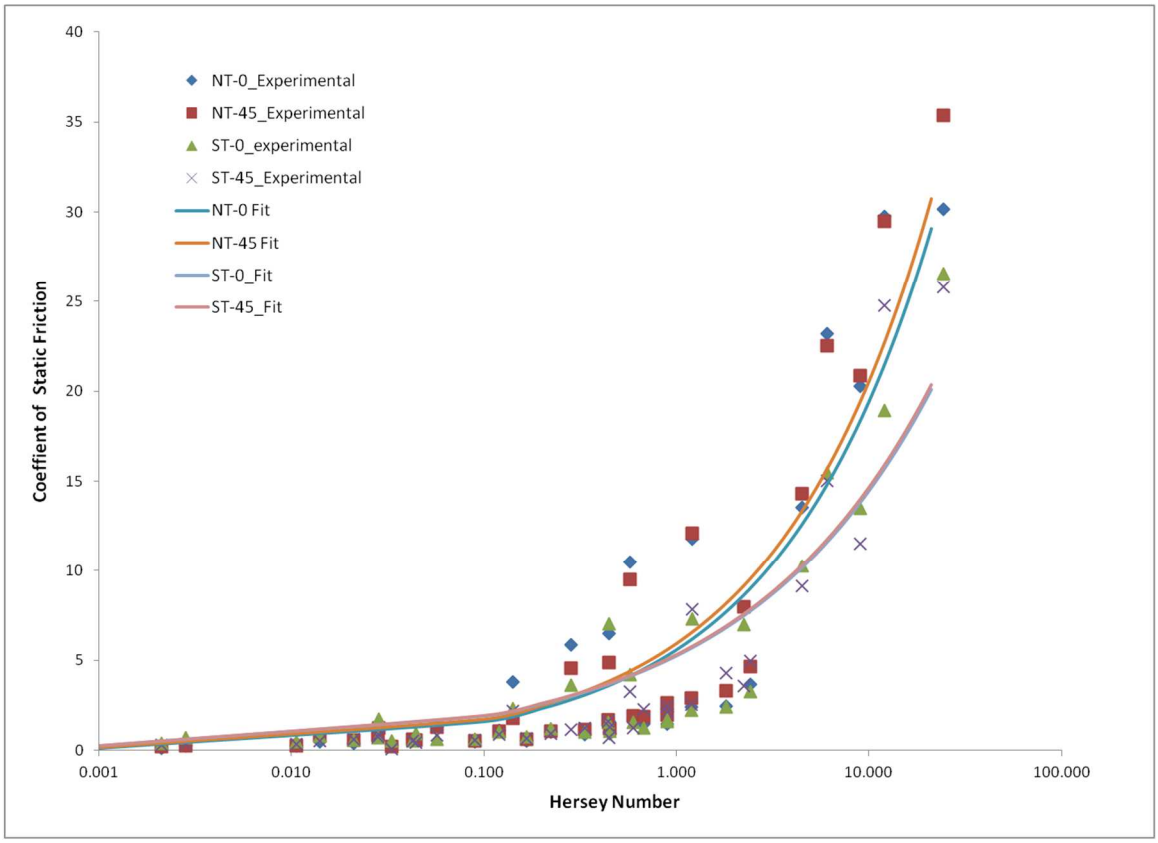

Figure 43: Experimental Data and Model for Coefficient of Static Friction

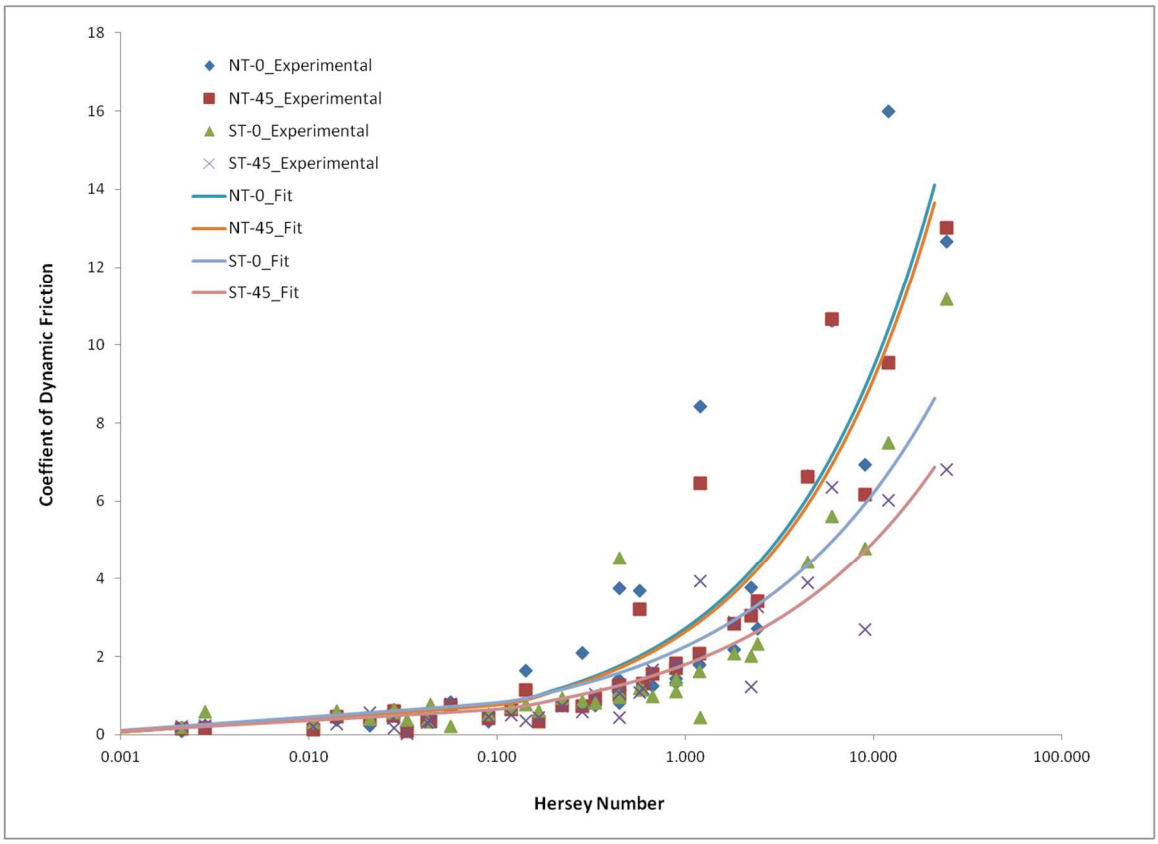

Figure 44: Experimental Data and Model for Coefficient of Dynamic Friction

Combining Equation 66 and Equation 68 yields the governing equation for inter-laminar shear stress (69): in which the process parameters are p, μ, and $\dot{\gamma}$ where p the normal pressure, μ is the resin viscosity, $\dot{\gamma}$ is the strain rate. The material constants are defined by m and b where m is a factor of the material twist type and b is a fitted parameter that is influenced by both ply orientation and material twist type and likely other unidentified factors.

$$\tau_f = bpH_s{}^m \tag{69}$$

The material constants for the prepregs produced with Cycom 970 resin are provided in Table 25. It is interesting to observe that in the mixed friction region — low Hersey numbers — the never twist fabric exhibits a lower shear required to initiate and sustain inter-laminar shearing. In the hydrodynamic friction region — high Hersey numbers — however, the never twist material results in a higher shear stress needed to initiate and sustain inter-laminar shearing.

The inflection of the fiber twist exhibiting higher inter-laminar stresses is unexpected since in the hydrodynamic friction region both surfaces are fully isolated by the resin layer. Given similar strain rates and external pressures, the friction coefficient would have been expected to be the same in the hydrodynamic region if the resin was equivalent.

Discussion of Hydrodynamic Region Friction Variation

Two possibilities exist to explain this friction variation. One of the initial assumptions used to calculate the resin film thickness was the difference between an uncured laminate and the cured thickness of the laminate. This assumption assumes that the debulk factor and thickness variation of the carbon prepeg is incorporated in the resin interface. These factors presumed to be equivalent between twist types could have induced differences in resin film thickness for the materials leading to differences in the coefficient of friction if subtle differences exist between twists.

The other possibility is that the viscosities are not the same between the low tack and high tack variants. To change the tack level, the manufacturer modifies the molecular weight of the resin such that the low tack resin will have a skewed distribution of molecular weight favoring higher molecular weights while the high tack variant will skew towards lower molecular weights. While the resin viscosity is considered equivalent for the different variations of the Cycom 970 prepreg, the Mark-Houwink equation does relate resin viscosity to molecular weight where lower molecular weights would reduce the resin viscosity even if ever so slightly. The hydrodynamic isolation of the two friction surfaces would take longer to build and lead to higher friction coefficients with a resin with a lower molecular weight compared to a resin with a slightly higher molecular weight. These results seem to indicate that the material tack level has an indirect relationship with inter-laminar friction in the hydrodynamic friction regime.

5.5.1.4 Modeling of Shear Modulus

The tribological approach was also used to determine the governing equations for the shear modulus. Figure 45 represents the typical response of the shear modulus plotted against the Hersey number (H). The shear modulus difference between tested pressures of 24 kPa and 48 kPa are indistinguishable. Thus, the strain corresponding to the maximum shear stress was analyzed. This critical strain was calculated using Equation70.

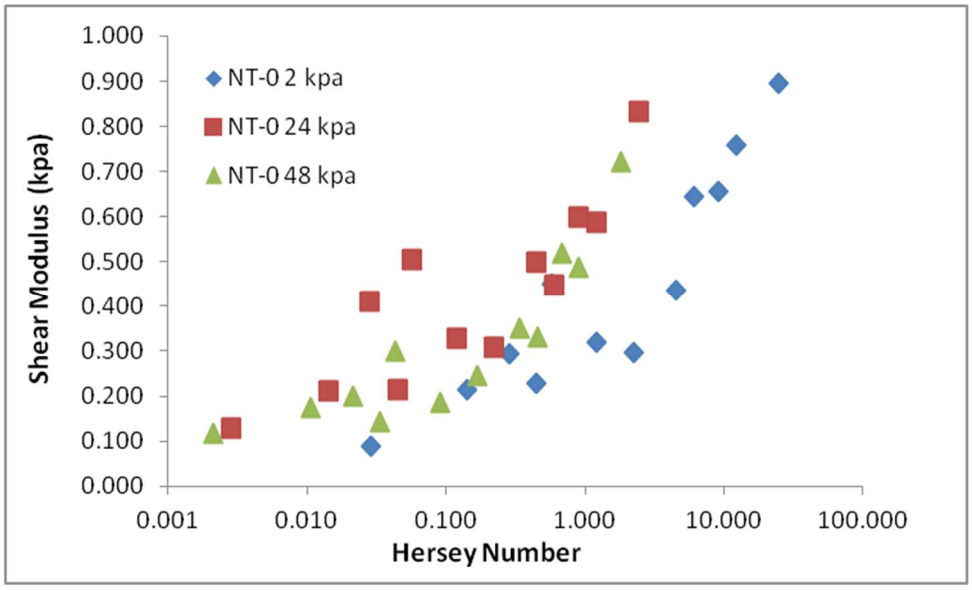

Figure 45: Hersey Number versus Shear Modulus for Never Twist 0° Material

$$\gamma_c = \frac{\tau_{static}}{G} \tag{70}$$

The critical shear strain shows a better distinction between the various test conditions shown in Figure 46 through Figure 49 for never twisted and standard twist materials.

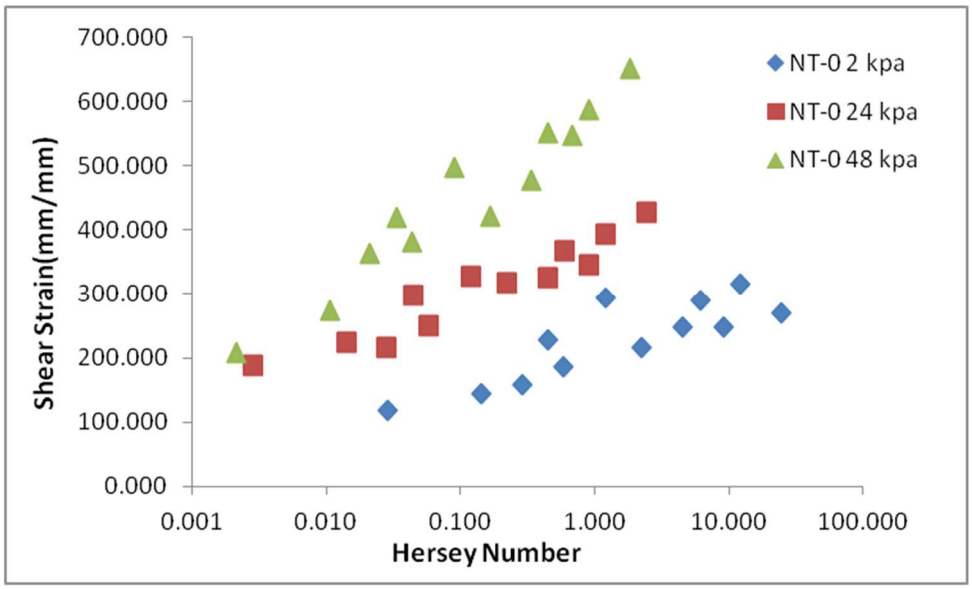

Figure 46: Critical Shear Strain for Never Twist with Ply Angle 0°

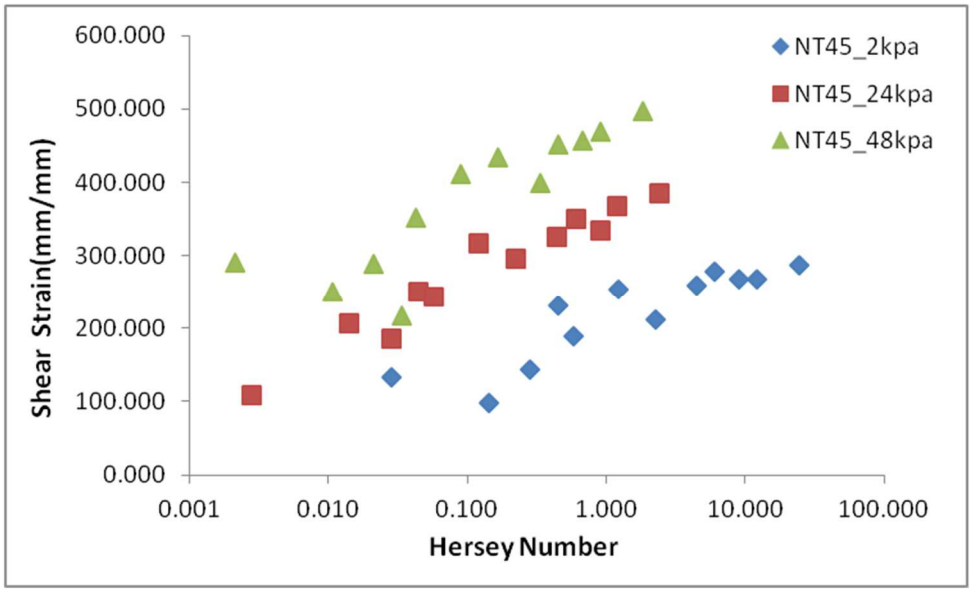

Figure 47: Critical Shear Strain for Never Twist with Ply Angle 45°

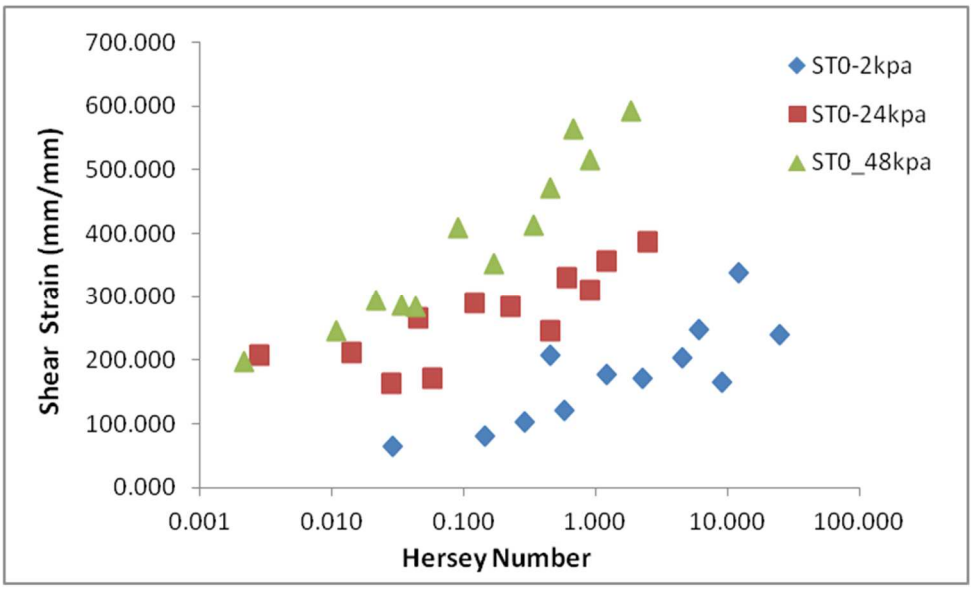

Figure 48: Critical Shear Strain for Standard Twist with Ply Angle 0°

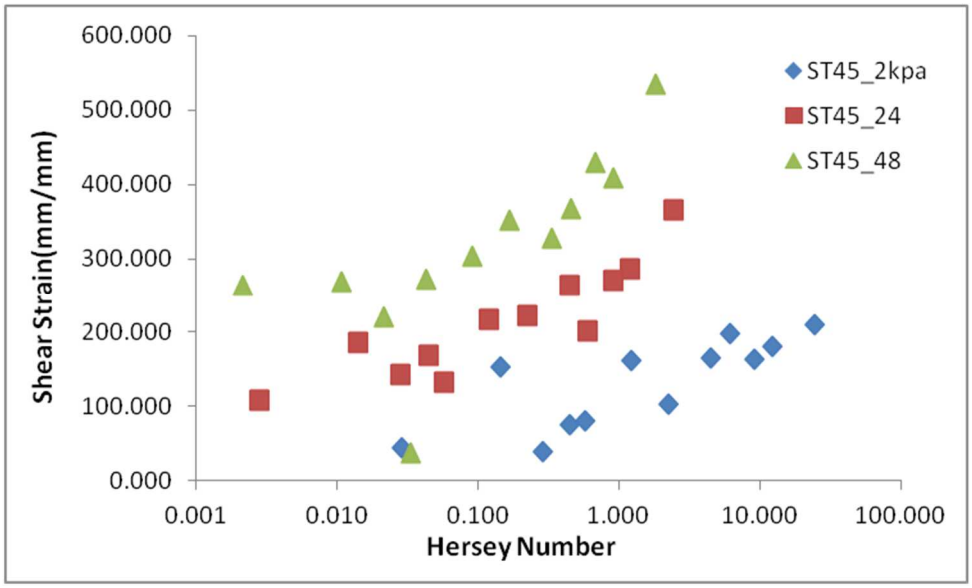

Figure 49: Critical Shear Strain for Standard Twist with Ply Angle 45°

The shear strain for each pressure follows a power equation outlined by Equation 71. The fit coefficients are provided in Table 27. A t-test comparing the m_γ coefficient for standard twist versus never twist fibers was statistically significant demonstrating the m_γ coefficients to be significantly different for these two groups of fibers. The material twist comparison also shows that the exponents are statistically significantly different.

$$\gamma_c = b\left(\frac{\mu\dot{\gamma}}{p}\right)^{m_\gamma} \tag{71}$$

Table 26: Fit Parameters for Critical Shear Strains

Fiber Twist/ Ply Orientation	Pressure (kPa)	b	$\mathbf{m_\gamma}$
NT-45	2	89.694	0.129
NT-45	24	108.952	0.141
NT-45	48	152.128	0.114
NT-0	2	94.274	0.117
NT-0	24	128.59	0.119
NT-0	48	166.182	0.142
ST-0	2	63.144	0.184
ST-0	24	113.616	0.120
ST-0	48	139.306	0.172
ST-45	2	37.414	0.195
ST-45	24	84.58	0.171
ST-45	48	106.338	0.173

The coefficient b was recalculated based upon a common exponent for both twist materials. The coefficient b is a function with respect to normal pressure. The trends follow a linear distribution outlined by equation 72 and coefficient iterations are provided in Table 28. The first iteration reveals that the coefficient c is statistically significant with respect to ply orientation. Then iteration 2 shows that the coefficient Po is significant with respect to fiber twist. It is interesting to note how the fiber twist influences the intercept while the ply orientation affects the slope. This differs from the shear model where the b coefficient was not significantly influenced by material variables.

$$b = cP + P_o \tag{72}$$

Table 27: Shear Strain Coefficient Fit with Uniform m

Fiber Twist/ Ply Orientation	Pressure (kPa)	b	m_γ	R^2
NT-45	2	102.1	0.127	0.774
NT-45	24	176.82	0.127	0.891
NT-45	48	242.4	0.127	0.769
NT-0	2	106.18	0.127	0.695
NT-0	24	190.56	0.127	0.912
NT-0	48	330.9	0.127	0.908
ST-0	2	79.9	0.169	0.641
ST-0	24	169.696	0.169	0.627
ST-0	48	268.4	0.169	0.939
ST-45	2	59.7	0.169	0.642
ST-45	24	141.46	0.169	0.839
ST-45	48	218.4	0.169	0.605

Table 28: Coefficient Iterations for b coefficient versus P

		Iteration 1			Iteration 2		
Fiber Twist	Ply Orientation	C	P_o	R^2	C	P_o	R^2
NT	0	4.900	88.352	0.986	4.5	97.62	0.980
NT	45	3.446	54.844	0.998	3.24	93.42	0.991
ST	0	4.098	71.58	1	4.5	61.08	0.989
ST	45	3.044	98.658	0.996	3.24	59.5	0.995

The governing equation for the critical shear strain is provided in Equation 73 with the coefficients provided in Table 29. In Appendix B.1 the model is plotted with the experimental data and shows good adherence at the tested normal pressures. At low pressures, the fiber type (P_o) dominates the critical shear. Appendix B.3 shows that the never-twist and standard-twist tests at 0° and 45° ply orientations follow the same trend while the two twists of fiber deviate. The never-twisted prepregs have a higher critical strain before slip occurs than the standard-twist fibers. As the normal pressure increases, the ply orientation (C) gains influence. At higher normal pressures, the 0° standard twist and never twist converge, whereas the 45° standard twist

and never twist converge at a lower strain value. These results and the results of the shear stress (Equation 69) seem to confirm the results presented by others [3,109] that suggest a laminate of similar plies [45,45] or [0,0] has lower inter-laminar friction than a similar balanced laminate of [0,45].

$$\gamma_c = (cp + p_o)\left(\frac{\mu\dot{\gamma}}{p}\right)^{m_\gamma} \tag{73}$$

Table 29: Coefficients for Critical Shear Strain

Fiber Twist	Ply Orientation	C	P_0	m_γ
NT	0	3.24	95.52	0.127
NT	45	4.5	95.52	0.127
ST	0	3.24	60.3	0.169
ST	45	4.5	60.3	0.169

The shear modulus can then be determined by substituting Equation 69 and Equation 73 into Equation 70. The coefficients are provided in Table 25 and Table 29. Appendix B.2 provides plots of the shear modulus versus experimental data. The model corresponds well for low pressures but slightly overestimates the modulus for the higher pressures. The model is also dominated primarily by the fiber type. Appendix B.4 provides plots of the model at various pressures. In each case, the similar ply angle (0°) shear case has a lower modulus than the off-angle (45°) shear case. At low pressures and Hersey numbers, the standard twist fibers have a higher shear modulus than the never twisted fibers. The trends intersect roughly at H=10 which is well within the hydrodynamic friction regime. This intersection point decreases as pressure increases such that at 48 kPa the intersection is roughly at H=2.

$$G = \frac{bp}{(cp+p_o)}\left(\frac{\mu\dot{\gamma}}{p}\right)^{m-m_\gamma} \tag{74}$$

5.5.1.5 Inter-laminar Toughness

From the inter-laminar shear stress and the critical shear strain, the toughness of the materials can be determined by calculating the area under the stress strain curve to the point where slip occurs. The plots of toughness versus Hersey number are provided in Appendix B.5. Never twist materials possess higher toughness at all Hersey numbers and pressures than the standard twist counterparts. Additionally, slip between ply angles have a higher toughness than the corresponding off-angle slip within a given fiber twist. In light of these results and the results reported in [3,109], prepregs with higher toughness are able to absorb before slip occurs reducing wrinkle formation.

5.5.2 Influence of Inter-Laminar Shearing on Forming Processes

The inter-laminar shearing tests showed that the fiber twists influence the inter-laminar shearing response. For the shear stress, the material twist's influence dominates confirming the first part of Hypothesis 2. At Hersey numbers less than 1, the standard twist and never twist nearly have the same stress. But at higher Hersey numbers, the twist type influences the stresses developed. There was no direct influence of the ply angle on shear stress. At low pressures, the fiber type dominates the critical shear while at higher pressures ply orientation gains influence. Both the strain and stress plots show their minimums at low Hersey numbers with large inflections occurring around H=2 at the transition from mixed friction to hydrodynamic friction.

Composite forming is often done at low pressures while debulking operations are done at higher pressures. In typical hot drape forming processes, the flange is fully formed by 13.5 kPa (4 inHg). At the onset of the forming process as the flange forms along the radius, the fiber twist is the influential material variable. Then as the forming process proceeds, the laminate is formed into the flange features, such as joggles. This forming step is performed at higher pressures than

the initial step and thus has influence of the ply orientation or part stacking sequence for forming onto the tool. Once the part is fully formed, compaction or debulking occurs. Full vacuum (100 kPa) is applied, at this stage.

5.6 Hot Drape Formed C-channels

Section 5.6 and it's subsections report the results of the hot drape forming experiments addressing Hypotheses 2, 3, and 4. Section 5.6.1 addresses Hypothesis 3 which states that the drapability of a ply in a laminate is not affected by inter-laminar effects. Section 5.6.2 addresses The second part of Hypothesis 2 and Hypothesis 4. The second part of Hypothesis 2 states that by eliminating fiber twist, the inter-laminar shear will decrease effectively reducing out-of-plane wrinkling compared to similar c-channels formed with twisted fabrics. Hypothesis 4 states that an optimum resin viscosity can be shown to exist for drape forming. Table 30 summarizes the results from the forming experiments. All wrinkle types, Figure 3, were observed in the flanges of the c-channel; chord web wrinkles were also observed.

Table 30: Green State Wrinkle Measurements

Resin System	Fabric Weave	Ply Count	Temp-erature (°C)	Wrinkle Location	Wrinkle Type	Average H (mm)	Average L (mm)	Average D (mm)	Average L/D (mm/mm)
970	PW-ST	10	60	Flange	Chord	18.2	10.6	0.05	150
970	PW-ST	18	60	Flange	Chord	30.5	13.0	0.8	15.5
970	PW-ST	30	22	Flange	Chord	59.3	16.1	2.6	8.0
970	PW-ST	30	22	Flange	Off-Angle	55.1	10.9	0.8	15.2
970	PW-ST	30	22	Web	Chord	53.3	9.1	0.5	17.3
970	PW-ST	30	38	Flange	Chord	24.8	13.6	1.5	12.5
970	PW-ST	30	38	Web	Chord	80.1	10.8	0.4	38.1
970	PW-ST	30	49	Flange	Chord	24.8	8.9	0.5	20.9
970	PW-ST	30	49	Web	Chord	91.4	11.4	0.5	26.7
970	PW-ST	30	60	Flange	Chord	23.4	10.4	0.9	55.0
970	PW-ST	30	60	Web	Chord	55.4	11.7	0.8	16.9
970	PW-ST	30	71	-	-	-	-	-	150
970	PW-ST	30	82	-	-	-	-	-	150
970	PW-NT	30	22	Flange	Off-Angle	42.7	7.6	0.5	21.3
970	PW-NT	30	22	Flange	Chord	44.5	9.4	1.1	8.9
970	PW-NT	30	22	Web	Chord	72.1	9.9	1.0	10.1
970	PW-NT	30	38	Flange	Chord	53.34	8.72	0.728	37.7
970	PW-NT	30	49	-	-	-	-	-	150
970	PW-NT	30	60	-	-	-	-	-	150
970	PW-NT	30	71	-	-	-	-	-	150

5320-1	UD	18	52	Flange	Chord	43.8	4.7	10.4	0.6
5320-1	UD	18	52	Flange	Off-Angle	121.3	7.1	12.8	0.6
5320-1	UD	18	52	Web	Chord	86.6	7.1	12.1	0.6
5320-1	PW	18	52	Flange	Chord	46.0	8.2	1.6	9.3
5320-1	8H	18	52	-	-	-	-	-	150

5.6.1 Effect of Intra-Laminar Shear

The 5320-1 system c-channels were all formed at 52 °C and possess similar symmetrical laminates of 18 plies. The UD c-channel exhibited wrinkles on the web and the flanges, as shown in Figure 50. The flange wrinkles included both off-angle and span wrinkles through the joggle region and chord wrinkles at the inset of the joggle. These wrinkles correspond to locations predicted by Sjölander et. al. [109] for the quasi c-channels indicating that the additional +45 plies at the plane of symmetry did not influence the forming result from a typical quasi-isentropic laminate. The wrinkles of the 5320-1 UD c-channel were measured in the green state and thus were larger than those presented in [1,108] which were measured post autoclave cure.

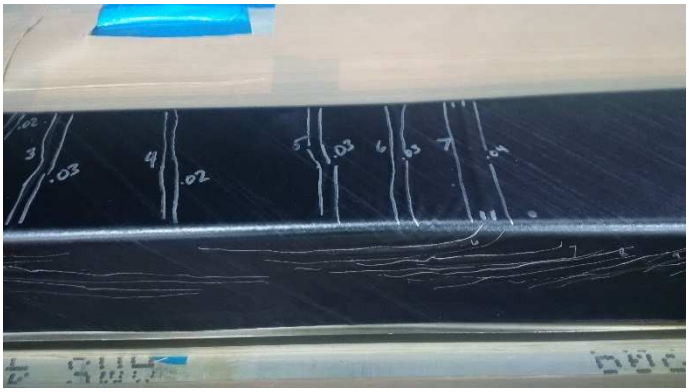

Figure 50: Typical UD Wrinkles

The PW and 8H laminates more closely represented a UD laminate of [+45,-45,90,0] or [45,90,-45,90] paired plies, in [3,109] case QI DL and CS 45/90, respectively. This pairing was shown to reduce the span and off-angle wrinkles but did not fully eliminate them. On the other

hand, the weaves created a PJN on each ply. The (0/90) plies follow a natural path as they conform into the joggle region rather than following a geodesic curve. The global tension of the [0] plies was also observed as a local tension in the (0/90) plies inducing additional intra-laminar shearing.

Neither the PW nor 8H c-channels possessed any post formed span or off-angle wrinkles as shown in Figure 51 and Figure 52 with the winkles marked. These results correspond well to the aforementioned cases of QI DL and CS 45/90 thereby validating the assumption and the inter-laminar shearing results that the off-angle (45/0) interface can lead to the span and off-angle wrinkles. Additionally, the PW specimen did have slight chord wrinkles in local compression zones outside the joggle similar to the results reported for both QI DL and CS 45/90. On the other hand, the 8H samples did not have any type of wrinkle or waviness.

Figure 51: Typical PW Wrinkles

Figure 52: Wrinkle Free 8H C-Channels

This indicates that the intra-laminar shearing behavior greatly affects the out-of-plane wrinkles. Thus Hypothesis 3 can be accepted. The increased locking angles of the 8 harness satin material allowed the plies to deform by a larger amount, allowing it to conform to the c-channel geometry without wrinkles. It may be suitable to adopt a woven fabric material to conform to more challenging c-channel geometries than a UD material can accommodate further enabling more weight competitive designs.

5.6.2 Effect of Inter-Laminar Shear

The effect of the inter-laminar shearing was investigated using Cycom 970 PW standard-twist and never-twist c-channels. Averaged experimental results are provided in Table 30. A direct comparison to the wrinkles sizes of the 5320-1 PW specimen was not be made due to differences in resin viscosities but it is observed that the wrinkles formed using the 970 samples were located in similar positions to that of the 5320-1 tests and published by Sjölander in [109] further validating the experimental results.

The spars were formed at various Hersey numbers which are outlined in Table 31 for the various test conditions outlined in Table 6. Viscosity was calculated for each condition according to Equation 64. The strain rate depends upon the total ply count, tool radius, and vacuum rate. A small pressure of 2 kPa was assumed for an initial pressure as the hand layup will compact the plies slightly.

Table 31: Hersey Numbers for HDF Test Parameters

Ply Count	Temperature (°C)	Viscosity (kPa-S)	Strain Rate (1/s)	Pressure Initial (kPa)	Hersey Number
10	60.0	0.10	0.66	2	0.03
18	60.0	0.10	1.32	2	0.06
30	22.2	2.51	1.99	2	2.50
30	37.8	0.93	1.99	2	0.93
30	48.9	0.37	1.99	2	0.37
30	60.0	0.10	1.99	2	0.10
30	71.1	0.06	1.99	2	0.06
30	82.2	0.04	1.99	2	0.04

5.6.2.1 Chord Wrinkle

When the never-twist and standard-twist samples of 30 plies are evaluated, the effect of Hersey number on chord wrinkle development can be observed in Figure 53. The room temperature tests did exhibit off-angle wrinkles which were not included in Figure 53. The decreasing Hersey number shows a decrease in wrinkle magnitude (increasing L/D).

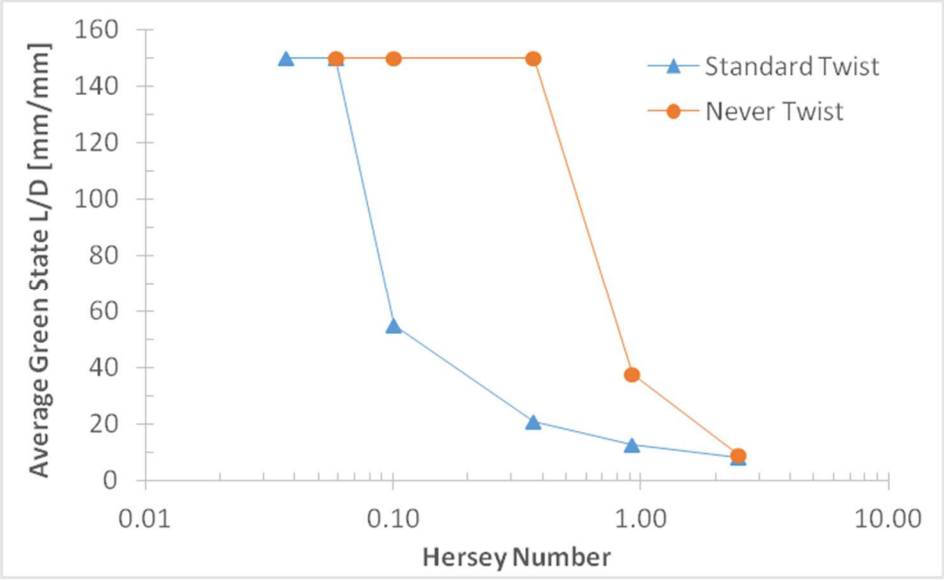

Figure 53: Effect of Forming Parameters on Wrinkle Size

It is interesting to note that, at room temperature, the resulting wrinkles between the standard-twist and never-twisted tests are similar and possess both chord and off-angle wrinkles.

This indicates that other material properties influence wrinkle development at low temperatures while inter-laminar shearing dominates at higher temperatures. This corresponds well with the previously reported tack data where at temperatures below 31 °C, the resin does not flow. This can be further confirmed by considering the spars formed at 38 °C (H=0.98). The standard-twist and never-twisted spar chord wrinkles begin to deviate at these test parameters showing that the material twist begins to influence the forming. The inability of the resin to flow limits the ability of the weaves to distort according to the PJN theory thus creating an undesired effective pairing of [45,0] laminates. This causes the laminate to behave similar to the QI Ref sample [109] yielding similar wrinkle types as the model and UD experiments.

Between the two prepregs, the resin viscosity is equivalent thus the differences observed in wrinkle formation are due to the differences of coefficient of friction caused by the inter-laminar shearing. As expected, the standard-twist laminates produced larger wrinkles than the never-twisted laminates at similar Hersey numbers. Thus hypothesis 2 can be accepted. The never-twisted laminates produce a wrinkle free spar at Hersey numbers ≤0.37 while the standard-twisted laminates produce a wrinkle free spar at Hersey numbers ≤0.1. These Hersey numbers correspond to a critical inter-laminar shear stress for one off-angle ply of 180 kPa and 120 kPa for never-twisted and standard-twist material forms.

Hypothesis 4 fails to be accepted in its entirety. While the resin viscosity does play a pivotal role in reducing shear and out-of-plane wrinkles, it was shown in this data and Section 5.5.1.3 that it is not the only factor. Both the shear rate and pressure also affect the formation of wrinkles governed by the Hersey number. Thus, any forming modeling should take into account the shear rate and initial pressure which this hypothesis failed to consider.

Influence of ply count

Changing the ply count of a laminate affects the strain rate. Fewer plies require less strain to fully form thus lowering the strain rate and effectively the Hersey number at an equivalent temperature. Evaluating the standard-twist c-channels formed at 60 °C shows that as the ply count increases, the magnitude and frequency of the wrinkles also increases. The 10-ply charge possessed very small green state waviness, averaging 0.05 mm in depth, which is the tolerance of the micrometer used to measure the wrinkle leading to an L/D > 150. The 18-ply charge possessed one wrinkle in the flange with an L/D of 15.4. While this wrinkle would not dissipate during cure, it was less pronounced than the 11 wrinkles in the 30-ply charges with L/D's ranging from 5 to 150. Excluding the wrinkles with an L/D of greater than 100, the average wrinkle L/D in the 30-ply charge was 13.1.

Traditional spars for aerospace applications have a varying ply count depending upon the load transferred from the skin and fittings. This then would cause various strain rates and thus Hersey numbers to be experienced along the spar during forming operations. From practical experience, the wrinkles occur at the thickest portion of the laminate or highest Hersey number. To mitigate these wrinkles, forming parameters should be chosen based upon the maximum ply count. Often, the forming temperature is mandated by process specifications; thus, the strain rate is often the most easily changeable variable. Figure 54 shows how the coefficient of static friction varies for a never twist off-angle slip while varying the strain rate. Both the ply count and vacuum rate affect the strain rate. At higher ply counts, it is necessary to decrease the vacuum rate to achieve an equivalent coefficient of friction.

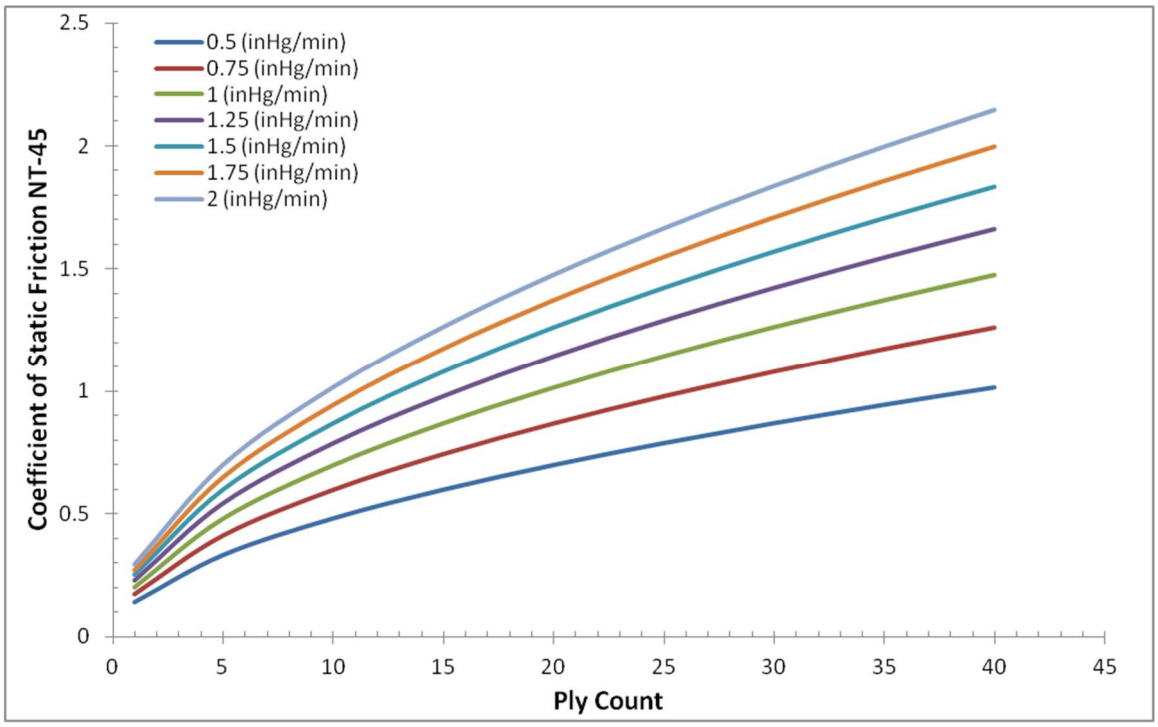

Figure 54: Strain Rate affect on Coefficient of Friction for Various Ply Counts

Influence of initial pressure

Over the course of the tests, it has been repeatedly shown that lower Hersey numbers reduce the inter-laminar shear stress and produce better parts. Recalling Equation 33, the Hersey number is proportional by viscosity and shear rate while inversely proportional to pressure. To the inexperienced observer, the best way to reduce the Hersey number is to increase the initial laminate compaction. Practical experience, on the other hand, shows that increased initial pressure will lead to larger wrinkles. This is partially because the pressure also directly influences the static shear stress and the critical shear strain, Equations 69 and 73, respectively. Thus, with increasing debulk pressure the total pressure on the laminate also will increase, causing the stress needed to induce slip to increase.

The additional debulk pressure also will affect the intra-laminar shear. Larberg et. al. [57], report that a series of uni-directional plies fully debulked and tested via the bias extension

test acts as a plain weave material. Thus, it is theorized that for a multi-ply laminate, the full debulking will entangle the plies affecting the intra-laminar slip initiating wrinkle formation.

5.6.2.2 Web Wrinkles

One final point needs to be made that is not obvious from looking at the data. In these experiments, web wrinkles occurred during forming of several different test articles independent of fiber twist. While these wrinkles are observed and predicted in the UD c-channels [3,109], the PW and 8H weaves should have eliminated these wrinkles at elevated temperatures. It was determined, through the experiments, that the transfer of the laminate from the layup table to the tool was creating excess sagging in the charge which was observed to correlate with the ST's web wrinkle locations. The transfer method was adjusted to eliminate the sagging for the remainder of the experiments. The never-twist tests show that the modification was sufficient to eliminate the web wrinkles on the spars. This indicates that many external factors can influence wrinkle development, and care needs to be taken while handling and preparing the flat charges.

CHAPTER 6 – WRINKLE PREDICTION MODEL

Chapter 6 addresses Hypothesis 5 which states that a direct correlation exists between inter-laminar shearing and out-of-plane wrinkle development which can be modeled using laminated plate theories.

6.1 Modeling Approach

This section discusses the modeling approach used to characterize buckling in un-cured (green) prepregs.

6.1.1 Green Laminated Plate

The green laminate consists of both prepreg ply layers and resin interface layers. Several assumptions were made to further define the green laminated plate model.

1. The interface between two adjacent prepreg plies acts as an individual layer representing all visco-elastic effects of the resin.
2. The interface properties are representative of all inter-laminar friction.
3. The bulk factor of the prepreg is represented in the interface layer.
4. Only the resin interface shears during forming operations. Prepreg layers are inextensible during forming operations and do not contribute to the critical shear stress

A prepreg layup, such as those provided in Table 8, consisting of k prepreg layers would have additional resin layers defined by Equation 75. Each resin interface would reside between the prepreg plies transforming the laminate shown in Figure 4 to that shown in Figure 55. For a layup with symmetry between plies, the green layup will have symmetry about the mid-plane resin interface layer (Figure 55).

$$k^i = k^p - 1 \tag{75}$$

$$\theta_k^i = |\theta_{k+1}^p - \theta_{k-1}^p| \tag{76}$$

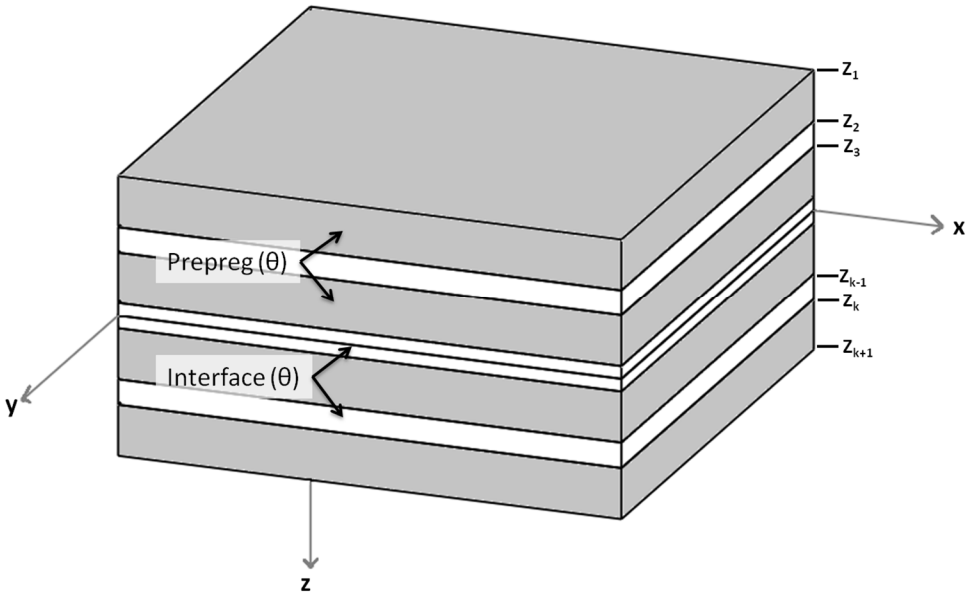

Figure 55: Green Laminated Plate Layup

The interface angle is a function of the prepreg layers such that the difference of the two adjacent prepreg layers defines the interface, shown in Equation 76. For instance, in a plain weave material with alternating 0/90 and ±45 layers, all interfaces would be characterized by a 45° interface except that of the mid-plane which would be a 0° interface.

6.1.2 Resin Interface Properties

The resin interface properties: E_x, E_y, ν_{12}, and G_{xy}, are all needed to fully characterize the interface in the laminated plate theories. G_{xy} must be experimentally determined and is defined by Equation 74. The Poisson's ratio and elastic modulus can be calculated using the shear modulus (G) and bulk modulus (K) as shown in Equations 77 and 78, respectively. Since $G_{xy}=G_{yx}$, for plain weave materials, $E_x=E_y$.

$$\nu_{xy} = \frac{3K-2G}{6K+2G} \tag{77}$$

$$E = \frac{9KG}{3K+G} \tag{78}$$

G_{xz} also needs to be determined for the first-order shear displacement theory (FSDT) buckling equations. G_{xz} is influenced by the prepreg tack (section 5.4) when the laminate is being pulled apart and the debulk modulus (section 5.2) when the laminate is being compressed. Since the forming operations are under vacuum, σ_{xz} is negative.

$$G_{xz} = \begin{cases} G_{debulk}, & \sigma_{xz} < 0 \\ G_{tack}, & \sigma_{xz} \geq 0 \end{cases} \tag{79}$$

6.2 Calculation of Laminate Constitutive Equation

For a plain-weave material, E_x=E_y. Thus, the Q_{ij} equations will reduce to Equations 80-83

$$Q_{11}^{i,p} = Q_{22}^{i,p} = \frac{E^{i,p}}{1-\nu^{i,p}\nu^{i,p}} \tag{80}$$

$$Q_{66}^{i,p} = G_{xy}^{i,p} \tag{81}$$

$$Q_{12}^{i,p} = \frac{\nu^{i,p}E^{i,p}}{1-\nu^{i,p}\nu^{i,p}} \tag{82}$$

$$Q_{55}^{i,p} = Q_{44}^{i,p} = G_{13}^{i,p} \tag{83}$$

The $\bar{Q}$ then can be calculated by Equations 84 – 89

$$\bar{Q}_{11}^{i,p} = Q_{11}^{i,p}\cos^4\theta^{i,p} + 2\left(Q_{12}^{i,p} + 2Q_{66}^{i,p}\right)\cos^2\theta^{i,p}\sin^2\theta^{i,p} + Q_{22}^{i,p}\sin^4\theta^{i,p} \tag{84}$$

$$\bar{Q}_{12}^{i,p} = \left(Q_{11}^{i,p} + Q_{22}^{i,p} - 4Q_{66}^{i,p}\right)\cos^2\theta^{i,p}\sin^2\theta^{i,p} + Q_{12}^{i,p}\left(\sin^4\theta^{i,p} + \cos^4\theta^{i,p}\right) \tag{85}$$

$$\bar{Q}_{22}^{i,p} = Q_{11}^{i,p}\sin^4\theta^{i,p} + 2\left(Q_{12}^{i,p} + 2Q_{66}^{i,p}\right)\cos^2\theta^{i,p}\sin^2\theta^{i,p} + Q_{22}^{i,p}\cos^4\theta^{i,p} \tag{86}$$

$$\bar{Q}_{16}^{i,p} = \left(Q_{11}^{i,p} - Q_{12}^{i,p} - 2Q_{66}^{i,p}\right)sin\,\theta^{i,p}\cos^3\theta^{i,p} + \left(Q_{12}^{i,p} - Q_{22}^{i,p} + 2Q_{66}^{i,p}\right)cos\,\theta^{i,p}\sin^3\theta^{i,p} \tag{87}$$

$$\bar{Q}_{26}^{i,p} = \left(Q_{11}^{i,p} - Q_{12}^{i,p} - 2Q_{66}^{i,p}\right)cos\,\theta^{i,p}\sin^3\theta^{i,p} + \left(Q_{12}^{i,p} - Q_{22}^{i,p} + 2Q_{66}^{i,p}\right)sin\,\theta^{i,p}\cos^3\theta^{i,p} \tag{88}$$

$$\bar{Q}_{55}^{i,p} = Q_{55}^{i,p}\cos^2\theta^{i,p} + Q_{44}^{i,p}\sin^2\theta^{i,p}$$

$$\bar{Q}_{66}^{i,p} = \left(Q_{11}^{i,p} + Q_{22}^{i,p} - 2(Q_{66}^{i,p} + Q_{12}^{i,p})\right)\cos^2\theta^{i,p}\sin^2\theta^{i,p} + Q_{66}^{i,p}\left(\sin^4\theta^{i,p} + \cos^4\theta^{i,p}\right) \tag{89}$$

The individual A, B, and D matrices can be calculated according to Equations 8-10, in which, the values of Z_k are dependent upon the layer thicknesses. These Equations were presented in Chapter 1 and repeated here.

$$A_{ij} = \sum_{i=k}^{N} \bar{Q}_{ij}^{k}(z_k - z_{k-1}) \tag{8}$$

$$B_{ij} = \frac{1}{2}\sum_{i=k}^{N} \bar{Q}_{ij}^{k}(z_k^2 - z_{k-1}^2) \tag{9}$$

$$D_{ij} = \frac{1}{3}\sum_{i=k}^{N} \bar{Q}_{ij}^{k}(z_k^3 - z_{k-1}^3) \tag{10}$$

The calculated matrices can then be assembled into the constitutive equations presented in Chapter 1 by Equations 7 and 13 and repeated here.

$$\begin{bmatrix}\{N\}\\ \{M\}\end{bmatrix} = \begin{bmatrix}[A] & [B]\\ [B] & [D]\end{bmatrix}\begin{bmatrix}\{\varepsilon^0\}\\ \{\varepsilon^1\}\end{bmatrix} \tag{7}$$

$$\begin{Bmatrix}Q_y\\ Q_x\end{Bmatrix} = K\begin{bmatrix}A_{44} & A_{45}\\ A_{45} & A_{55}\end{bmatrix}\begin{Bmatrix}\frac{\partial \omega_o}{\partial y} + \phi_y\\ \frac{\partial \omega_o}{\partial x} + \phi_x\end{Bmatrix} \tag{13}$$

6.3 Critical Loads

This section outlines the calculation of stresses that lead to buckling and shear deformation of green composite laminates.

6.3.1 Buckling Equations

For a chord and span wrinkle, Figure 3, the boundary conditions for buckling will change. The boundary conditions of a span wrinkle formed parallel to the spar axis would be fixed at the web and free at the end of the flange. Its length would be equivalent to the flange length. Boundary conditions for chord wrinkles, formed perpendicular to the spar axis, are free – free. Its length would be the length of the laminate.

Section 1.2.3 describes the general approach for determining the buckling equations. For the classical laminated plate theory (CLPT), these equations often reduce to discrete one-dimensional problems depending upon the D matrix. The FSDT equations are dependent upon the D and A matrix, and several boundary conditions diverge to a non-linear solution often needing a numerical method to solve the equation. In the following sections, the equations for beam buckling and plate buckling will be presented for both CLPT and FSDT theories.

6.3.1.1 Classical Laminated Plate Theory

The general equation for laminated beam buckling derived by the CLPT method is provided by Equation 90.

$$N_c = \frac{\lambda^2}{D_{11}'} \tag{90}$$

In Equation 90, λ is determined from the boundary conditions, and $D_{11}^{'}$ is from the inverse of the ABD matrix. In the case where B=0, $D_{11}^{'}$ simply becomes the inverse of D_{11}. Applying the boundary conditions to Equation 17, the solution of the 4th order differential equation of motion, and solving for the non-trivial solution yields the λ's provided in Table 32 which states that 'a' is the length of the beam corresponding to the wrinkle type being investigated.

Table 32: Solutions of λ for CLPT Laminated Beam Buckling

Boundary Condition	$\boldsymbol{\lambda}$
Free-Free	π/a
Fixed-Free	π/(2a)

The buckling of a laminated plate uses a different solution to the equation of motion than the laminated beam buckling. This general solution takes the form of Equation 91.

$$w(x,y) = W_{nm}\cos(\alpha x)\sin(\beta y) \tag{91}$$

$$\alpha = \frac{m\pi}{a} \tag{92}$$

$$\beta = \frac{n\pi}{b} \tag{93}$$

The non-trivial solution ($W_{nm} \neq 0$) then yields the critical buckling stress for any boundary conditions that satisfy Equation 91. In order to produce the lowest critical buckling stress, the optimal combination of m and n need to be determined for each laminate.

$$N_c = \frac{D_{11}\alpha^4 + 2(D_{12}+2D_{66})\alpha^2\beta^2 + D_{22}\beta^4}{\alpha^2 + k\beta^2} \tag{94}$$

$$k = \frac{N_{yy}}{N_{xx}} = \frac{A_{22}}{A_{12}} \tag{95}$$

6.3.1.2 First-Order Shear Displacement Theory

The general equation for laminated beam buckling derived by the FSDT is provided by Equation 96 in which, λ is again determined from applying boundary conditions to the solutions to the equation of motion.

$$N_c = \frac{\lambda^2}{D'_{11}\left(1 + \frac{\lambda^2}{KD'_{11}G_{xz}h}\right)} \tag{96}$$

$$G_{xz} = \frac{1}{A'_{55}h} \tag{97}$$

In addition to Equation 17, an additional equation (98) is needed to depict the twist of the laminate**.** Applying the boundary conditions and solving for the non-trivial solution results in the λ's provided in Table 33 in which, 'a' is the length of the beam corresponding to the wrinkle type being investigated.

$$\chi(x) = \frac{1}{\left(1 + \frac{\lambda^2}{KD'_{11}G_{xz}h}\right)}\frac{dW}{dx} - c_3\frac{N_{xx}}{KG_{xz}h} \tag{98}$$

Table 33: Solutions of λ for FSDT Laminated Beam Buckling

Boundary Condition	$\boldsymbol{\lambda}$
Free-Free	π/a
Fixed-Free	π/(2a)

Buckling of a FSDT laminated plate has a combination of additional A, B, and D terms to that of the CLPT laminated plate buckling equation. But for the specific case of a symmetric laminate (B=0), the FSDT plate theory reduces to Equation 94.

6.3.2 Critical Shear Stress

Order of magnitude differences in the elastic modulus exist between the prepreg layers and interface layers of a green laminate. In the case of green shearing during forming, only the interface layers shear; thus, prepreg layers are inextensible during forming operations and do not contribute to the critical shear stress. A new ABD matrix (ABD^i) will be calculated using only the $\bar{Q}_{ij}^i$ terms or setting $\bar{Q}_{ij}^p = 0$.

The critical shear strain for slip to occur must be experimentally determined for each prepreg system, which is Equation 73 for Cycom 970 PW system. The total strain that a laminate needs to experience before inter-laminar shearing occurs is defined by Γ in Equation 99 where k^i is the total interface layers defined in Equation 75.

$$\Gamma = \gamma_c k^i \tag{99}$$

Assuming the x-axis is aligned with the principle material axis (span), the constitutive equation for green composite slip can be derived from Equation 7. For symmetric laminates where B=0, the equations are decoupled reducing the constitutive equation to Equation 100.

$$\begin{bmatrix} N_{xx}^{\Gamma} \\ N_{yy}^{\Gamma} \\ N_{xy}^{\Gamma} \end{bmatrix} = \begin{bmatrix} A_{11}^i & A_{12}^i & A_{16}^i \\ A_{12}^i & A_{22}^i & A_{26}^i \\ A_{16}^i & A_{26}^i & A_{66}^i \end{bmatrix} \begin{bmatrix} 0 \\ \Gamma \\ 0 \end{bmatrix} \tag{100}$$

Wrinkling will occur if the critical shear stress N_{xx}^{Γ} or N_{yy}^{Γ} is greater than the critical buckling stress N_c.

6.5 Model Validation

This section verifies the wrinkling model defined in sections 6.1 through 6.4 against the experimental hot drape forming presented in section 5.6.2.

6.5.1 Material Properties

The prepreg properties — E, G, and υ — were acquired from Cytec and used in the verification. These properties are as follows: $E^p = 58e9$ Pa, $G^p = 5e9$ Pa, $\upsilon^p = 0.1$, with ply thickness of 0.0216 mm. The resin interface properties were determined using Equations 73, 74, and 77-79. In Equations 77 and 78, the bulk modulus is a required input. Smith et. al. [114], shows bulk modulus of an epoxy resin to be 5.5 GPa. A similar bulk modulus was utilized for this work. Additionally, G_{debulk} was calculated to be 2e6 Pa from Table 9. Defining $\vec{x}$ parallel to the length of the composite laminate and $\vec{y}$ parallel to the width, a=0.9652 m and b= 0.08572 m. The laminate layups used are shown in Table 34.

Table 34: Laminate Stacking Sequence

Ply Count	Stacking Sequence
30	$[\pm45,0/90, \pm45,0/90, \pm45,0/90, \pm45,0/90, \pm45,0/90, \pm45,0/90, \pm45,0/90, \pm45]_s$
18	$[\pm45,0/90, \pm45,0/90, \pm45,0/90, \pm45,0/90, \pm45]_s$
10	$[\pm45,0/90, \pm45,0/90, \pm45]_s$

6.5.2 Model Results

Using the Matlab® code provided in Appendix D, the buckling and shearing stresses were determined for various Hersey numbers and the three different laminates outlined in Table 34. Results in section 6.5.2.1 show that for lower slenderness ratios (b/h), the buckling will

follow laminated beam buckling. For higher slenderness ratios, the laminate will buckle via laminated plate buckling.

The chord wrinkles of the 30-ply laminate are modeled very closely using the FSDT green laminate model. Based upon the verification experiments, the FSDT green laminate model predicts the wrinkle development accurately based upon the inter-laminar shearing characteristics and verification experiments, thus confirming Hypothesis 5.

6.5.2.1 Laminate Thickness Variation

The critical buckling and shearing stresses along the spar's x axis are provided in Table 35 for the standard-twist 10-, 18-, and 30-ply laminates. The critical buckling stresses are presented for both the FSDT and CLPT represented by N_f and N_c, respectively. The boundary conditions FF, free-free, and FC, free-clamped, are also denoted for each theory.

Table 35: Critical Stresses for Chord Wrinkles in Laminates of Various Thicknesses

	Hersey Number	**2.4924**	**0.9235**	**0.3674**	**0.0993**	**0.0596**	**0.0397**
30	**Nxx (Pa)**	1.95E+06	1.26E+06	8.41E+05	4.73E+05	3.78E+05	3.16E+05
	Nyy (Pa)	2.00E+06	1.29E+06	8.61E+05	4.84E+05	3.87E+05	3.24E+05
	Nf_FF (Pa)	5.22E+05	6.28E+05	7.36E+05	9.00E+05	9.66E+05	1.02E+06
	Nc_FF (Pa)	1.50E+04	1.50E+04	1.50E+04	1.50E+04	1.50E+04	1.50E+04
	N_plate (Pa)	2.29E+06	2.29E+06	2.29E+06	2.29E+06	2.29E+06	2.29E+06
	Hersey Number	**1.4955**	**0.5541**	**0.2205**	**0.0596**	**0.0357**	**0.0238**
18	**Nxx (Pa)**	5.32E+05	3.43E+05	2.29E+05	1.29E+05	1.03E+05	8.60E+04
	Nyy (Pa)	5.53E+05	3.57E+05	2.38E+05	1.34E+05	1.07E+05	8.95E+04
	Nf_FF (Pa)	3.80E+04	4.36E+04	4.87E+04	5.58E+04	5.84E+04	6.04E+04
	Nc_FF (Pa)	3.13E+03	3.13E+03	3.13E+03	3.13E+03	3.13E+03	3.13E+03
	N_plate (Pa)	4.94E+05	4.94E+05	4.94E+05	4.94E+05	4.94E+05	4.94E+05
	Hersey Number	**0.8308**	**0.3078**	**0.1225**	**0.0331**	**0.0199**	**0.0132**
10	**Nxx (Pa)**	1.13E+05	7.30E+04	4.86E+04	2.74E+04	2.18E+04	1.83E+04
	Nyy (Pa)	1.22E+05	7.86E+04	5.24E+04	2.94E+04	2.35E+04	1.97E+04
	Nf_FF (Pa)	1.81E+03	1.94E+03	2.04E+03	2.17E+03	2.22E+03	2.25E+03
	Nc_FF (Pa)	4.96E+02	4.96E+02	4.96E+02	4.96E+02	4.96E+02	4.96E+02

N_plate (Pa)	8.50E+04	8.50E+04	8.50E+04	8.50E+04	8.50E+04	8.50E+04

By plotting the intersection of the buckling stress and shearing stress curves for each slenderness ratio, the instability limit of the material can be determined. At Hersey numbers below the instability limit no wrinkling is predicted while Hersey numbers above the limit are predicted to wrinkle. Figure 56 provides the tested conditions for the 30-, 18, and 10-ply laminates and also the experimental wrinkled response of the standard-twist verification. The flange slenderness ratio, b/h, is calculated for each tested laminate and are provided in Table 36. The limiting slenderness ratio (b/h) defines the transition from a slender column or plate to a non-slender column or beam. For these uncured laminates, this transition occurs when the slenderness ratio is equal to 23 defined in Equation 101. At slenderness ratios below 23 the laminate will buckle according to beam theory, while at slenderness ratios greater or equal to 23 the laminate will buckling according to plate theory.

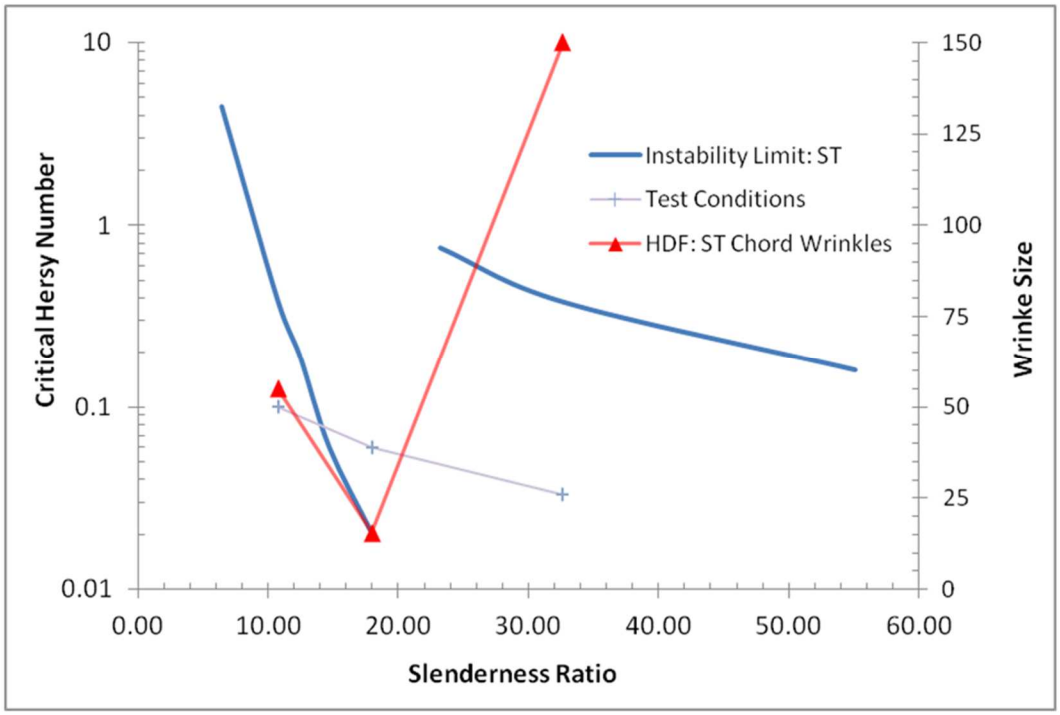

Figure 56: FSDT Slenderness Ratio Verification

Table 36: Slenderness Ratios of Standard-Twisted Laminates

Ply Count	Slenderness Ratio (b/h)
30	11
18	18
10	33

$$N_c = \begin{cases} FSDT\ Beam, & b/h < 23 \\ FSDT\ Plate, & b/h \geq 23 \end{cases} \tag{101}$$

In all laminates, the CLPT theory predicts that wrinkling should occur at each Hersey number. This does not reflect the results from experimental tests presented in Table 30 indicating that the CLPT green laminate model does not represent the wrinkling states of the beams. The FDST beam theory represents the slight wrinkling in the 30-ply laminate and large wrinkles in 18-ply laminate but does not represent the wrinkle-free scenario of the 10-ply laminate. The plate theory does, however, represent the wrinkle-free case of the 10-ply laminate. These experimental results correspond well with the transition from a non-slender column to a slender column shown in Figure 56. The 18-ply laminate was formed at a Hersey number greater than the instability limit and was expected to wrinkle while the 30-ply laminate and the 10-ply laminate were expected not to wrinkle according to the beam and plate theory, respectively.

6.5.2.2 30 Ply Laminate Verification

The critical buckling and shearing stresses are provided in Table 37 for never-twisted and standard-twist fibers for the 30-ply laminate. For both never-twisted and standard-twist fibers, the critical buckling stresses are presented for the first order shear deformation theory and the classical laminated plate theory. The boundary conditions FF, free-free, and FC, free-clamped, are also denoted.

The laminated plate buckling predicts that no wrinkles — neither chord nor span— will form for standard-twist fibers and at Hersey numbers less than 2.49 for never-twisted prepregs. The CLPT beam predicts that all Hersey numbers will initiate all types of wrinkles. Neither accurately represents the wrinkling observed in the hot drape forming trials (5.6). The addition of the transverse shear strains in the FSDT theory provides a more accurate representation of wrinkling in green laminates. The FSDT theory predicts that chord wrinkles will occur in both fiber twists and that no span wrinkles will occur. No span wrinkles occurred in the experimental data validating this prediction.

Table 37: Critical Buckling and Shear Stresses for ST and NT Fibers of 30 Ply Laminate

	Hersey Number	**2.4924**	**0.92349**	**0.36741**	**0.0993**	**0.05958**	**0.03972**
ST Fibers	**N^{Γ}_{xx} (Pa)**	1.95E+06	1.26E+06	8.41E+05	4.73E+05	3.78E+05	3.16E+05
	N^{Γ}_{yy} (Pa)	2.00E+06	1.29E+06	8.61E+05	4.84E+05	3.87E+05	3.24E+05
	N_f_FF (Pa)	5.22E+05	6.28E+05	7.36E+05	9.00E+05	9.66E+05	1.02E+06
	N_f_FC (Pa)	5.09E+08	6.16E+08	7.24E+08	8.89E+08	9.55E+08	1.01E+09
	N_c_FC (Pa)	4.75E+05	4.75E+05	4.75E+05	4.75E+05	4.75E+05	4.75E+05
	N_c_FF (Pa)	1.50E+04	1.50E+04	1.50E+04	1.50E+04	1.50E+04	1.50E+04
	N_plate (Pa)	2.29E+06	2.29E+06	2.29E+06	2.29E+06	2.29E+06	2.29E+06
NT Fiber	**N^{Γ}_{xx} (Pa)**	2.38E+06	1.39E+06	8.46E+05	4.17E+05	3.17E+05	2.54E+05
	N^{Γ}_{yy} (Pa)	2.43E+06	1.42E+06	8.65E+05	4.27E+05	3.24E+05	2.60E+05
	N_f_FF (Pa)	5.89E+05	7.66E+05	9.44E+05	1.20E+06	1.29E+06	1.36E+06
	N_f_FC (Pa)	5.77E+08	7.55E+08	9.33E+08	1.19E+09	1.28E+09	1.35E+09
	N_c_FC (Pa)	4.75E+05	4.75E+05	4.75E+05	4.75E+05	4.75E+05	4.75E+05
	N_c_FF (Pa)	1.50E+04	1.50E+04	1.50E+04	1.50E+04	1.50E+04	1.50E+04
	N_plate (Pa)	2.28E+06	2.28E+06	2.28E+06	2.28E+06	2.28E+06	2.28E+06

The theory also accurately depicts the formation of chord wrinkles at the various tested Hersey numbers. Figure 57 shows the verification of the wrinkle model versus the hot drape formed chord wrinkles. The never twist's critical shear stress, NT:N^{Γ}_{xx}, intersects with the FSDT critical buckling stress, NT:N_f_FF, at H_i=0.42 while the standard twist's critical shear stress, ST:N^{Γ}_{xx}, intersects with the FSDT critical buckling stress, ST:N_f_FF, at H_i=0.3. At Hersey

numbers below this critical value, the critical shear stress is lower than the critical buckling stress; thus, the laminate will shear and not wrinkle. While at Hersey numbers greater than the critical Hersey number, the buckling stress is lower than the critical shear stress; thus, the laminate will wrinkle.

This corresponds well to the experimental wrinkled spars. The never-twisted spars produced a non-wrinkled state at H≤0.37 which falls into the wrinkle-free zone predicted from the model. The standard-twisted material is wrinkle free at H≤0.06. The spar formed at H=0.1 had very slight wrinkles (L/D=55) while the model predicts that the standard-twist spars are wrinkle free at H<0.3. While this does not perfectly represent the two replicate spars formed at H=0.1, the trend of the data shows an inflection point between the tests at H=0.37 and H=0.1 which corresponds to the critical Hersey number of H≤0.3.

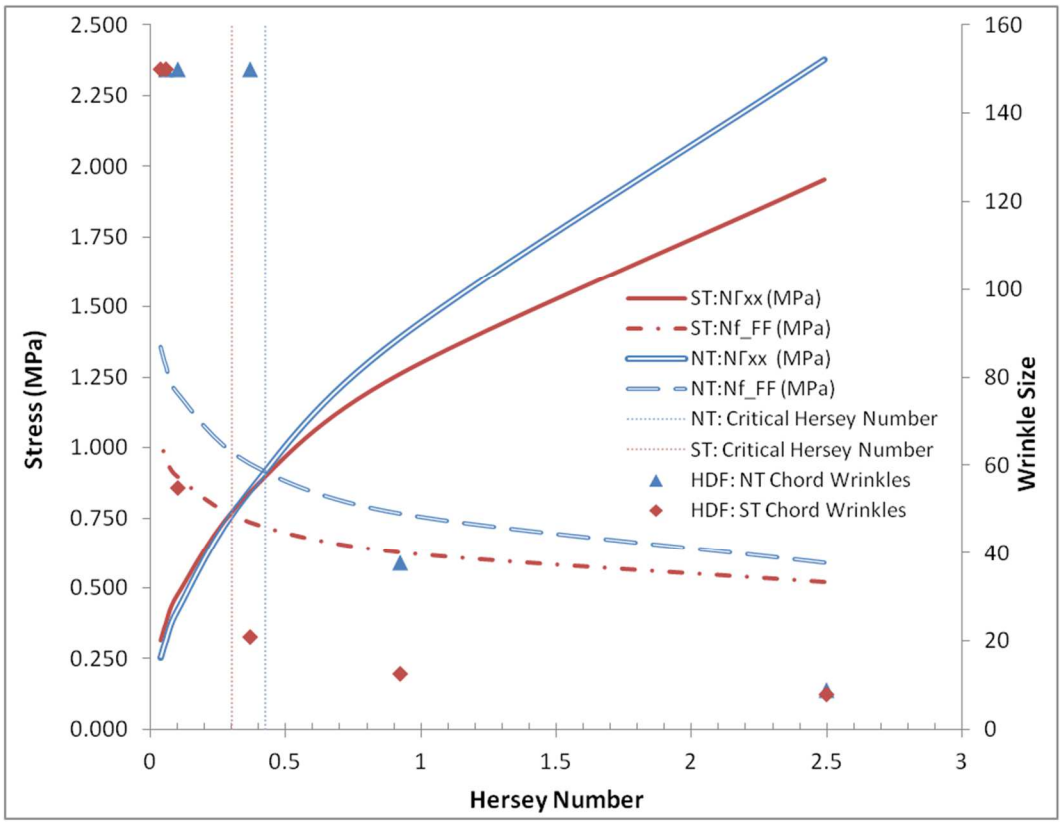

Figure 57: FSDT Chord Wrinkle Model Validation

Off-angle wrinkles did occur in the standard-twist and never-twist tests at 22 °C (H=2.51) which is not predicted via the N_f_FF beam, N_f_FC beam, nor plate models. These wrinkles are highly dependent upon the joggle and only form in the joggled regions. If an effective length, proportional to the length of the joggle (a=0.734 m, b/h=11), is used for buckling length and applying boundary conditions of a pinned-pinned or simply supported beam ($\lambda = \frac{\pi}{a}$) to the edges of the section, the model predicts the off-angle wrinkles to occur at 22 °C as shown in Figure 58.

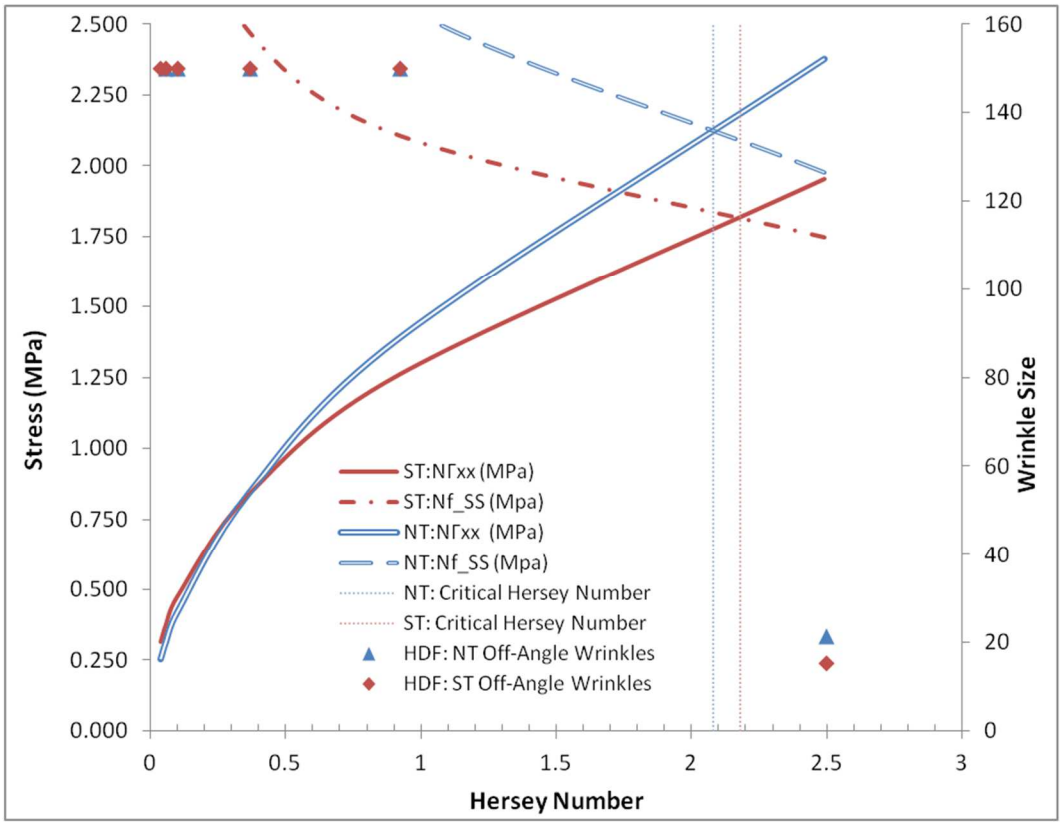

Figure 58: FSDT Off-Angle Model Verification

6.5.3 Applications of Green Wrinkle Model

The FSDT green laminate model predicts the wrinkle development accurately based upon the inter-laminar shearing characteristics performed on the prepregs. Thus Hypothesis 5 is accepted demonstrating that the green wrinkling behavior can be modeled using laminated plate

theories. A more accurate model can be produced by incorporating the prepreg bending and intra-laminar shearing behavior to the model but was out of scope for this work.

This low-fidelity model can be utilized as a screening aid to determine process parameters for composite forming processes. Characterization of the prepreg inter-laminar shearing would be required to utilize this model but the amount of material needed to characterize the prepreg input variables is considerably less than would be utilized performing forming trials to heuristically determine the optimal forming temperature. One limitation of the model is that this model has been validated with continuous-thickness laminates. In traditional composite c-channels, the laminate thickness is reduced outside of the joggle region to reduce the weight of a component. It is theorized that the model would hold if an effective length could be utilized for the spar; similar to that of the off-angle wrinkles in section 5.6.2.2.

CHAPTER 7 – CONCLUSIONS

This work primarily investigated the influence of how material properties affect the wrinkling behavior of a composite laminate. Several factors affecting composite ply forming were identified from literature. These were inter-laminar shearing, ply bending, material tack, and intra-laminar effects. A series of experimental tests were conducted with uni-directional tapes (UD), plain weaves (PW), and eight harness satin (8HS) prepregs which showed that intra-laminar shearing was a factor in the wrinkling. Then the PW prepreg was selected to fully characterize, and two variations of Cycom 970's PW prepreg were analyzed for tack, intra-laminar shearing, and inter-laminar shearing. Additionally, a low fidelity model was derived based upon the first-order shear displacement theory. Verification of the model was conducted via experimental hot drape forming of laminates using various Hersey numbers. Through the course of this project, five hypotheses were investigated and are outlined herein.

The first hypothesis was that the tack grade of a prepreg would not affect the inter-laminar friction at temperatures above room temperature. Results showed that varying the tack grade did not influence out-of-plane wrinkling at elevated temperatures. Two different tack grades— Cycom 970 high tack and low tack— were tested at various temperatures and strain rates. It was determined that the two tack grades were statistically equivalent and, thus, do not affect the forming of the prepregs, thus, confirming Hypothesis 1. However, the tack tests did show the transition of the resin from inter-facial failure to cohesive failures. This transition represents the point at which the resin starts to flow and, thus, composite forming operations should be conducted at temperatures above this transition temperature.

The second hypothesis was that fiber twist would play a major factor in inter-laminar shearing. Thus, by eliminating fiber twist, the inter-laminar shear would decrease which would

reduce out-of-plane wrinkling compared to c-channels of twisted fibers. Two twist types were acquired using a Cycom 970 PW prepreg: standard twist and never twist. Characterization of the inter-laminar shearing was conducted at various combinations of resin viscosity, strain rate, and normal pressures. The dimensionless constant Hersey number correlates the three tested variables. Results showed that the twist type was a significant variable in both the shear stress equation and critical strain equations. Both equations possessed variables of Hersey number and normal pressure and contained material-specific coefficients fitted from the experimental data. The never-twisted material had higher shear toughness compared to the standard-twisted material. Thus, the never-twisted material would absorb more energy before slip occurs. This was confirmed with experimental drape forming showing that the standard-twist material had wrinkles at lower Hersey numbers than the never-twisted material, thus, confirming Hypothesis 2.

The third hypothesis was that the drapability of a ply in a laminate would not be affected by inter-laminar effects. Thus 8HS laminates, which show improved ply drapability over PW plies and tapes plies, would produce fewer wrinkles than similar tape or PW laminates. Drape forming trials were conducted with Cycom 5320-1 prepregs of UD, PW, and 8HS equivalent laminates. The 8HS laminate formed without wrinkles while the PW laminate had smaller wrinkles than the tape laminate, thus, confirming Hypothesis 3.

The forth hypothesis was that forming charges at lower resin viscosities would reduce out-of-plane wrinkle development and that an optimum resin viscosity could be shown to exist for forming processes. Experimental drape forming trials were conducted at various forming temperatures on a 30 ply balanced and symmetric laminate using Cycom 970 standard-twist and never-twist prepregs. The results showed that the differences in wrinkle development between

the two laminates were caused by the inter-laminar shearing differences. The never-twisted prepreg laminates produced a wrinkle-free spar at Hersey numbers ≤0.37 while the standard-twist laminates produced a wrinkle free spar at Hersey numbers ≤0.1. While the resin viscosity is a direct variable in the Hersey number, the results showed that the viscosity was not the only variable influencing the wrinkle development. In addition to the viscosity, the shear rate and the initial pressure also affected the wrinkle development, thus, negating Hypothesis 4 which considered viscosity alone rather than as part of a combination of influential variables.

The final hypothesis was that a correlation could be shown to exist between wrinkle development and inter-laminar shearing and that it could be modeled using composite plate theories. The first-order shear displacement theory was adapted for use with uncured prepregs. From the stacking sequence of the laminate, interfacial layers were added between the plies representing the resin joint. The properties of these layers were characterized from the inter-laminar shearing characterization completed as part of this project. The model then considered the failure mechanism between inter-laminar shearing and out-of-plane wrinkling. Validating the model against the experimental hot drape forming data shows good correlation between modeled wrinkle predictions and the experimental wrinkle results, thus confirming Hypothesis 5.

In summary, this project advanced the understanding of how uncured material properties influence composite forming process. A low-fidelity-first-principle model was developed and the necessary characterization steps to determine the model's input prepregs properties were also presented.

Improvements upon the work presented herein can further investigate the different prepreg forms of uni-directional tapes and harness weaves to fully develop the FSDT prepreg model. This low fidelity model works well for design and process engineers to determine part

stacking sequence or the part family's forming parameters but it does little to fully characterize the size of a formed wrinkle. A better representation of the wrinkle formation could be achieved by incorporating this model into a finite element based solution. This higher fidelity model would enable an accurate depiction of wrinkle formation and formed size. The FEA simulation of wrinkle formation would allow for a more robust process evaluation and an iterative process optimization. Composite part manufactures would greatly benefit from this higher fidelity model to evaluate and optimize composite forming processes and part designs.

REFERENCES

[1] Hallander P, Akermo M, Mattei C, Petersson M, Nyman T. An experimental study of mechanisms behind wrinkle development during forming of composite laminates. Compos Part A Appl Sci Manuf 2013;50:54–64. doi:10.1016/j.compositesa.2013.03.013.

[2] Laminating Technology. Boeing_HDF. Hot Drape Former 2010. http://www.laminatingtechnology.com/images/Boeing_HDF.jpg (accessed January 1, 2016).

[3] Hallander P, Sjölander J, Åkermo M. Forming induced wrinkling of composite laminates with mixed ply material properties; an experimental study. Compos Part A Appl Sci Manuf 2015;78:234–45. doi:10.1016/j.compositesa.2015.08.025.

[4] Reddy JN. Mechanics of Laminated Composite Plates and Shells: Theory and Analysis, Second Edition. Taylor & Francis; 2004.

[5] Munson BR, Young DF, Okiishi TH. Fundamentals of Fluid Mechanics. 6th ed. Fowley, Don; 2009.

[6] Robinson JW, Zhou Y, Bhattacharya P, Erck R, Qu J, Bays JT, et al. Probing the molecular design of hyper-branched aryl polyesters towards lubricant applications. Sci Rep 2016;6:18624. doi:10.1038/srep18624.

[7] Woo K, Whitcomb JD. Effects of fiber tow misalignment on the engineering properties of plain weave textile composites. Compos Struct 1997;37:343–55.

[8] Liu D, Fleck NA, Sutcliffe MPF. Compressive strength of fibre composites with random fibre waviness. J Mech Phys Solids 2004;52:1481–505.

[9] Desplentere F, Lomov S V., Woerdeman DL, Verpoest I, Wevers M, Bogdanovich A. Micro-CT characterization of variability in 3D textile architecture. Compos Sci Technol 2005;65:1920–30. doi:10.1016/j.compscitech.2005.04.008.

[10] Abdiwi F, Harrison P, Koyama I, Yu WR, Long AC, Corriea N, et al. Characterising and modelling variability of tow orientation in engineering fabrics and textile composites. Compos Sci Technol 2012;72:1034–41. doi:10.1016/j.compscitech.2012.03.017.

[11] Wisnom MR, Gigliotti M, Ersoy N, Campbell M, Potter KD. Mechanisms generating residual stresses and distortion during manufacture of polymer–matrix composite structures. Compos Part A Appl Sci Manuf 2006;37:522–9.

[12] Radford DW, Rennick TS. Separating sources of manufacturing distortion in laminated composites. J Reinf Plast Compos 2000;19:621–41.

[13] Fernlund G, Rahman N, Courdji R, Bresslauer M, Poursartip A, Willden K, et al. Experimental and numerical study of the effect of cure cycle, tool surface, geometry, and lay-up on the dimensional fidelity of autoclave-processed composite parts. Compos Part A Appl Sci Manuf 2002;33:341–51.

[14] Albert C, Fernlund G. Spring-in and warpage of angled composite laminates. Compos Sci Technol 2002;62:1895–912.

[15] Cinar K, Ersoy N. Effect of fibre wrinkling to the spring-in behaviour of L-shaped composite materials. Compos Part A Appl Sci Manuf 2015;69:105–14. doi:10.1016/j.compositesa.2014.10.025.

[16] Leong M, Overgaard LCT, Thomsen OT, Lund E, Daniel IM. Investigation of failure mechanisms in GFRP sandwich structures with face sheet wrinkle defects used for wind turbine blades. Compos Struct 2012;94:768–78.

[17] Wang J, Potter KD, Hazra K, Wisnom MR. Experimental fabrication and characterization

of out-of-plane fibre waviness in continuous fibre-reinforced composites. J Compos Mater 2011:21998311429877.
[18] Mukhopadhyay S, Jones MI, Hallett SR. Tensile failure of laminates containing an embedded wrinkle; numerical and experimental study. Compos Part A Appl Sci Manuf 2015;77:219–28.
[19] El-Hajjar RF, Petersen DR. Gaussian function characterization of unnotched tension behavior in a carbon/epoxy composite containing localized fiber waviness. Compos Struct 2011;93:2400–8.
[20] Bloom LD, Wang J, Potter KD. Damage progression and defect sensitivity: an experimental study of representative wrinkles in tension. Compos Part B Eng 2013;45:449–58.
[21] Mukhopadhyay S, Jones MI, Hallett SR. Compressive failure of laminates containing an embedded wrinkle; Experimental and numerical study. Compos Part A Appl Sci Manuf 2015;73:132–42. doi:10.1016/j.compositesa.2015.03.012.
[22] Adams DO, Hyer MW. Effects of layer waviness on the compression strength of thermoplastic composite laminates. J Reinf Plast Compos 1993;12:414–29.
[23] Bradley DJ, Adams DO, Gascoigne HE. Interlaminar strains and compressive strength reductions due to nested layer waviness in composite laminates. J Reinf Plast Compos 1998;17:989–1011.
[24] Lemanski SL, Wang J, Sutcliffe MPF, Potter KD, Wisnom MR. Modelling failure of composite specimens with defects under compression loading. Compos Part A Appl Sci Manuf 2013;48:26–36.
[25] Makeev A, Seon G, Lee E. Failure predictions for carbon/epoxy tape laminates with wavy plies. J Compos Mater 2009.
[26] Potter K, Khan B, Wisnom M, Bell T, Stevens J. Variability, fibre waviness and misalignment in the determination of the properties of composite materials and structures. Compos Part A Appl Sci Manuf 2008;39:1343–54.
[27] Prodromou a. G, Chen J. On the relationship between shear angle and wrinkling of textile composite preforms. Compos Part A Appl Sci Manuf 1997;28:491–503. doi:10.1016/S1359-835X(96)00150-9.
[28] Harrison P, Abdiwi F, Guo Z, Potluri P, Yu WR. Characterising the shear-tension coupling and wrinkling behaviour of woven engineering fabrics. Compos Part A Appl Sci Manuf 2012;43:903–14. doi:10.1016/j.compositesa.2012.01.024.
[29] Tam AS, Gutowski TG. The kinematics for forming ideal aligned fibre composites into complex shapes. Compos Manuf 1990;1:219–28. doi:10.1016/0956-7143(90)90044-W.
[30] Gereke T, Döbrich O, Hübner M, Cherif C. Experimental and computational composite textile reinforcement forming: A review. Compos Part A Appl Sci Manuf 2013;46:1–10. doi:10.1016/j.compositesa.2012.10.004.
[31] Jenny ZY, Cai Z, Ko FK. Formability of textile preforms for composite applications. Part 1: Characterization experiments. Compos Manuf 1994;5:113–22.
[32] Lightfoot JS, Wisnom MR, Potter K. A new mechanism for the formation of ply wrinkles due to shear between plies. Compos Part A Appl Sci Manuf 2013;49:139–47. doi:10.1016/j.compositesa.2013.03.002.
[33] Twigg G, Poursartip A, Fernlund G. An experimental method for quantifying tool–part shear interaction during composites processing. Compos Sci Technol 2003;63:1985–2002.
[34] Potter KD, Campbell M, Langer C, Wisnom MR. The generation of geometrical

deformations due to tool/part interaction in the manufacture of composite components. Compos Part A Appl Sci Manuf 2005;36:301–8.
[35] Ersoy N, Garstka T, Potter K, Wisnom MR, Porter D, Clegg M, et al. Development of the properties of a carbon fibre reinforced thermosetting composite through cure. Compos Part A Appl Sci Manuf 2010;41:401–9.
[36] Ersoy N, Potter K, Wisnom MR, Clegg MJ. An experimental method to study the frictional processes during composites manufacturing. Compos Part A Appl Sci Manuf 2005;36:1536–44.
[37] Harrison P. Modelling the forming mechanics of engineering fabrics using a mutually constrained pantographic beam and membrane mesh. Compos Part A Appl Sci Manuf 2016;81:145–57. doi:10.1016/j.compositesa.2015.11.005.
[38] De Bilbao E, Soulat D, Hivet G, Gasser A. Experimental study of bending behaviour of reinforcements. Exp Mech 2010;50:333–51.
[39] Bilisik K, Yolacan G. Experimental determination of bending behavior of multilayered and multidirectionally-stitched E-Glass fabric structures for composites. Text Res J 2012;82:1038–49.
[40] Kawahabat A. The Standardization and Analysis of Hand Evaluation 2001.
[41] Lomov SV, Verpoest I, Barburski M, Laperre J. Carbon composites based on multiaxial multiply stitched preforms. Part 2. KES-F characterisation of the deformability of the preforms at low loads. Compos Part A Appl Sci Manuf 2003;34:359–70.
[42] Dodwell TJ, Erland S, Butler R, Down C, Continuum C, Defects W, et al. a Cosserat Continuum Model for Uncured Composite Laminates With Applications To Ply Wrinkle Formation. Iccm20 2015:19–24.
[43] Dodwell TJ. Internal buckling instabilities in layered media. Philos Mag Across Scales IV Accept 2015.
[44] Standard B. Textiles—test methods for nonwovens—Part 7: Determination of bending length. BS EN ISO 1998:9073–7.
[45] Hancock SG, Potter KD. The use of kinematic drape modelling to inform the hand lay-up of complex composite components using woven reinforcements. Compos Part A Appl Sci Manuf 2006;37:413–22.
[46] Sidhu R, Averill RC, Riaz M, Pourboghrat F. Finite element analysis of textile composite preform stamping. Compos Struct 2001;52:483–97.
[47] Harrison P, Yu W-R, Long AC. Rate dependent modelling of the forming behaviour of viscous textile composites. Compos Part A Appl Sci Manuf 2011;42:1719–26.
[48] Skordos AA, Monroy Aceves C, Sutcliffe MPF. A simplified rate dependent model of forming and wrinkling of pre-impregnated woven composites. Compos Part A Appl Sci Manuf 2007;38:1318–30. doi:10.1016/j.compositesa.2006.11.005.
[49] Harrison P, Abdiwi F, Guo Z, Potluri P, Yu WR. Characterising the shear–tension coupling and wrinkling behaviour of woven engineering fabrics. Compos Part A Appl Sci Manuf 2012;43:903–14.
[50] Launay J, Hivet G, Duong A V., Boisse P. Experimental analysis of the influence of tensions on in plane shear behaviour of woven composite reinforcements. Compos Sci Technol 2008;68:506–15. doi:10.1016/j.compscitech.2007.06.021.
[51] Cao J, Akkerman R, Boisse P, Chen J, Cheng HS, de Graaf EF, et al. Characterization of mechanical behavior of woven fabrics: Experimental methods and benchmark results. Compos Part A Appl Sci Manuf 2008;39:1037–53.

doi:10.1016/j.compositesa.2008.02.016.
[52] Haanappel SP, Ten Thije RHW, Sachs U, Rietman B, Akkerman R. Formability analyses of uni-directional and textile reinforced thermoplastics. Compos Part A Appl Sci Manuf 2014;56:80–92. doi:10.1016/j.compositesa.2013.09.009.
[53] ten Thije RHW, Akkerman R. Solutions to intra-ply shear locking in finite element analyses of fibre reinforced materials. Compos Part A Appl Sci Manuf 2008;39:1167–76. doi:10.1016/j.compositesa.2008.03.014.
[54] Sharma SB, Sutcliffe MPF, Chang SH. Characterisation of material properties for draping of dry woven composite material. Compos Part A Appl Sci Manuf 2003;34:1167–75. doi:10.1016/j.compositesa.2003.09.001.
[55] Mohammed U, Lekakou C, Dong L, Bader MG. Shear deformation and micromechanics of woven fabrics. Compos Part A Appl Sci Manuf 2000;31:299–308. doi:10.1016/S1359-835X(99)00081-0.
[56] Wang J, Page JR, Paton R. Experimental investigation of the draping properties of reinforcement fabrics. Compos Sci Technol 1998;58:229–37. doi:10.1016/S0266-3538(97)00115-2.
[57] Larberg YR, Åkermo M, Norrby M. On the deformability of different generations of cross-plied unidirectional prepreg. J Compos Mater 2011;46:929–39. doi:10.1177/0021998311412988.
[58] Pandey RK, Sun CT. Mechanisms of wrinkle formation during the processing of composite laminates. Compos Sci Technol 1999;59:405–17. doi:10.1016/S0266-3538(98)00080-3.
[59] Erland S, Dodwell TJ, Butler R. Inter and intra-ply shearing of uncured carbon fibre laminates. Eur Conf Compos Mater 2014:1--8.
[60] Allaoui S, Boisse P, Chatel S, Hamila N, Hivet G, Soulat D, et al. Experimental and numerical analyses of textile reinforcement forming of a tetrahedral shape. Compos Part A Appl Sci Manuf 2011;42:612–22. doi:10.1016/j.compositesa.2011.02.001.
[61] Gelin JC, Cherouat A, Boisse P, Sabhi H. Manufacture of thin composite structures by the RTM process: numerical simulation of the shaping operation. Compos Sci Technol 1996;56:711–8.
[62] Boisse P, Zouari B, Daniel J-L. Importance of in-plane shear rigidity in finite element analyses of woven fabric composite preforming. Compos Part A Appl Sci Manuf 2006;37:2201–12.
[63] Lin H, Wang J, Long AC, Clifford MJ, Harrison P. Predictive modelling for optimization of textile composite forming. Compos Sci Technol 2007;67:3242–52.
[64] Molnar P, Ogale A, Lahr R, Mitschang P. Influence of drapability by using stitching technology to reduce fabric deformation and shear during thermoforming. Compos Sci Technol 2007;67:3386–93.
[65] Bergsma OK. Computer Simulation of 3 D Forming Processes of Fabric Reinforced Plastics. ICCM/9 Compos Des 1993;4:560–7.
[66] Bergsma OK, Huisman J. Deep drawing of fabric reinforced thermoplastics. Comput Aided Des Compos Mater Technol 1988:323–34.
[67] Wang J, Paton R, Page JR. Draping of woven fabric preforms and prepregs for production of polymer composite components. Compos Part A Appl Sci Manuf 1999;30:757–65. doi:10.1016/S1359-835X(98)00187-0.
[68] Potluri P, Sharma S, Ramgulam R. Comprehensive drape modelling for moulding 3D

textile preforms. Compos Part A Appl Sci Manuf 2001;32:1415–24.
[69] Lee JS, Hong SJ, Yu W-R, Kang TJ. The effect of blank holder force on the stamp forming behavior of non-crimp fabric with a chain stitch. Compos Sci Technol 2007;67:357–66.
[70] Cherouat A, Billoët JL. Mechanical and numerical modelling of composite manufacturing processes deep-drawing and laying-up of thin pre-impregnated woven fabrics. J Mater Process Technol 2001;118:460–71.
[71] Boisse P, Hamila N, Vidal-Sall?? E, Dumont F. Simulation of wrinkling during textile composite reinforcement forming. Influence of tensile, in-plane shear and bending stiffnesses. Compos Sci Technol 2011;71:683–92. doi:10.1016/j.compscitech.2011.01.011.
[72] Mohammed U, Lekakou C, Bader MG. Experimental studies and analysis of the draping of woven fabrics. Compos Part A Appl Sci Manuf 2000;31:1409–20. doi:10.1016/S1359-835X(00)00080-4.
[73] Laroche D, Vu-Khanh T. Forming of woven fabric composites. J Compos Mater 1994;28:1825–39.
[74] Bickerton S, Šimáček P, Guglielmi SE, Advani SG. Investigation of draping and its effects on the mold filling process during manufacturing of a compound curved composite part. Compos Part A Appl Sci Manuf 1997;28:801–16.
[75] Vu-Khanh T, Liu B. Prediction of fibre rearrangement and thermal expansion behaviour of deformed woven-fabric laminates. Compos Sci Technol 1995;53:183–91.
[76] Crossley RJ, Schubel PJ, Warrior NA. The experimental determination of prepreg tack and dynamic stiffness. Compos Part A Appl Sci Manuf 2012;43:423–34. doi:10.1016/j.compositesa.2011.10.014.
[77] Dodwell TJ, Butler R, Hunt GW. Out-of-plane ply wrinkling defects during consolidation over an external radius. Compos Sci Technol 2014;105:151–9. doi:10.1016/j.compscitech.2014.10.007.
[78] Fletcher TA, Butler R, Dodwell TJ. Anti-symmetric laminates for improved consolidation and reduced warp of tapered C-sections. Adv Manuf Polym Compos Sci 2015;1:105–11.
[79] Martin CJ, Seferis JC, Wilhelm MA. Frictional resistance of thermoset prepregs and its influence on honeycomb composite processing. Compos Part A Appl Sci Manuf 1996;27:943–51. doi:10.1016/1359-835X(96)00037-1.
[80] Larberg YR, Åkermo M. On the interply friction of different generations of carbon/epoxy prepreg systems. Compos Part A Appl Sci Manuf 2011;42:1067–74. doi:10.1016/j.compositesa.2011.04.010.
[81] Erland S, Dodwell TJ, Butler R. Characterisation of inter-ply shear in uncured carbon fibre prepreg. Compos Part A Appl Sci Manuf 2015;77:210–8. doi:10.1016/j.compositesa.2015.07.008.
[82] Larberg YR, Åkermo M. In-plane properties of cross-plied unidirectional prepreg. 16th Int. Conf. Compos. Mater. ICCM-16-“ A Giant Step Towar. Environ. Aware. From Green Compos. to Aerospace”, 8 July 2007 through 13 July 2007, Kyoto, Japan, 2007.
[83] Larberg YR, Åkermo M, Norrby M. On the in-plane deformability of cross-plied unidirectional prepreg. J Compos Mater 2011:21998311412988.
[84] Kalebek NA, Babaarslan O. Effect of weight and apllied force on the friction coefficient of the spunlace nonwoven fabrics. Fibers Polym 2010;11:277–84.
[85] Erland S, Dodwell TJ, Butler R, Modelling A. Viscoelastic inter-ply slip in uncured

laminates - experiemntal characterisation and modelling. Iccm 20 2015:19–24.
[86] Gutowski TG, Morigaki T, Cai Z. The consolidation of laminate composites. J Compos Mater 1987;21:172–88.
[87] Hubert P, Poursartip A. A review of flow and compaction modelling relevant to thermoset matrix laminate processing. J Reinf Plast Compos 1998;17:286–318.
[88] Gutowski TG, Dillon G, Chey S, Li H. Laminate wrinkling composites scaling laws for ideal. Compos Manuf 1995;6:123–34.
[89] Tam AS, Gutowski TG. The kinematics for forming ideal aligned fibre composites into complex shapes. Compos Manuf 1990;1:219–28.
[90] Tam AS. A deformation model for the forming of aligned fiber composites 1990.
[91] Johnston A, Vaziri R, Poursartip A. A plane strain model for process-induced deformation of laminated composite structures. J Compos Mater 2001;35:1435–69.
[92] Dodwell TJ. Internal buckling instabilities in layered media. Philos Mag 2015:1–19. doi:10.1080/14786435.2015.1034221.
[93] ten Thije RHW, Akkerman R. Finite element simulations of laminated composites forming processes. Int J Mater Form 2010;3:715–8.
[94] Vanclooster K, Lomov SV, Verpoest I. Simulation of multi-layered composites forming. Int J Mater Form 2010;3:695–8.
[95] Murtagh AM, Lennon JJ, Mallon PJ. Surface friction effects related to pressforming of continuous fibre thermoplastic composites. Compos Manuf 1995;6:169–75.
[96] Gorczyca-Cole JL, Sherwood JA, Chen J. A friction model for thermostamping commingled glass–polypropylene woven fabrics. Compos Part A Appl Sci Manuf 2007;38:393–406.
[97] Mühlhaus H-B, Sakaguchi H, Moresi L, Fahey M. Discrete and continuum modelling of granular materials. Contin. discontinuous Model. cohesive-frictional Mater., Springer; 2001, p. 185–204.
[98] Sulem J, Mühlhaus H. A continuum model for periodic two□dimensional block structures. Mech Cohesive□frictional Mater 1997;2:31–46.
[99] Adhikary DP, Dyskin A V. A Cosserat continuum model for layered materials. Comput Geotech 1997;20:15–45.
[100] Cosserat E, Cosserat F. Théorie des corps déformables. Paris 1909;3:17–29.
[101] Pasternak E, Mühlhaus H-B. Generalised homogenisation procedures for granular materials. Math. Mech. Granul. Mater., Springer; 2005, p. 199–229.
[102] DE BORST R. Simulation of strain localization: a reappraisal of the Cosserat continuum. Eng Comput 1991;8:317–32.
[103] Sulem J, Cerrolaza M. Finite element analysis of the indentation test on rocks with microstructure. Comput Geotech 2002;29:95–117.
[104] Stefanou I, Sulem J, Vardoulakis I. Three-dimensional Cosserat homogenization of masonry structures: elasticity. Acta Geotech 2008;3:71–83.
[105] Forest S, Sab K. Cosserat overall modeling of heterogeneous materials. Mech Res Commun 1998;25:449–54.
[106] Biot MA. Rheological stability with couple stresses and its application to geological folding. Proc. R. Soc. London A Math. Phys. Eng. Sci., vol. 298, The Royal Society; 1967, p. 402–23.
[107] Mühlhaus HB. Continuum models for layered and blocky rock. Compr Rock Eng 2014;2:209–31.

[108] Hallander P, Sjölander J, Petersson M, Åkermo M. Interface manipulation towards wrinkle-free forming of stacked UD prepreg layers. Compos Part A Appl Sci Manuf 2016;90:340–8. doi:10.1016/j.compositesa.2016.07.013.
[109] Sjölander J, Hallander P, Åkermo M. Forming induced wrinkling of composite laminates: A numerical study on wrinkling mechanisms. Compos Part A Appl Sci Manuf 2016;81:41–51. doi:10.1016/j.compositesa.2015.10.012.
[110] Cytec Engineered Materials. Cycom 970 Epoxy Resin System -Technical Data Sheet. 2013.
[111] Dahlquist CA. Adhesion fundamentals and practice. McLaren: London 1966:0–4.
[112] Dahlquist CA. Pressure-sensitive adhesives. Treatise Adhes Adhes 1969;2:219–60.
[113] Dahlquist CA. An investigation into the nature of tack. Adhes Age 1959;2:25–9.
[114] Smith A, Wilkinson SJ, Reynolds WN. The elastic constants of some epoxy resins. J Mater Sci 1974;9:547–50. doi:10.1007/BF00551873.

APPENDIX A – Inter-Laminar Shearing Variables

A.1 Dynamic Shear Stress

A.1.1 Standard Twist with Fiber Angle of 0°

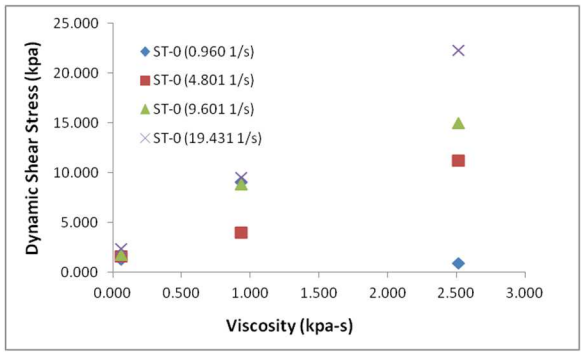

Figure 59: ST-0 Viscosity Effect at 2 kPa

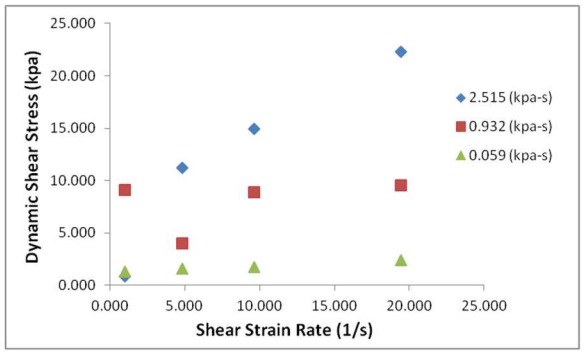

Figure 62: ST-0 Shear Rate Effect at 2 kPa

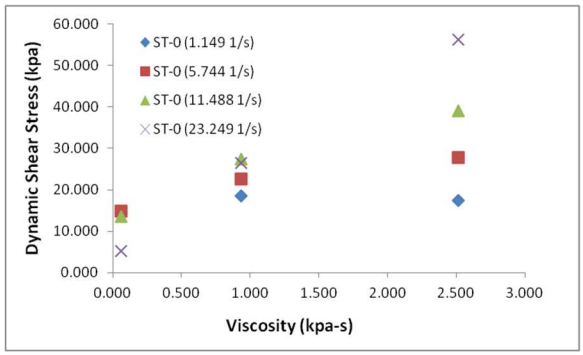

Figure 60: ST-0 Viscosity Effect at 24 kPa

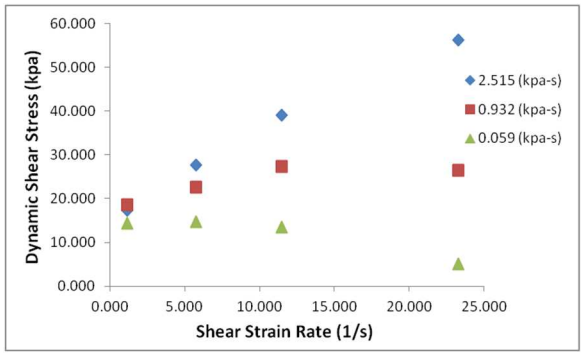

Figure 63: ST-0 Shear Rate Effect at 24 kPa

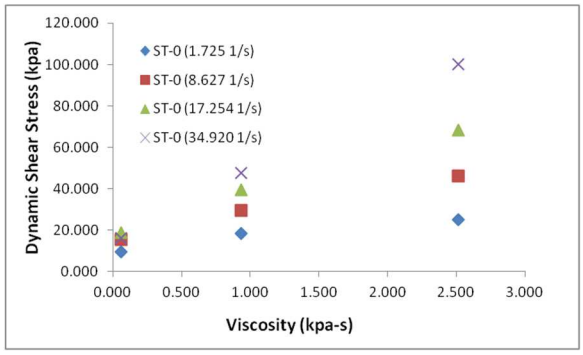

Figure 61: ST-0 Viscosity Effect at 48 kPa

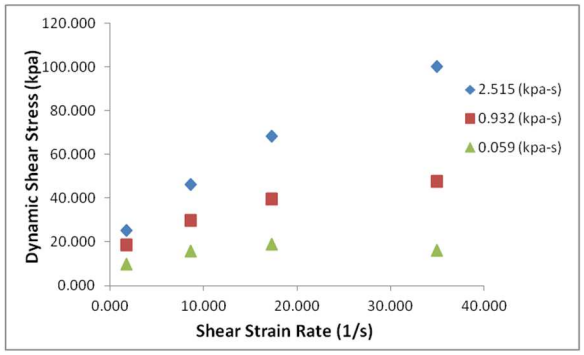

Figure 64: ST-0 Shear Rate Effect at 48 kPa

A.1.2 Standard Twist with Fiber Angle of 45°

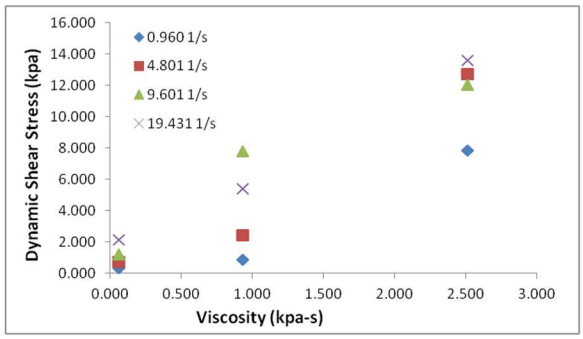

Figure 65: ST-45 Viscosity Effect at 2 kPa

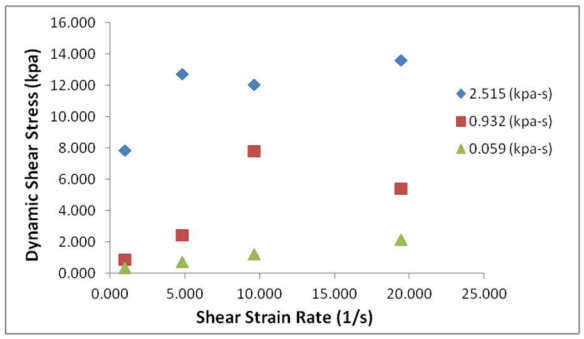

Figure 68: ST-45 Shear Rate Effect at 2 kPa

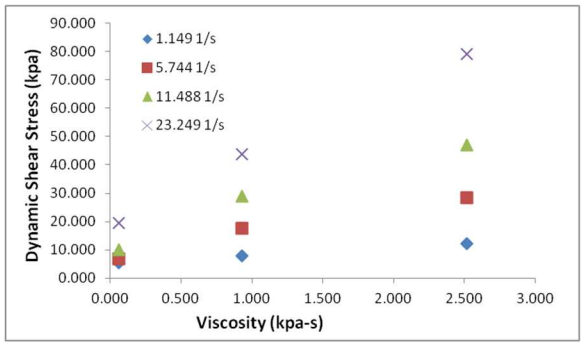

Figure 66: ST-45 Viscosity Effect at 24 kPa

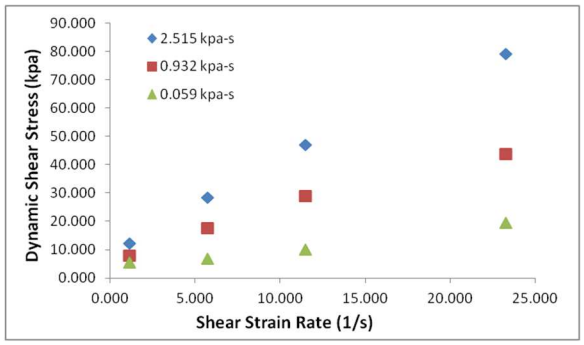

Figure 69: ST-45 Shear Rate Effect at 24kPa

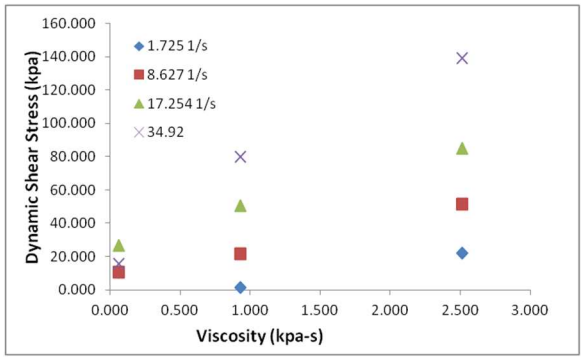

Figure 67: ST-45 Viscosity Effect at 48 kPa

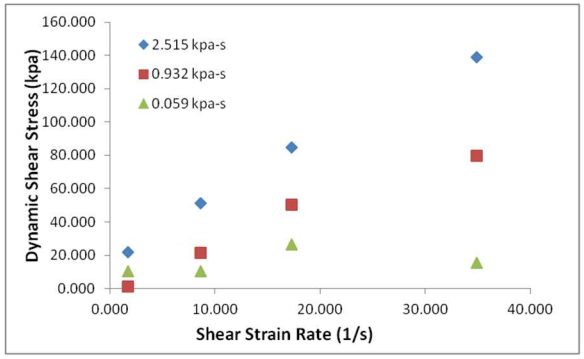

Figure 70: ST-45 Shear Rate Effect at 48kPa

A.1.3 Never Twist with Fiber Angle of 0°

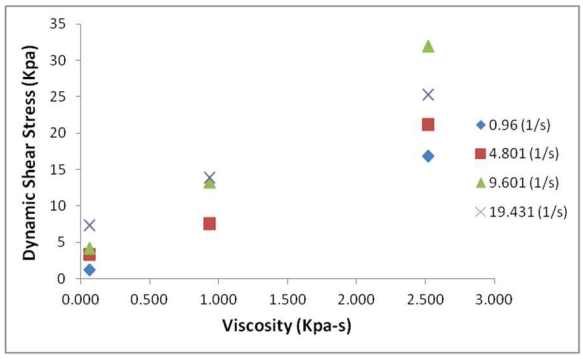

Figure 71: NT-0 Viscosity Effect at 2 kPa

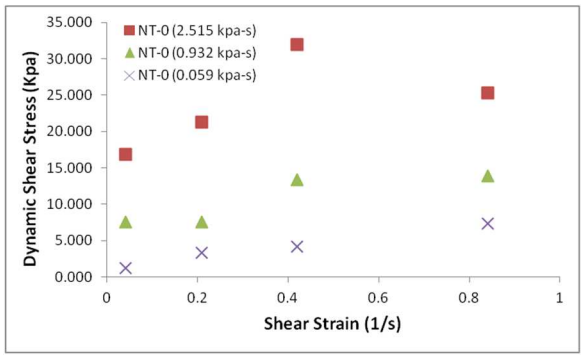

Figure 74: NT-0 Shear Rate Effect at 2 kPa

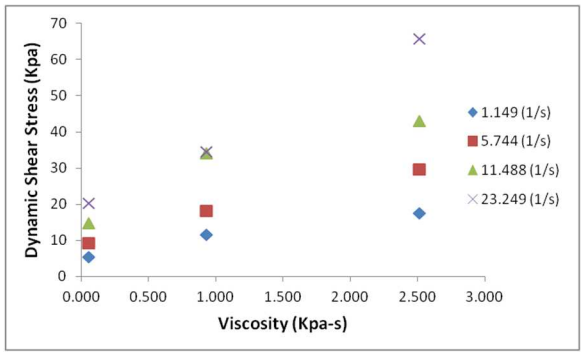

Figure 72: NT-0 Viscosity Effect at 24 kPa

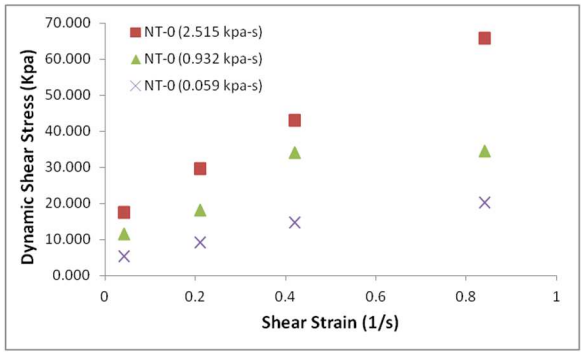

Figure 75: NT-0 Shear Rate Effect at 24 kPa

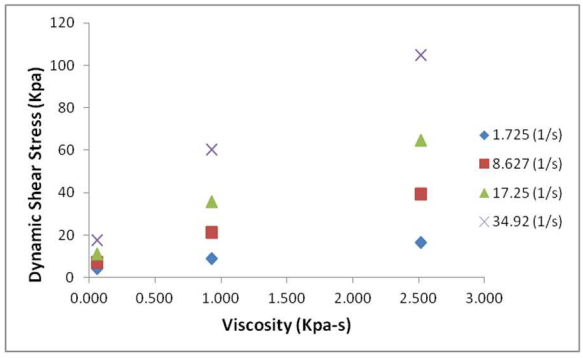

Figure 73: NT-0 Viscosity Effect at 48 kPa

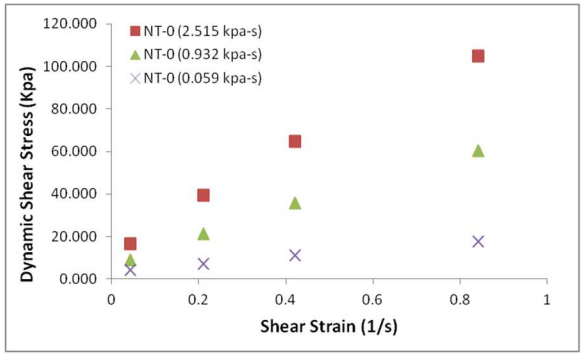

Figure 76: NT-0 Shear Rate Effect at 48 kPa

A.1.4 Never Twist with Fiber Angle of 45°

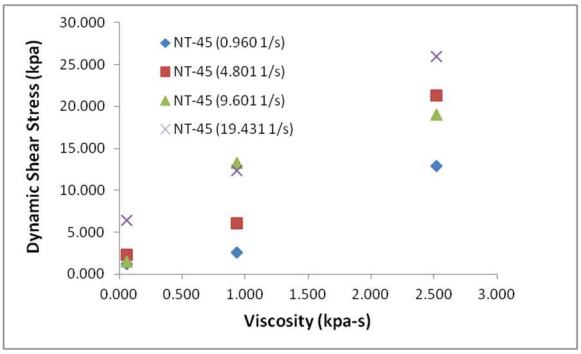

Figure 77: NT-45 Viscosity Effect at 2 kPa

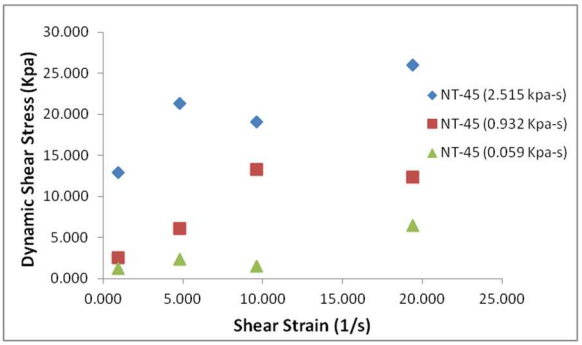

Figure 80: NT-45 Shear Rate Effect at 2 kPa

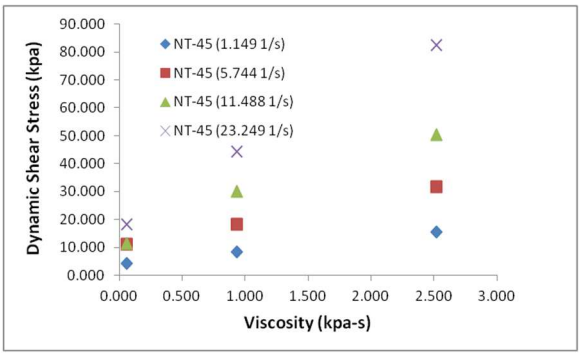

Figure 78: NT-45 Viscosity Effect at 24 kPa

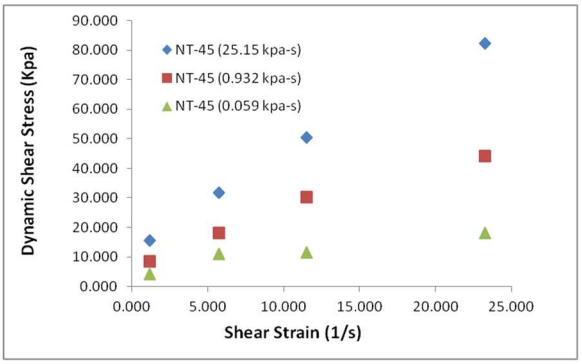

Figure 81: NT-45 Shear Rate Effect at 24kPa

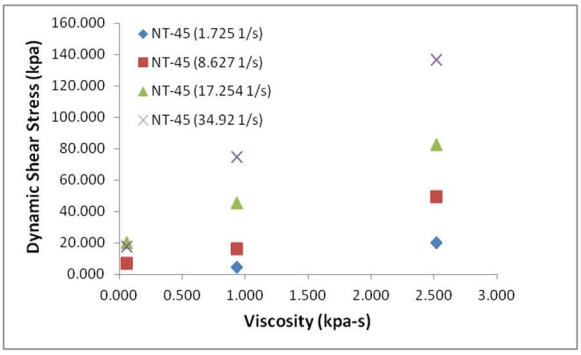

Figure 79: NT-45 Viscosity Effect at 48 kPa

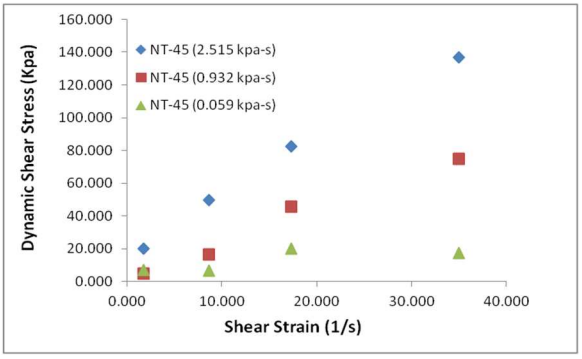

Figure 82: NT-45 Shear Rate Effect at 48 kPa

A.2 Static Shear Stress

A.2.1 Standard Twist with Fiber Angle of 0°

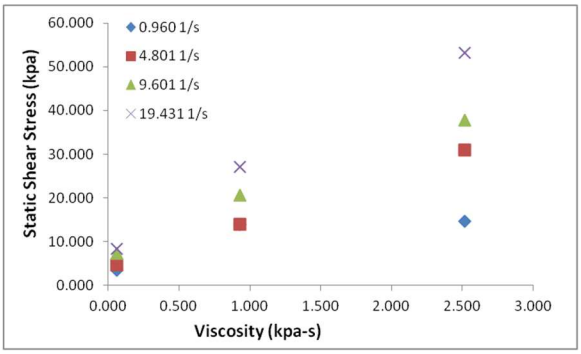

Figure 83: ST-0 Viscosity Effect at 2 kPa

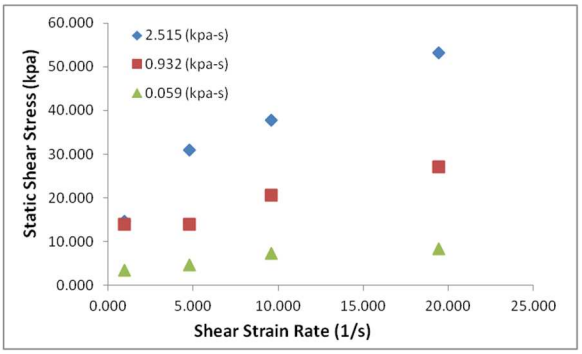

Figure 86: ST-0 Shear Rate Effect at 2 kPa

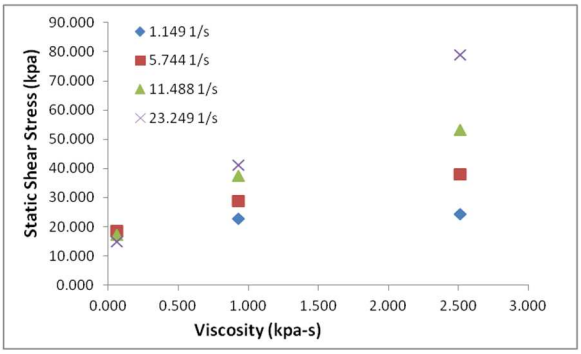

Figure 84: ST-0 Viscosity Effect at 24 kPa

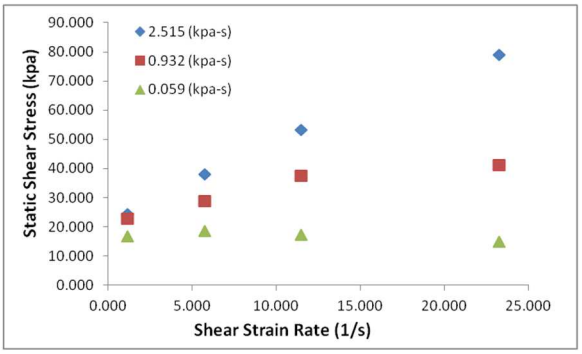

Figure 87: ST-0 Shear Rate Effect at 24 kPa

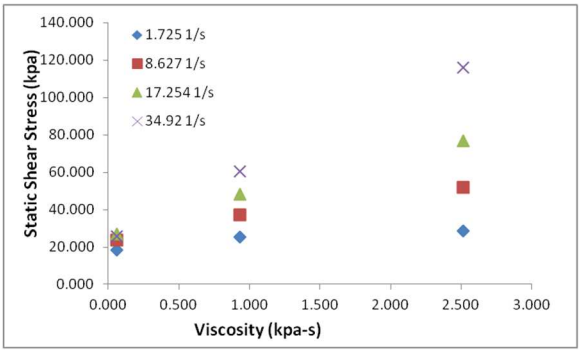

Figure 85: ST-0 Viscosity Effect at 48 kPa

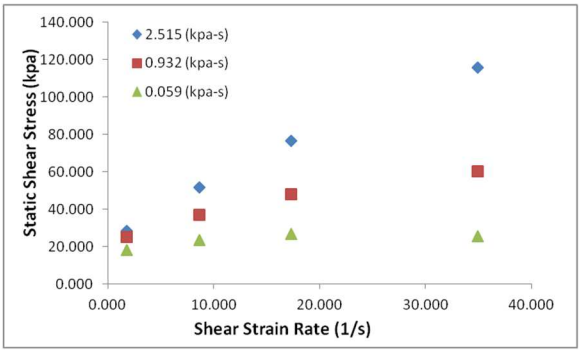

Figure 88: ST-0 Shear Rate Effect at 48 kPa

A.2.2 Standard Twist with Fiber Angle of 45°

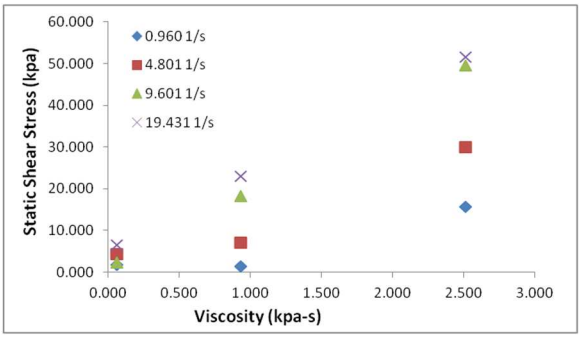

Figure 89: ST-45 Viscosity Effect at 2 kPa

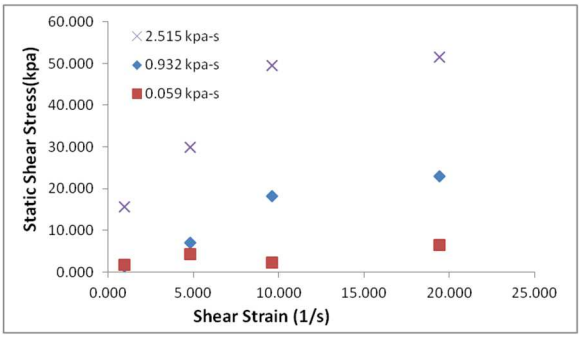

Figure 92: ST-45 Shear Rate Effect at 2 kPa

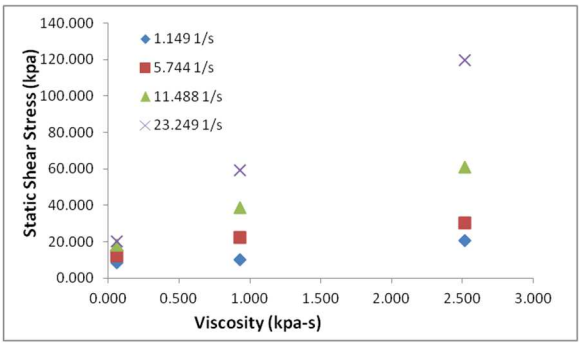

Figure 90: ST-45 Viscosity Effect at 24 kPa

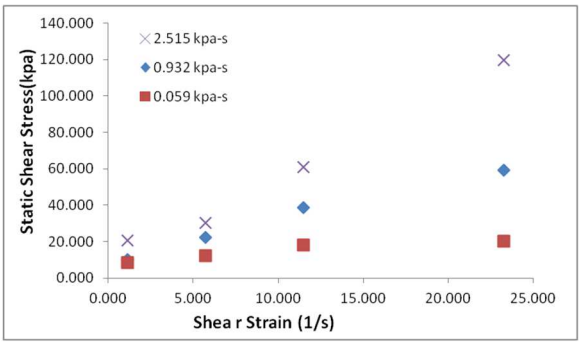

Figure 93: ST-45 Shear Rate Effect at 24 kPa

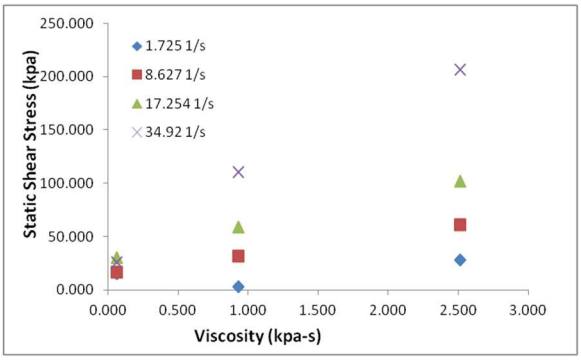

Figure 91: ST-45 Viscosity Effect at 48 kPa

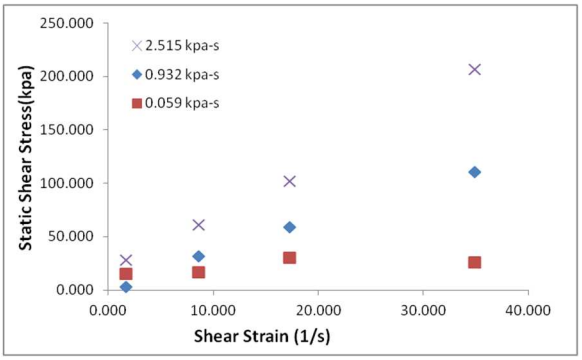

Figure 94: ST-45 Shear Rate Effect at 48 kPa

A.2.3 Never Twist with Fiber Angle of 0°

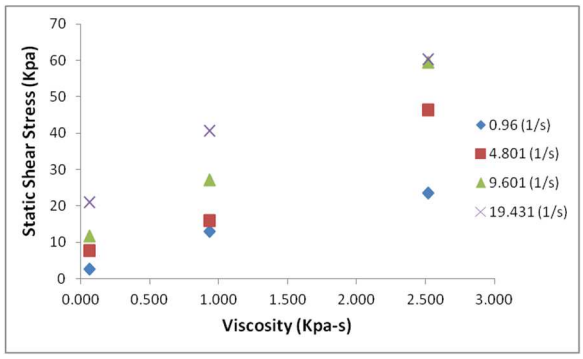

Figure 95: NT-0 Viscosity Effect at 2 kPa

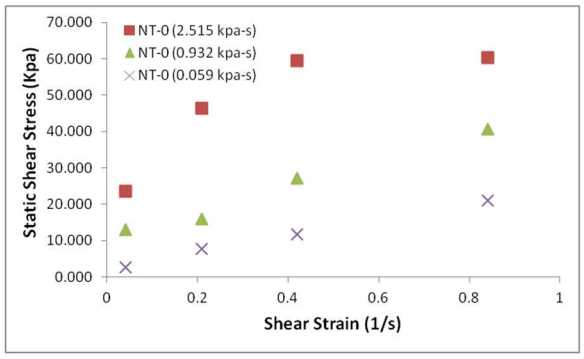

Figure 98: NT-0 Shear Rate Effect at 2 kPa

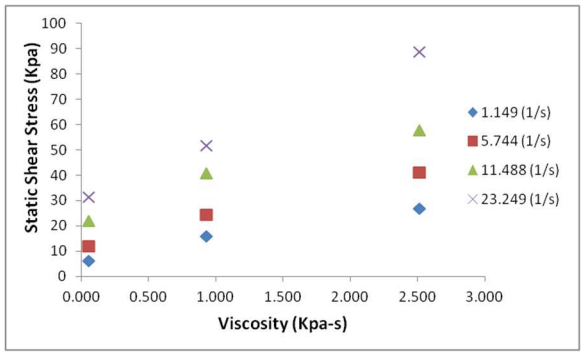

Figure 96: NT-0 Viscosity Effect at 24 kPa

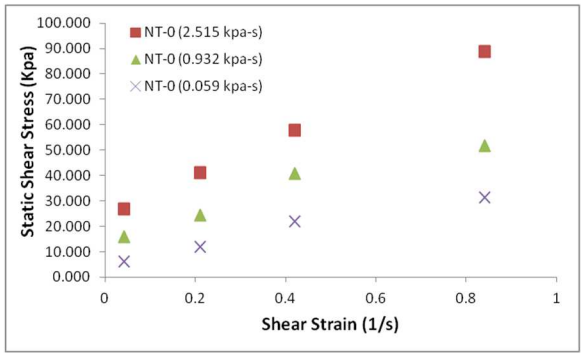

Figure 99: NT-0 Shear Rate Effect at 24 kPa

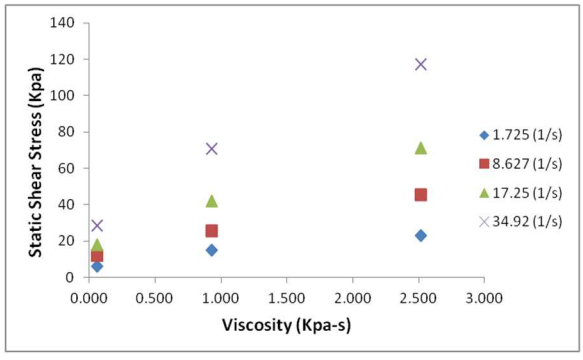

Figure 97: NT-0 Viscosity Effect at 48 kPa

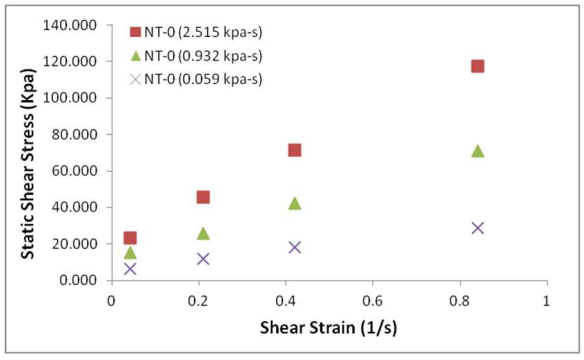

Figure 100: NT-0 Shear Rate Effect at 48 kPa

A.2.4 Never Twist with Fiber Angle of 45°

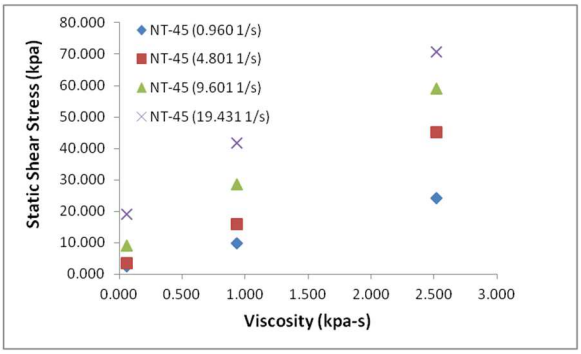

Figure 101: NT-45 Viscosity Effect at 2 kPa

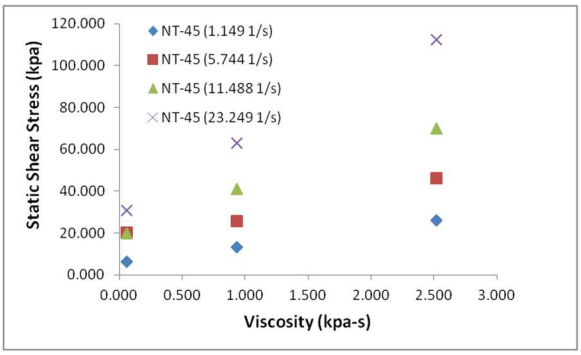

Figure 102: NT-45 Viscosity Effect at 24 kPa

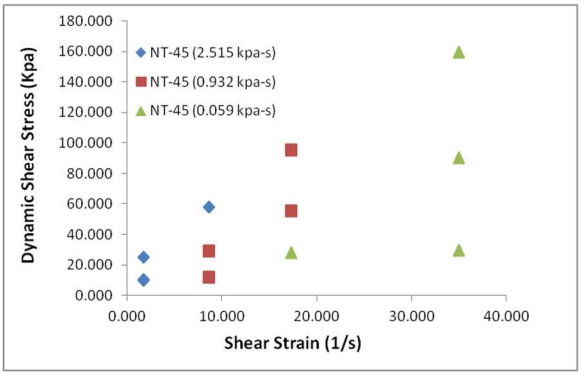

Figure 103: NT-45 Viscosity Effect at 48 kPa

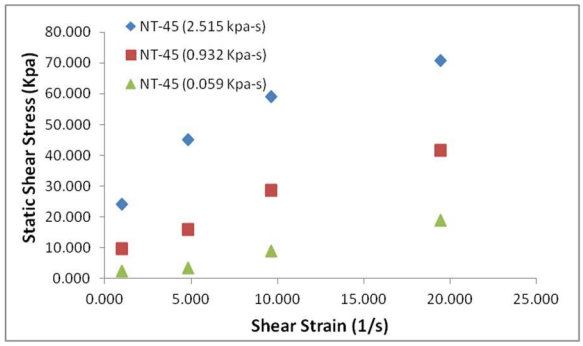

Figure 104: NT-45 Shear Rate Effect at 2 kPa

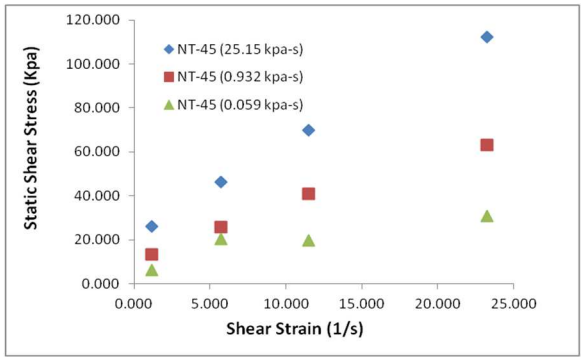

Figure 105: NT-45 Shear Rate Effect at 24 kPa

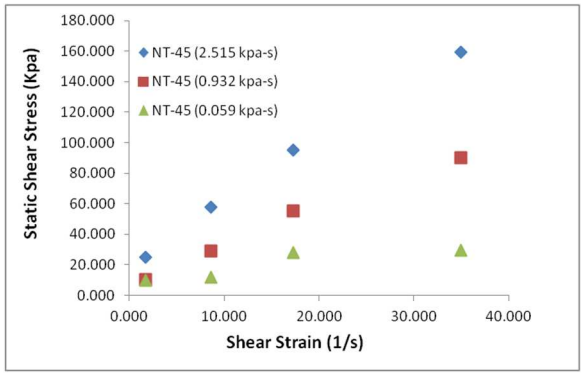

Figure 106: NT-45 Shear Rate Effect at 48 kPa

A.3 Shear Modulus

A.3.1 Standard Twist with Fiber Angle of 0°

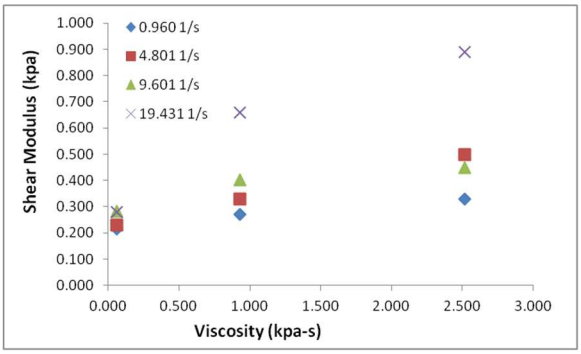

Figure 107: ST-0 Viscosity Effect at 2 kPa

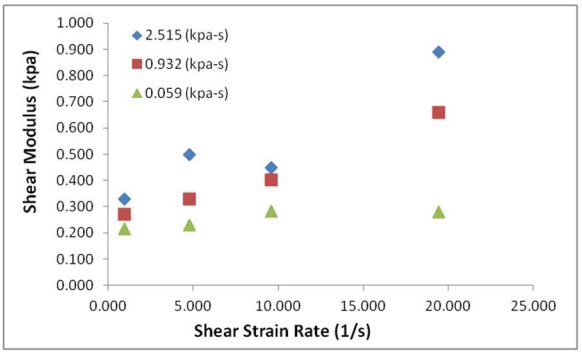

Figure 110: ST-0 Shear Rate Effect at 2 kPa

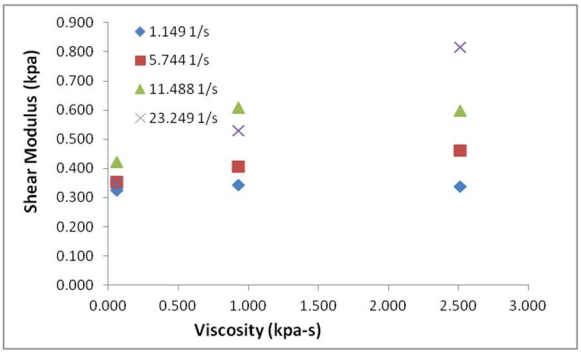

Figure 108: ST-0 Viscosity Effect at 24 kPa

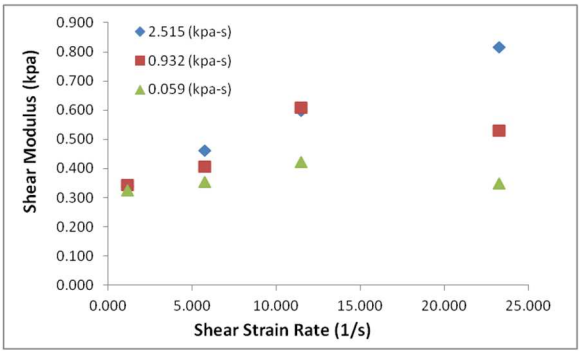

Figure 111: ST-0 Shear Rate Effect at 24 kPa

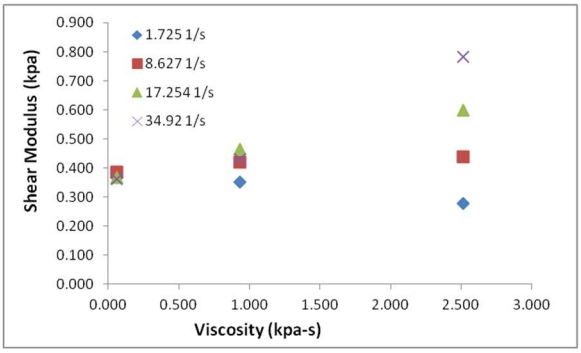

Figure 109: ST-0 Viscosity Effect at 48 kPa

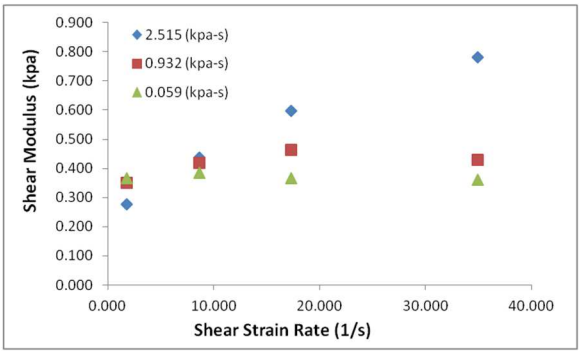

Figure 112: ST-0 Shear Rate Effect at 48 kPa

A.3.2 Standard Twist with Fiber Angle of 45°

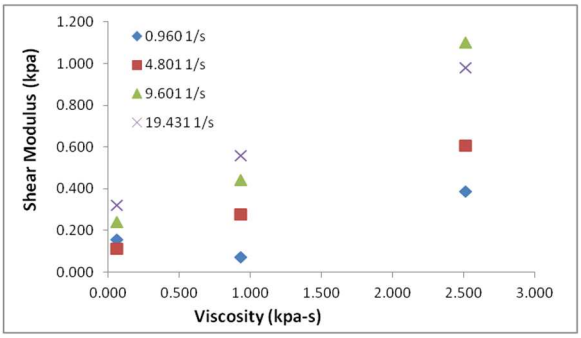

Figure 113: ST-45 Viscosity Effect at 2 kPa

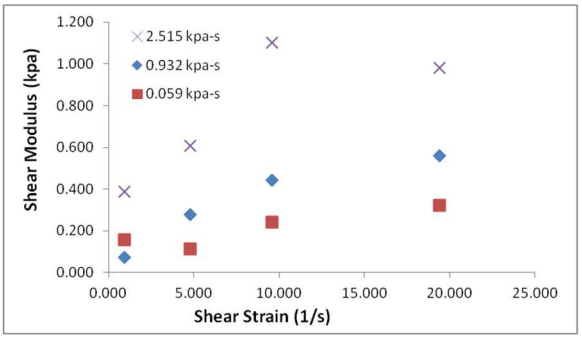

Figure 116: ST-45 Shear Rate Effect at 2 kPa

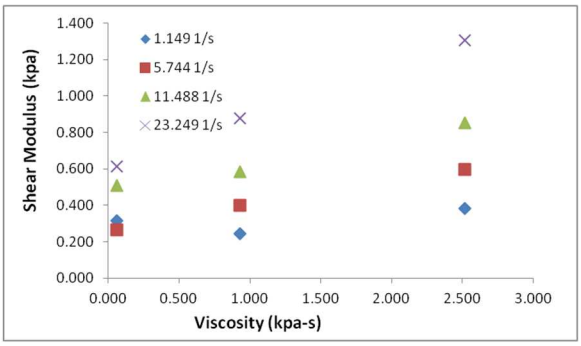

Figure 114: ST-45 Viscosity Effect at 24 kPa

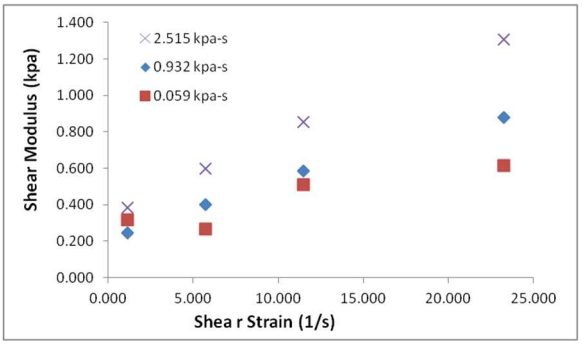

Figure 117: ST-45 Shear Rate Effect at 24 kPa

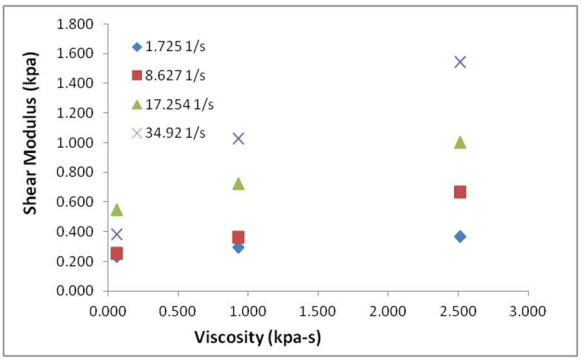

Figure 115: ST-45 Viscosity Effect at 48 kPa

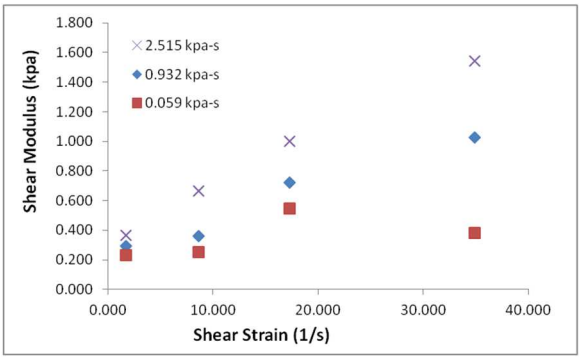

Figure 118: ST-45 Shear Rate Effect at 48 kPa

A.3.3 Never Twist with Fiber Angle of 0°

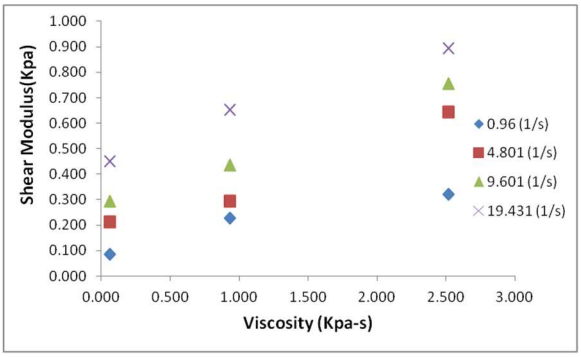

Figure 119: NT-0 Viscosity Effect at 2 kPa

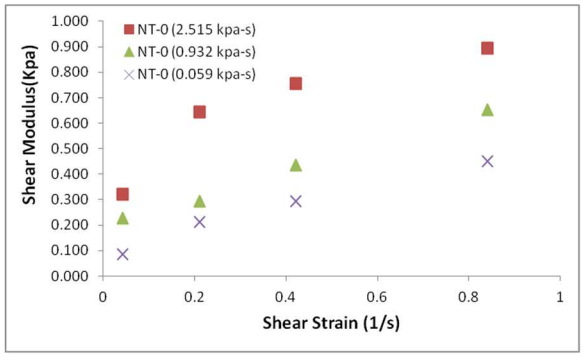

Figure 122: NT-0 Shear Rate Effect at 2 kPa

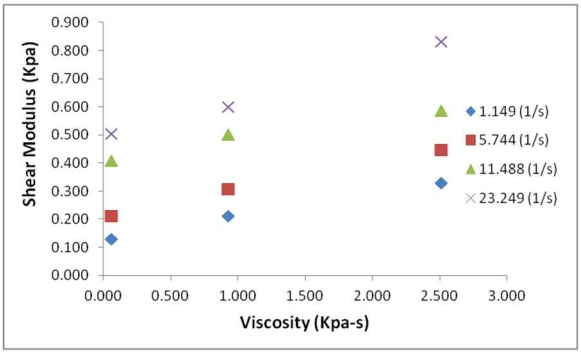

Figure 120: NT-0 Viscosity Effect at 24 kPa

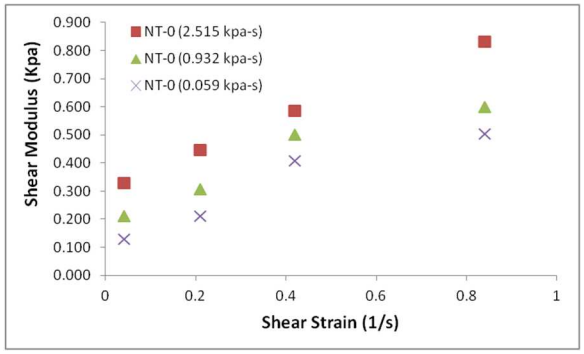

Figure 123: NT-0 Shear Rate Effect at 24 kPa

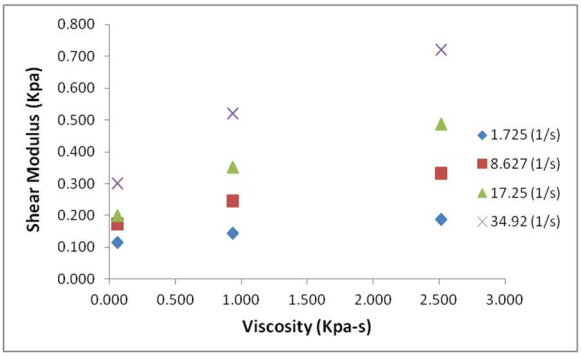

Figure 121: NT-0 Viscosity Effect at 48 kPa

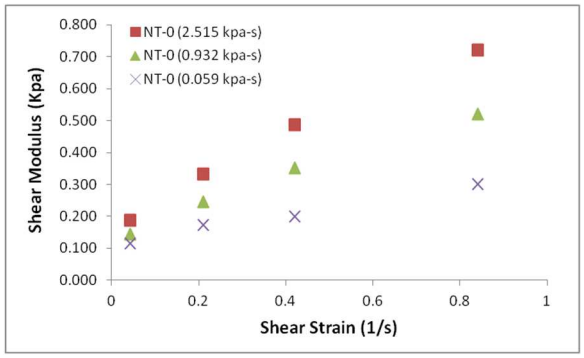

Figure 124: NT-0 Shear Rate Effect at 48 kPa

A.3.4 Never Twist with Fiber Angle of 45°

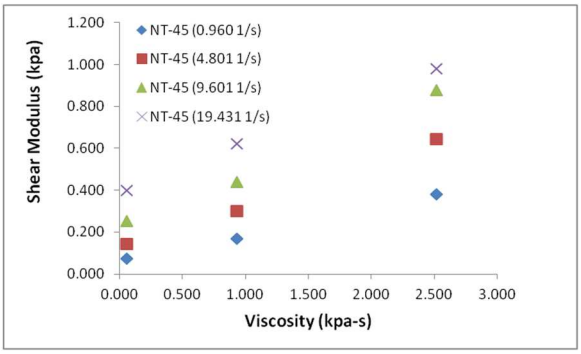

Figure 125: NT-45 Viscosity Effect at 2 kPa

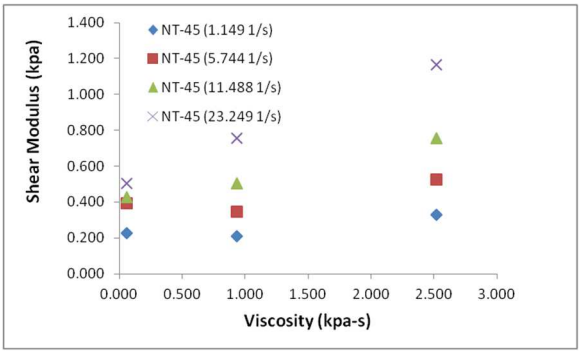

Figure 126: NT-45 Viscosity Effect at 24 kPa

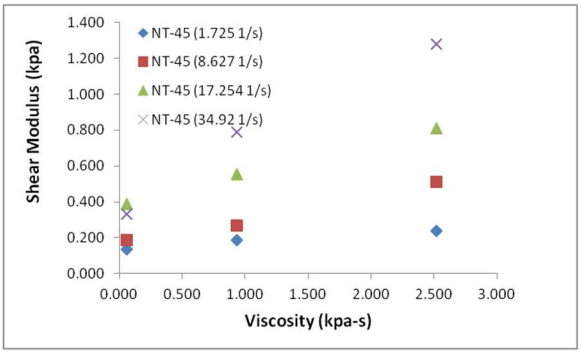

Figure 127: NT-45 Viscosity Effect at 48 kPa

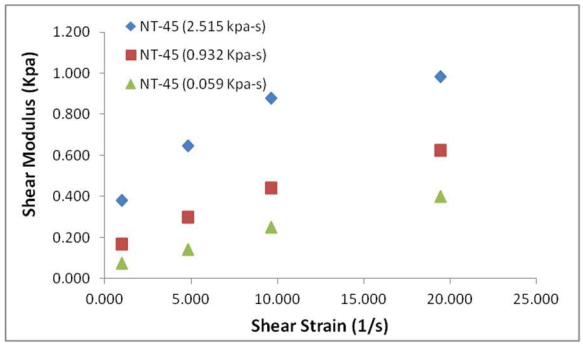

Figure 128: NT-45 Shear Rate Effect at 2 kPa

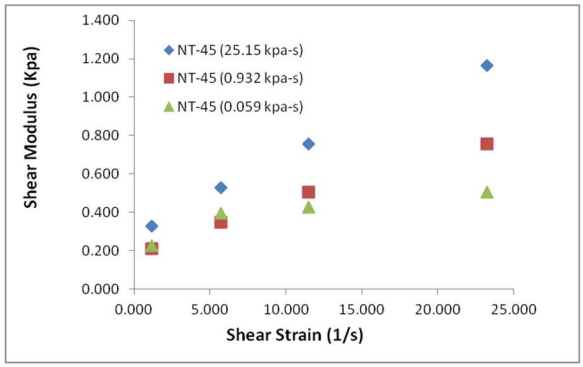

Figure 129: NT-45 Shear Rate Effect at 24 kPa

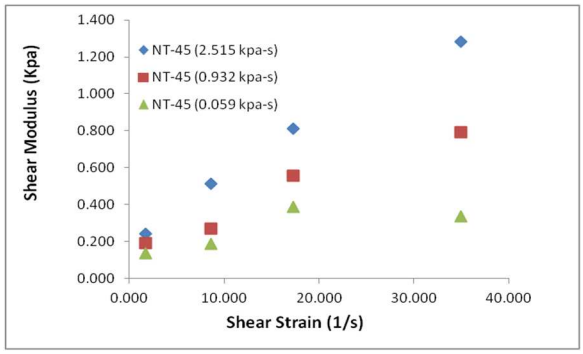

Figure 130: NT-45 Shear Rate Effect at 48 kPa

Appendix B – Inter-Laminar Shearing Plots

B.1 Correlation of Critical Strain Model with Experimental Data

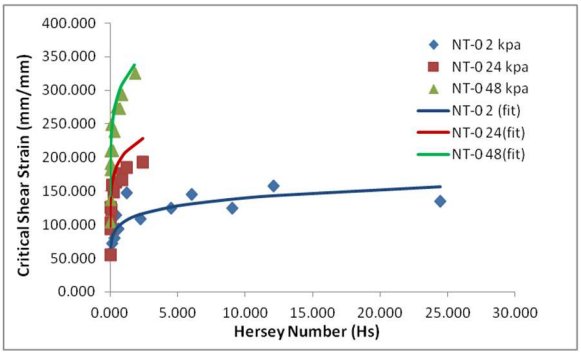

Figure 131: Critical Strain Model versus Experimental For NT-0

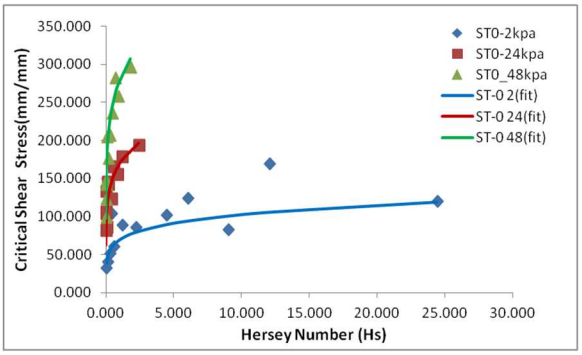

Figure 133: Critical Strain Model versus Experimental Data for ST-0

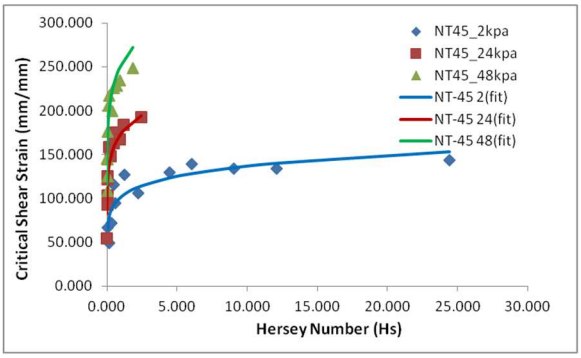

Figure 132: Critical Strain Model versus Experimental Data for NT-45

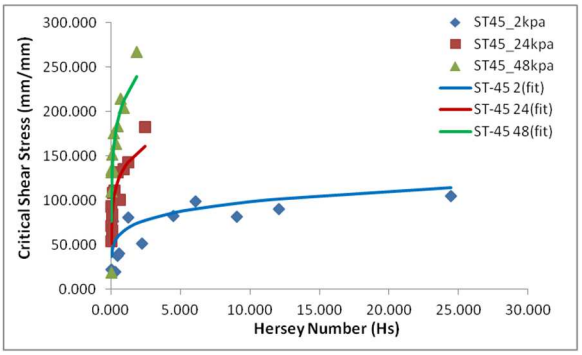

Figure 134: Critical Strain Model versus Experimental Data for ST-45

B.2 Correlation of Shear Modulus with Experimental Data

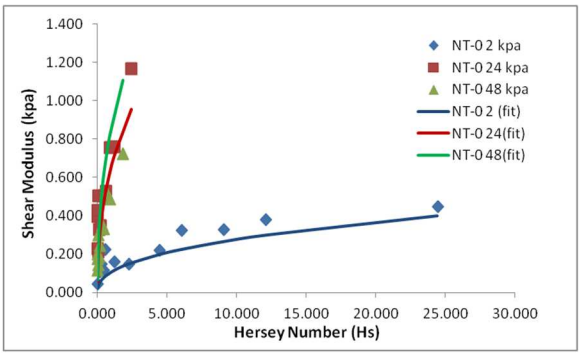

Figure 135: Shear Modulus versus Experimental Data for NT-0

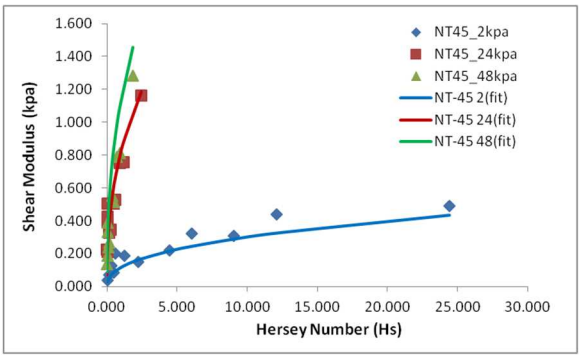

Figure 136: Shear Modulus versus Experimental Data for NT-45

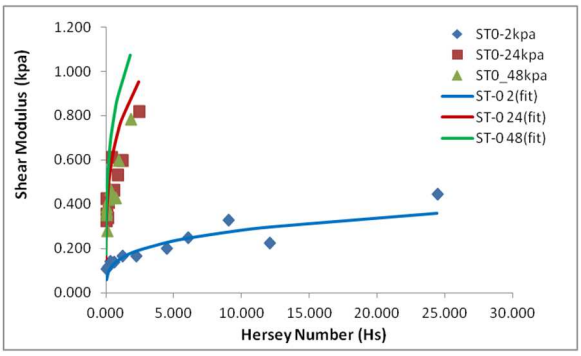

Figure 137: Shear Modulus versus Experimental Data for ST-0

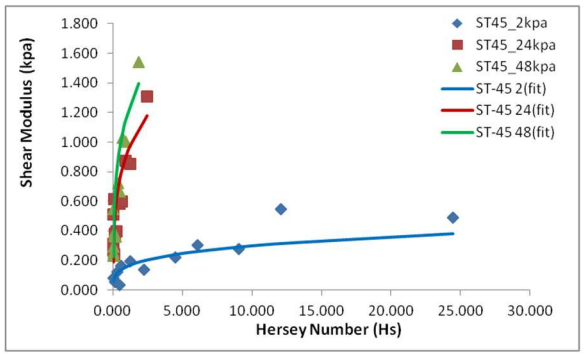

Figure 138: Shear Modulus versus Experimental Data for ST-45

B.3 Effect of Pressure on Critical Strain

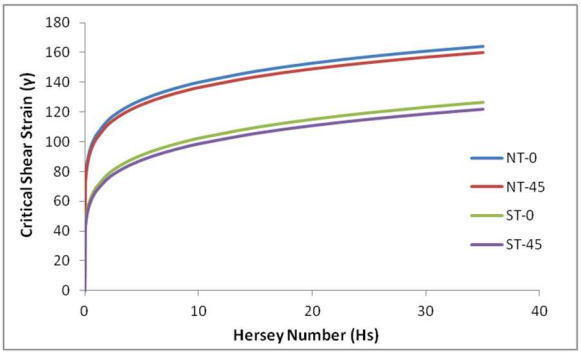

Figure 139: Critical Shear Strain at P=2 kPa

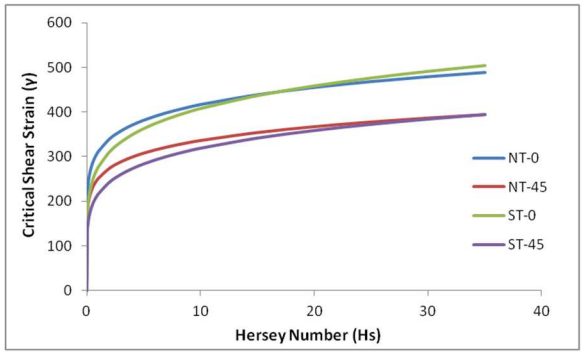

Figure 141: Critical Shear Strain at P=48 kPa

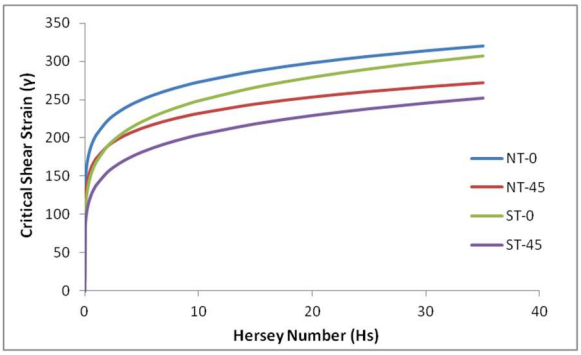

Figure 140: Critical Shear Strain at P=24 kPa

B.4 Effect of Pressure on Shear Modulus

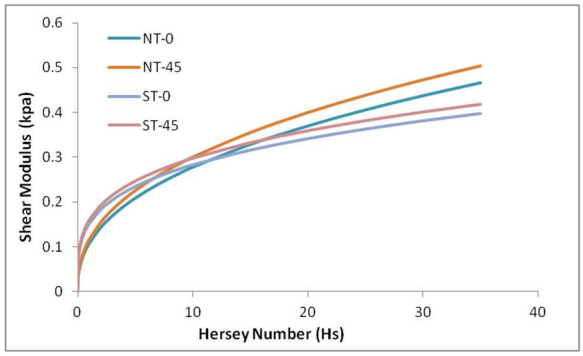

Figure 142: Shear Modulus at P=2 kPa

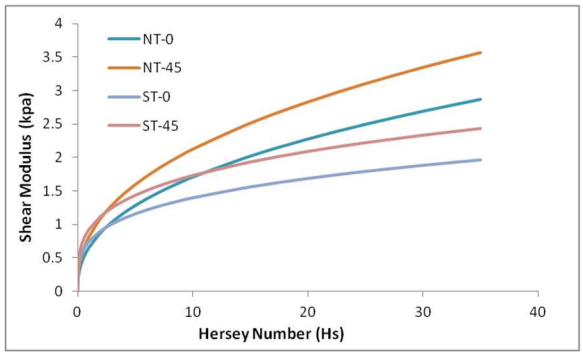

Figure 143: Shear Modulus at P=24 KPa

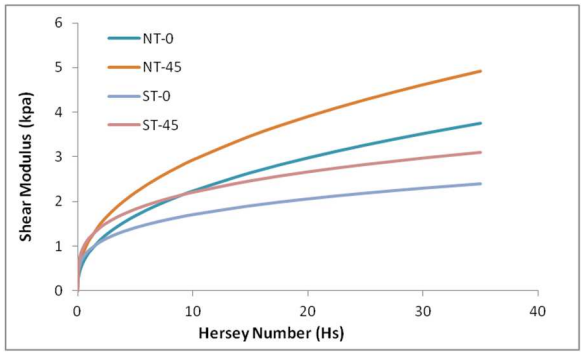

Figure 144: Shear Modulus at P=48 kPa

B.5 Effect of Pressure on Toughness

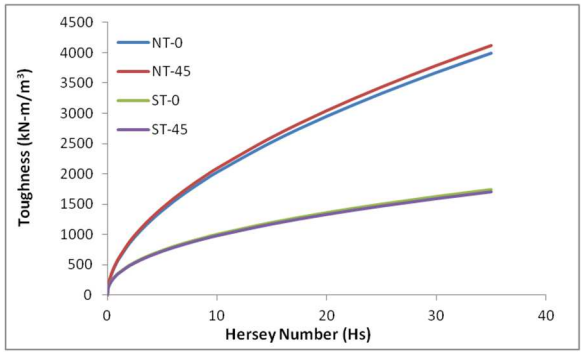

Figure 145: Toughness at P=2

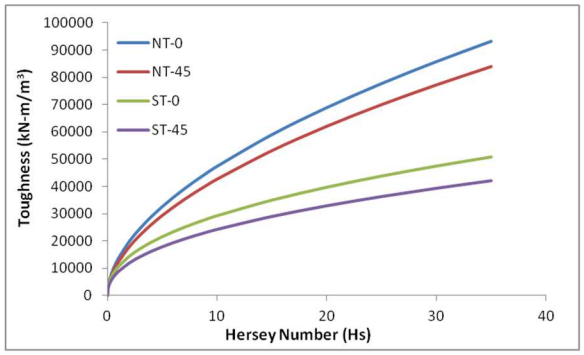

Figure 146: Toughness at P=24 kPa

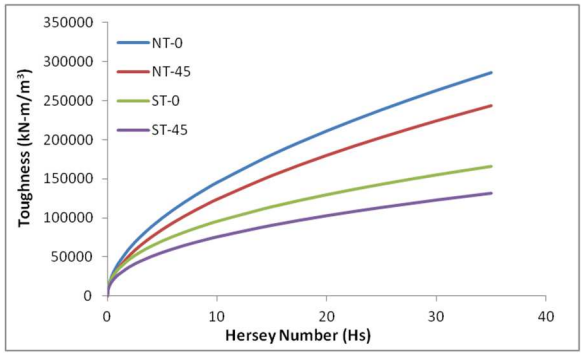

Figure 147: Toughness at P=48 kPa

Appendix C – Low Heresy Graphs at 48 kPa

C.1 Coefficient of Frictions

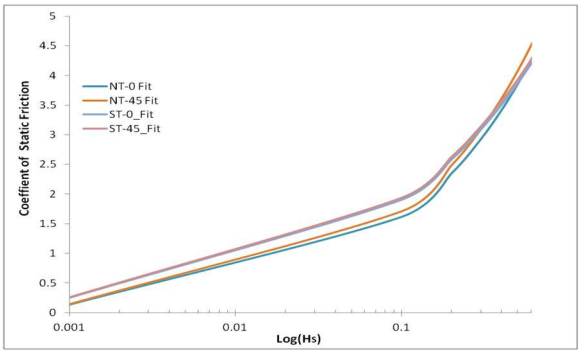

Figure 148: Coefficient of Static Friction at Low Hersey Numbers

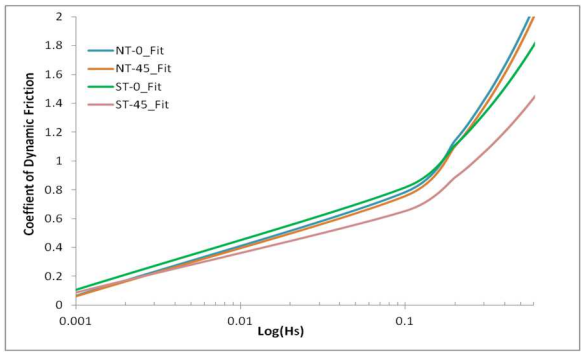

Figure 149: Coefficient of Dynamic Friction at Low Hersey Numbers

C.2 Critical Strain

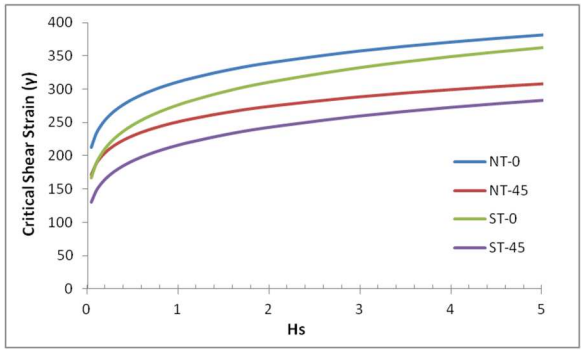

Figure 150: Critical Shear Strain at low Hersey Numbers

C.3 Shear Modulus

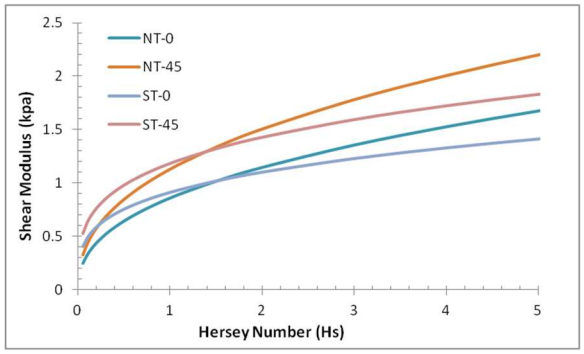

Figure 151: Shear Modulus at Low Hersey Numbers

C.4 Toughness

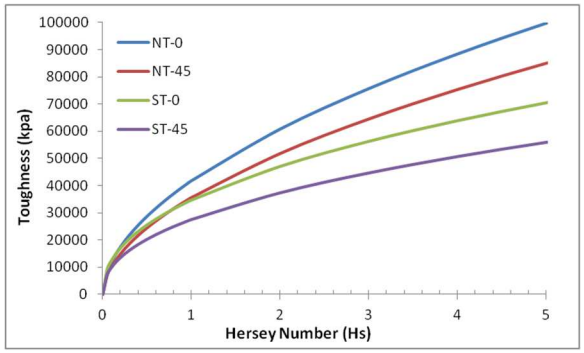

Figure 152: Toughness at Low Hersey Number

Appendix D – Matlab Functions for Wrinkle Prediction Model

This section contains the matlab script and functions used to calculate the wrinkle model.

D.1 Base Script

```
 clc
clear
% format shortg
%% Inputs
Laminate=[45,0,45,0,45,0,45,0,45,0,45,0,45,0,45,0,45,45,0,45,0,45,0,45,0,45,0,45,0
,45,0,45];
% Laminate =[45,0,45,0,45,0,45,0,45,45,0,45,0,45,0,45,0,45];
% Laminate =[45,0,45,0,45,45,0,45,0,45];
Twist=1        % NT=0, ST=1
Vac=2;          % Vacuum Rate in inHg/min
Po=2;           % initial laminate pressure in kPa
[oo Ply]=size(Laminate);
st=0.0331*Vac*Ply;
tR=(-4E-07*Po+5E-05)/(0.0086*25.4/1000);

M_tack=[3.4203e+05, 3.5237e+05, 2.5238e+05, 1.5261e+05, 1.3045e+05,
1.2045e5];
M_Debulk=2e6;

%% ABD variation with Hs
mua=[2.51 0.93 0.37 0.10 0.06 0.04];  % resin viscosity kPa-s
Hs=st.*mua./Po;
[aa, bb]=size(mua);

% beam inputs
a=38*25.4/1000;
K=6/5;

%  plate inputs
n=1; m=1;
b=(3*25.4/1000);
ax=m*pi/(a);
by=n*pi/b;


%% Calculation Loop
for i=1:bb;
    mu=mua(i);
    [~, B, D, ei,z]=ABDg(Laminate,Twist,Po,st,mu); % Laminate Variables
    [A,~,~]=ABD0(Laminate,Twist,Po,st,mu); % Interface Variable
    ABD=[A B;B D];
    e=[0;ei(2,1)*(Ply-1);0;0;0;0];%*(2*Ply-1)
    N(:,i)=ABD*e;

    M=inv([A B;B D]);
    Di=M(4:6,4:6);
```

```
    %% G13
    h=z(end,3)*2;
    Gxz(i)=1/(M(3,3)*h);
    G13i=M_Debulk;
    [~, A55,~]=ABD0f(Laminate,Twist,Po,st,mu,0,G13i);
    Ai55=inv(A55);
    Gxz2(i)=1/(Ai55(3,3)*h);

 %% CLPT Beam
    Nc_FF(i)=(pi/a)^2/Di(1,1);
    Nc_Cb(i)=(pi/(2*b))^2/Di(1,1);

%% FSDT Beam
    NF_FF(i)=1/Di(1,1)*(pi/(a))^2*(1+(1/Di(1,1)*(pi/(a))^2)/(K*Gxz2(i)*h));
    Nf_Cb(i)=1/Di(1,1)*(pi/(2*a))^2
*(1+((pi/(2*a))^2)/(Di(1,1)*K*Gxz2(i)*h));

%% Plate theory
    % when B=0; FSDT reduces to CLPT plate theory.
    k=A(1,2)/A(1,1);
    c33=D(1,1)*ax^4+2*(D(1,2)+2*D(3,3))*ax^2*by^2+D(2,2)*by^4;
    N_plate(i)=c33/(ax^2+k*by^2);

end

%% Plots
figure
hold on
plot(Hs,Nc_FF,'r--')
plot(Hs,Nc_Cb,'m--')
plot(Hs,Nf_Cb,'m')
plot(Hs,NF_FF,'r')
plot(Hs,N_plate,'b')
xlabel('Hersey Number')
ylabel('Critical Buckling Stress (Pa)')
plot(Hs,N(1,:),'d',Hs,N(2,:),'o')
legend('C-FF','C-CB','F-CB','F-FF','Plate','\sigma_x_x','\sigma_y_y')
```

D.2 Function ABDg

```
%
% this function calculates the A, B, and D matrix for a green PW laminate
%
function [A, B, D, ei,z]=
ABDg(Laminate,Twist,Initial_Pressure,Strain_Rate,Viscosity)
p=Initial_Pressure; st=Strain_Rate; mu=Viscosity;
% Laminate=[45,0,45,0,45,45,0,45,0,45] Layup referening major ply angle
% Twist    NT=0, ST=1
% mu      resin viscosity kPa-s
% p= initial laminate pressure in kPa
%st= strain rate of laminate forming over radius (1/s)
```

```
%% Interface Properties
[Ei Gi vi ei] = EGv(Twist,p,st,mu);
ti=-4E-07*p+5E-05;              % thickness of resin interface in meters

%% Carbon Properties
Ec=58e9;
Gc=5.e9;
vc=0.1;
tc=0.0086*25.4/1000;          % thickness of Carbon Ply in meters

%% Calculation of Q's
% carbon
Qc11=Ec/(1-vc*vc);
Qc22=Ec/(1-vc*vc);
Qc66=Gc;
Qc12=vc*Ec/(1-vc*vc);
% interface
Qi11=Ei./(1-vi.^2);
Qi22=Ei./(1-vi.^2);
Qi66=Gi;
Qi12=vi.*Ei./(1-vi.^2);

%% Calculation of Qbar's
Angles=[0 45];
Qbc=Qbars(Qc11,Qc12,Qc22,Qc66,Angles);
for i=1:2
    ori=Angles(i);
    Qbi(i,:)=Qbars(Qi11(i),Qi12(i),Qi22(i),Qi66(i),ori);
end

%% Zk's
[n m]=size(Laminate);
ml=2*m-1;
z=zeros(ml,7);
j=1;
for i=1:2:ml        %Ply Angle and Thickness
    z(i,2)=tc;
    z(i,1)=Laminate(j);
    if i>1
        z(i-1,2)=ti;
        if Laminate(j)~=Laminate(j-1)
            z(i-1,1)=45;
        else
            z(i-1,1)=0;
        end
    end
    j=j+1;
end
z(m,3)=z(m,2)/2;    % Midply zk+1 *NOTE: Must have even ply count
z(m,4)=-z(m,2)/2;   % MidPly zk-1 *NOTE: must have even ply count
j=1;                % Counter
for i=m+1:ml        % Zk+1 (3) Zk-1 (4)
    z(i,3)=z(i,2)+z(i-1,3); %zk+1 positive
    z(i,4)=z(i-1,3);        %zk-1 positive
    z(m-j,4)=-z(m-j,2)+z(m-j+1,4); %zk+1 negative
```

```
    z(m-j,3)=z(m-j+1,4);            %zk-1 negative
    j=j+1;
end
for i=1:ml          % z,z2,z3
    z(i,5)=z(i,3)-z(i,4);       %Zk-Zk-1
    z(i,6)=(z(i,3)^2-z(i,4)^2)./2;   %Zk^2-Zk-1^2
    z(i,7)=(z(i,3)^3-z(i,4)^3)./3;   %Zk^3-Zk-1^3
end

%% Laminate ABD's
A=zeros(3,3); B=zeros(3,3); D=zeros(3,3);
for i=1:ml
    if z(i,2)==tc
        if z(i,1)==45
            Qb=Qbc(2,:);
        elseif z(i,1)==0
            Qb=Qbc(1,:);
        else
            display('error')
        end
    elseif z(i,2)==ti
        if z(i,1)==45
            Qb=Qbi(2,:);
        elseif z(i,1)==0
            Qb=Qbi(1,:);
        else
            display('error')
        end
    end
    A(1,1)=Qb(2)*z(i,5)+A(1,1);
    A(1,2)=Qb(3)*z(i,5)+A(1,2);
    A(2,2)=Qb(4)*z(i,5)+A(2,2);
    A(1,3)=Qb(5)*z(i,5)+A(1,3);
    A(2,3)=Qb(6)*z(i,5)+A(2,3);
    A(3,3)=Qb(7)*z(i,5)+A(3,3);
    A(2,1)=A(1,2); A(3,1)=A(1,3); A(3,2)=A(2,3);

    B(1,1)=Qb(2)*z(i,6)+B(1,1);
    B(1,2)=Qb(3)*z(i,6)+B(1,2);
    B(2,2)=Qb(4)*z(i,6)+B(2,2);
    B(1,3)=Qb(5)*z(i,6)+B(1,3);
    B(2,3)=Qb(6)*z(i,6)+B(2,3);
    B(3,3)=Qb(7)*z(i,6)+B(3,3);
    B(2,1)=B(1,2); B(3,1)=B(1,3); B(3,2)=B(2,3);

    D(1,1)=Qb(2)*z(i,7)+D(1,1);
    D(1,2)=Qb(3)*z(i,7)+D(1,2);
    D(2,2)=Qb(4)*z(i,7)+D(2,2);
    D(1,3)=Qb(5)*z(i,7)+D(1,3);
    D(2,3)=Qb(6)*z(i,7)+D(2,3);
    D(3,3)=Qb(7)*z(i,7)+D(3,3);
    D(2,1)=D(1,2); D(3,1)=D(1,3); D(3,2)=D(2,3);
end
if B <1e-5
    B=zeros(3,3); % symmetric laminate and B should be zero.
end
```

D.3 Function EGv

```
%
% This function is to be used to calculate the Material constants for ST
% and NT interfaces
% The function will return E (0, 45) G (0, 45) and v12 (0 ,45)
%
function [Ei, Gi , vi, ei] =
EGv(Twist,Initial_Pressure,Strain_Rate,Viscosity)
%% Interface Properties
p=Initial_Pressure; st=Strain_Rate; mu=Viscosity;
% p=2;            % initial lamiante pressure in kPa
% st=1.99;        % strain rate of lamiante forming over radius (1/s)
% mu=2.51;        % resin viscosity kPa-s
% Twist=0;        % Define NT as 0 and ST as 1.

Hs=mu*st/p;     % Hersey Number with respect to shear.
K=5.5e9;

if Twist==0
    % Calculation of Material interface Constants for NT
    % Material Constants
    % Twist,Orientation,b,C,P0,m,mg
    %NT 0   5.604  3.24 95.52  0.54 0.127
    %NT 45  5.927  4.5  95.52  0.54 0.127
    Cs= [5.604, 3.24, 95.52, 0.54, 0.127; % 0 orientation (like angle)
        5.927, 4.5, 95.52, 0.54, 0.127]; % 45 orientation (off angle)
    b=Cs(:,1); c=Cs(:,2);  po=Cs(:,3);
    M=Cs(:,4);  Mg=Cs(:,5);
    ei=(c.*p+po).*Hs.^Mg;
    Gi=b*p/(c*p+po)*(Hs).^(M-Mg)*1000; %pa
    vi=(3.*K-2.*Gi)./(2*(3*K+Gi));
    Ei=9.*K.*Gi./(3.*K+Gi)*1000; %pa
elseif Twist==1
    % Calculation of Material interface Constants for NT
    % Twist,Orientation,b,C,P0,m,mg
    %ST 0   5.249  3.24 60.3 0.44 0.169
    %ST 45  5.330  4.5  60.3 0.44 0.169
    Cs=[5.249, 3.24, 60.3, 0.44, 0.169;     % 0 orientation (like angle)
        5.330, 4.5, 60.3, 0.44, 0.169];     % 45 orientation (off angle)
    b=Cs(:,1); c=Cs(:,2);  po=Cs(:,3);
    M=Cs(:,4);  Mg=Cs(:,5);
    Gi=b*p/(c*p+po)*(Hs).^(M-Mg)*1000; %pa
    ei=(c*p+po).*Hs.^Mg;
    vi=(3.*K-2.*Gi)./(2*(3*K+Gi));
    Ei=9.*K.*Gi./(3.*K+Gi)*1000; %pa
else
    display('error')
end
```

D.4 Function Qbars

```
%
% This is a function for calculating Qbar based upon the layup orientation.
%

function Qb=Qbars(Q11,Q12,Q22,Q66,Angle)
[j k]=size(Angle);
for i=1:k
    t=Angle(i);
    Qb(i,1)=t;
    Qb(i,2)=
Q11*cosd(t).^4+2.*(Q12+2*Q66).*sind(t).^2.*cosd(t).^2.+Q22.*sind(t).^4;
%Column 2 is Qb11
    Qb(i,3)=(Q11+Q22-
4*Q66).*sind(t).^2.*cosd(t).^2.+Q12*(sind(t).^4.+cosd(t).^4);         %Column
3 is Qb12

Qb(i,4)=Q11*sind(t).^4.+2*(Q12+2*Q66).*sind(t).^2.*cosd(t).^2+Q22.*cosd(t).^4
;         %Column 4 is Qb22
    Qb(i,5)=(Q11-Q12-2*Q66)*(sind(t).*cosd(t).^3)+(Q12-
Q22+2*Q66).*sind(t).^3.*cosd(t);    %Column 5 is Qb16
    Qb(i,6)=(Q11-Q12-2*Q66)*(sind(t).^3.*cosd(t))+(Q12-
Q22+2*Q66)*sind(t).*cosd(t).^3;     %Column 6 is Qb26
    Qb(i,7)=(Q11+Q22-2*Q12-
2*Q66)*sind(t).^2.*cosd(t).^2+Q66*(sind(t).^4.+cosd(t).^4);     %Column 7 is
Qb66
end
```

D.5 Function ABD0

```
%
% this function calculates the A, B, and D matrix for a green PW laminate
% with no prepreg influence.
%
function [A B D]= ABD0(Laminate,Twist,Initial_Pressure,Strain_Rate,Viscosity)
p=Initial_Pressure; st=Strain_Rate; mu=Viscosity;
% Laminate=[45,0,45,0,45,45,0,45,0,45] Layup referencing major ply angle
% Twist    NT=0, ST=1
% mu      resin viscosity kPa-s
% p= initial laminate pressure in kPa
%st= strain rate of laminate forming over radius (1/s)

%% Interface Properties
[Ei Gi vi ei] = EGv(Twist,p,st,mu);
ti=-4E-07*p+5E-05;              % thickness of resin interface in meters

%% Carbon Properties
Ec=0;
Gc=0;
vc=0.1;
tc=0.0086*25.4/1000;          % thickness of Carbon Ply in meters

%% Calculation of Q's
```

```
% carbon
Qc11=Ec/(1-vc*vc);
Qc22=Ec/(1-vc*vc);
Qc66=Gc;
Qc12=vc*Ec/(1-vc*vc);
% interface
Qi11=Ei./(1-vi.^2);
Qi22=Ei./(1-vi.^2);
Qi66=Gi;
Qi12=vi.*Ei./(1-vi.^2);

%% Calculation of Qbar's
Angles=[0 45];
Qbc=Qbars(Qc11,Qc12,Qc22,Qc66,Angles);
for i=1:2
    ori=Angles(i);
    Qbi(i,:)=Qbars(Qi11(i),Qi12(i),Qi22(i),Qi66(i),ori);
end

%% Zk's
[n m]=size(Laminate);
ml=2*m-1;
z=zeros(ml,7);
j=1;
for i=1:2:ml        %Ply Angle and Thickness
    z(i,2)=tc;
    z(i,1)=Laminate(j);
    if i>1
        z(i-1,2)=ti;
        if Laminate(j)~=Laminate(j-1)
            z(i-1,1)=45;
        else
            z(i-1,1)=0;
        end
    end
    j=j+1;
end
z(m,3)=z(m,2)/2;    % Midply zk+1 *NOTE: Must have even ply count
z(m,4)=-z(m,2)/2;   % MidPly zk-1 *NOTE: must have even ply count
j=1;                % Counter
for i=m+1:ml        % Zk+1 (3) Zk-1 (4)
    z(i,3)=z(i,2)+z(i-1,3); %zk+1 positive
    z(i,4)=z(i-1,3);        %zk-1 positive
    z(m-j,4)=-z(m-j,2)+z(m-j+1,4); %zk+1 negative
    z(m-j,3)=z(m-j+1,4);            %zk-1 negative
    j=j+1;
end
for i=1:ml          % z,z2,z3
    z(i,5)=z(i,3)-z(i,4);       %Zk-Zk-1
    z(i,6)=(z(i,3)^2-z(i,4)^2)./2;   %Zk^2-Zk-1^2
    z(i,7)=(z(i,3)^3-z(i,4)^3)./3;   %Zk^3-Zk-1^3
end

%% Laminate ABD's
A=zeros(3,3); B=zeros(3,3); D=zeros(3,3);
for i=1:ml
```

```
    if z(i,2)==tc
        if z(i,1)==45
            Qb=Qbc(2,:);
        elseif z(i,1)==0
            Qb=Qbc(1,:);
        else
            display('error')
        end
    elseif z(i,2)==ti
        if z(i,1)==45
            Qb=Qbi(2,:);
        elseif z(i,1)==0
            Qb=Qbi(1,:);
        else
            display('error')
        end
    end
    A(1,1)=Qb(2)*z(i,5)+A(1,1);
    A(1,2)=Qb(3)*z(i,5)+A(1,2);
    A(2,2)=Qb(4)*z(i,5)+A(2,2);
    A(1,3)=Qb(5)*z(i,5)+A(1,3);
    A(2,3)=Qb(6)*z(i,5)+A(2,3);
    A(3,3)=Qb(7)*z(i,5)+A(3,3);
    A(2,1)=A(1,2); A(3,1)=A(1,3); A(3,2)=A(2,3);

    B(1,1)=Qb(2)*z(i,6)+B(1,1);
    B(1,2)=Qb(3)*z(i,6)+B(1,2);
    B(2,2)=Qb(4)*z(i,6)+B(2,2);
    B(1,3)=Qb(5)*z(i,6)+B(1,3);
    B(2,3)=Qb(6)*z(i,6)+B(2,3);
    B(3,3)=Qb(7)*z(i,6)+B(3,3);
    B(2,1)=B(1,2); B(3,1)=B(1,3); B(3,2)=B(2,3);

    D(1,1)=Qb(2)*z(i,7)+D(1,1);
    D(1,2)=Qb(3)*z(i,7)+D(1,2);
    D(2,2)=Qb(4)*z(i,7)+D(2,2);
    D(1,3)=Qb(5)*z(i,7)+D(1,3);
    D(2,3)=Qb(6)*z(i,7)+D(2,3);
    D(3,3)=Qb(7)*z(i,7)+D(3,3);
    D(2,1)=D(1,2); D(3,1)=D(1,3); D(3,2)=D(2,3);
end
if B <1e-5
    B=zeros(3,3); % symmetric laminate and B should be zero.
end
```

D.6 Function ABD0f

```
%
% this function calculates the A, B, and D matrix for a green PW laminate
% with input Prepreg G and Interface G.
%
function [Qi66,A, h]=
ABD0f(Laminate,Twist,Initial_Pressure,Strain_Rate,Viscosity,G13c,G13i)
```

```
p=Initial_Pressure; st=Strain_Rate; mu=Viscosity;
% Laminate=[45,0,45,0,45,45,0,45,0,45] Layup referencing major ply angle
% Twist    NT=0, ST=1
% mu      resin viscosity kPa-s
% p= initial laminate pressure in kPa
%st= strain rate of laminate forming over radius (1/s)

%% Interface Properties
[Ei Gi vi ei] = EGv(Twist,p,st,mu);
ti=-4E-07*p+5E-05;              % thickness of resin interface in meters
Gi=[G13i;G13i];

%% Carbon Properties
Ec=0;
Gc=G13c;
vc=0.1;
tc=0.0086*25.4/1000;          % thickness of Carbon Ply in meters

%% Calculation of Q's
% carbon
Qc11=Ec/(1-vc*vc);
Qc22=Ec/(1-vc*vc);
Qc66=Gc;
Qc12=vc*Ec/(1-vc*vc);
% interface
Qi11=Ei./(1-vi.^2);
Qi22=Ei./(1-vi.^2);
Qi66=Gi;
Qi12=vi.*Ei./(1-vi.^2);

%% Calculation of Qbar's
Angles=[0 45];
Qbc=Qbars(Qc11,Qc12,Qc22,Qc66,Angles);
for i=1:2
    ori=Angles(i);
    Qbi(i,:)=Qbars(Qi11(i),Qi12(i),Qi22(i),Qi66(i),ori);
end

%% Zk's
[n m]=size(Laminate);
ml=2*m-1;
z=zeros(ml,7);
j=1;
for i=1:2:ml        %Ply Angle and Thickness
    z(i,2)=tc;
    z(i,1)=Laminate(j);
    if i>1
        z(i-1,2)=ti;
        if Laminate(j)~=Laminate(j-1)
            z(i-1,1)=45;
        else
            z(i-1,1)=0;
        end
    end
    j=j+1;
end
```

```
z(m,3)=z(m,2)/2;    % Midply zk+1 *NOTE: Must have even ply count
z(m,4)=-z(m,2)/2;   % MidPly zk-1 *NOTE: must have even ply count
j=1;                % Counter
for i=m+1:ml        % Zk+1 (3) Zk-1 (4)
    z(i,3)=z(i,2)+z(i-1,3); %zk+1 positive
    z(i,4)=z(i-1,3);        %zk-1 positive
    z(m-j,4)=-z(m-j,2)+z(m-j+1,4); %zk+1 negative
    z(m-j,3)=z(m-j+1,4);           %zk-1 negative
    j=j+1;
end
for i=1:ml          % z,z2,z3
    z(i,5)=z(i,3)-z(i,4);       %Zk-Zk-1
    z(i,6)=(z(i,3)^2-z(i,4)^2)./2;   %Zk^2-Zk-1^2
    z(i,7)=(z(i,3)^3-z(i,4)^3)./3;   %Zk^3-Zk-1^3
end
h=z(end,3)*2;
%% Laminate ABD's
A=zeros(3,3);
for i=1:ml
    if z(i,2)==tc
        if z(i,1)==45
            Qb=Qbc(2,:);
        elseif z(i,1)==0
            Qb=Qbc(1,:);
        else
            display('error')
        end
    elseif z(i,2)==ti
        if z(i,1)==45
            Qb=Qbi(2,:);
        elseif z(i,1)==0
            Qb=Qbi(1,:);
        else
            display('error')
        end
    end
    A(1,1)=Qb(2)*z(i,5)+A(1,1);
    A(1,2)=Qb(3)*z(i,5)+A(1,2);
    A(2,2)=Qb(4)*z(i,5)+A(2,2);
    A(1,3)=Qb(5)*z(i,5)+A(1,3);
    A(2,3)=Qb(6)*z(i,5)+A(2,3);
    A(3,3)=Qb(7)*z(i,5)+A(3,3);
    A(2,1)=A(1,2); A(3,1)=A(1,3); A(3,2)=A(2,3);
   end
```